# PROXIMITY EFFECT IN JOSEPHSON JUNCTION ARRAYS FABRICATED ON TOPOLOGICAL INSULATORS

BY

YANG BAI

DISSERTATION

Submitted in partial fulfillment of the requirements
for the degree of Doctor of Philosophy in Physics
in the Graduate College of the
University of Illinois at Urbana-Champaign, 2020

Urbana, Illinois

Doctoral Committee:

Professor Alexey Bezryadin, Chair
Professor James N Eckstein, Director of Research
Research Professor Tai-Chang Chiang
Professor Michael Stone

## ABSTRACT

Topological Insulators (TIs) have attracted quite an amount of attention recently because of their nontrivial surface states and the promising possibility of hosting Majorana Zero Modes (MZMs) when proximity-coupled to normal s-wave superconductors (SC) predicted by Fu and Kane in 2008. Although extensive efforts have been dedicated to the realization of Topological Superconductivity (TSC) via the proximity effect and evidence of TSC have been successfully reported, the superconducting proximity effect between TIs and SC is poorly understood. To tackle this problem, we fabricated and tested a series of Josephson Junction Arrays (JJAs) on TIs of different carrier densities with two kinds of geometrical designs and various spacings. JJA is a great platform to studying 2D superconductivity with tunable critical temperature and current by adjusting island sizes and spacings. In this work, two kinds of islands were fabricated, square shape and dot shape islands, their spacings also vary. From the transport study of Josephson junction made of big square-island arrays, it is found that the contact conductance is related to surface geometry and band structure of TIs, bumper surface and presence of bulk carriers can increase contact conductance, hence enhance the proximity effect. In the second kind of arrays, TI films with and without bulk carriers are both used. To eliminate bulk superconductivity contamination to TSC, we carefully tuned the composition ratio of the TI material grown by molecular beam epitaxy and successfully obtained TI films with intrinsic bulk insulting state, and the TSC induced in JJAs on this kind of TI film is 2D superconductivity and confined only in the top surface state. Temperature dependent resistive transition results and current-voltage characteristics are presented. The contact conductance of 2D carriers is found smaller than the 3D carriers. Results suggest that TSC confined in the top surface state is significantly different from TSC assisted by the bulk state. This work may provide important guidance for future study of TSC and search for MZMs in TI based systems.

## ACKNOWLEDGMENTS

I am honored to be part of the physics department at the University of Illinois, not only because of its long-established reputation for condensed matter physics and it is the home of the BCS theory, but also for its warmness and kindness, for its effort of taking care of all aspects of life of graduate students, from personal life to academic progress and career development. I have received help from many groups of people and experienced a meaningful graduate school life here.

First, I would like to express my deepest appreciation to my advisor, Professor James N Eckstein, for all of his support, guidance, and patience. It was a great opportunity to work with him who has deep and broad knowledge of physics especially in superconductivity and electrodynamics. Professor Eckstein is particularly a good mentor of doing experiment as he has abundant knowledge and hands on experience of film growth, vacuum systems, and electronics. Without him it would have been impossible for me to get started with my experiment for my Ph.D. study.

I also would like to sincerely thank a number of professors who have helped me with my experiment: Professor Alexey Bezryadin and Professor Dale Van Harlingen for letting me use their Helium Dilution fridge, and Professor Tai-Chang Chiang for the ARPES data of my films.

During my thesis work, most of sample fabrication was performed in the Frederick Seitz Materials Research Lab (MRL). I would like to acknowledge all the staff at MRL who are doing a great job maintaining facilities and helping me and other researchers make progress.

Graduate school is challenging and sometimes can be depressing, I am lucky enough to have support from my labmates and friends who helped me accomplish my Ph.D. study. Thanks

to Can Zhang who helped me started with my project, and Carolyn Kan who has been a good friend and source for all my questions to lab issues. Also, thanks to Soorya Suresh Babu who is always ready to help. Special thanks to my friends, Lina Li, who has been a close friend to me throughout my graduate school, Guannan Chen and Xiangyu Song who are my graduate school fellows and also good friends, and all my lovely dancing friends from Illini Dancesport where I have spent most joyful time during these years.

Finally, I would like to thank my dear parents for their unconditional love and support.

*To my parents.*

# TABLE OF CONTENTS

# CHAPTER 1: INTRODUCTION

We are interested in the topological superconductivity (TSC) which is a promising research area in condensed matter physics. Proposed by Fu and Kane in 2008, the TS can be achieved by combining a topological insulator with a simple s-wave superconductor (SC), at the interface a TS induced in the surface state capable of supporting Majorana Zero Modes (MZMs) will appear. To date, many groups have tested TSC in either bilayer heterostructures or Josephson junctions, see reference [48-56] There are two problems with those TSC. The first one is that induced TSC resides in both bulk and surface states due to the non-insulating bulk states of TIs such as $Bi_2Se_3$ and $Bi_2Te_3$. The second problem is that the TSC carries the inherent property of the SC. Particularly in an STS study[1] on $Bi_2Se_3/NbSe_2$, the measured gap size of TSC induced in $Bi_2Se_3$ is nearly the same as the base $NbSe_2$, this indicate the electrodynamics of the continuous SC layer dominates the dynamics of the whole bilayer system. We aim to create an artificial topological superconductor of which the TSC only resides in the surface state and the electrodynamics is dominated by the TSC. We make use of the gapless surface state of TIs . Instead of using continuous SC films, we fabricate Josephson junction arrays (JJAs) by coupling TIs with many small superconducting islands (niobium). The first JJA consists of islands of micron size on $Bi_2Se_3$ as will be presented in chapter 3. Then we optimized JJAs by using bulk-insulating TIs and nano-island arrays. This way, we do worry about TSC coming from the bulk states, and by making island size small (ideally should be smaller than the coherence length of niobium) and spacings small, the induced TSC should be dominated by electrodynamics of TIs. Recall that MZMs take place in cores of these vortices, if vortex dynamics are controlled by the coupled superconductor, then they are subject to vortex pinning which prevents manipulation of MZMs such as braiding. In the nano-island array, the structure of a superconducting vortex will not be determined by characteristic lengths of the superconductor but by the coherence length and penetration depth of the induced TSC. The nano-island array project is presented in chapter 4.

## 1.1 Topological Invariant and Topological Insulators

Topology is originally a term used in mathematics to describe properties of an object that do not change under continuous deformation. Its application in physics may start in the nineteenth century[2] back to the development of electromagnetic theory. The TKNN integers (also referred to as the Chern number *C*) found by Thouless[3,4] *et al*. in the Integer Quantum Hall effect (IQHE) is the beginning of the geometric approach to studying electronic states in condensed matter physics. In a work in 2005, Kane and Mele[5] proposed that the $Z_2$ topological invariant order of Quantum Spin Hall phase of two-band model of a 2D system of a single layer of graphene can be generalized to apply to multiple bands materials. The importance of this work is that it proposed a novel topological invariant order, $Z_2$ order, and by calculating the $Z_2$ invariant of a bulk system one can predict whether special edge or surface states can exist. $Z_2$ invariant is different from the TKNN integers as it is not an integer; it describes parity, either even (topological trivial) or odd (topological nontrivial). And $Z_2$ invariant is protected by time reversal symmetry (TRS), as long as the spin-orbital coupling is present (no external magnetic field) so TRS is not broken then the exotic edge states predicted by $Z_2$ invariant are robust to impurities, disorder and defects. Zhang[6] in 2006 predicted that on the edges of CdTe/HgTe/CdTe quantum well system, spins with opposite sign will counter-propagate and the longitudinal conductance is quantized and equal to $2e^2/h$. In 2007, Molenkamp[7] grew a thin layer of HgTe that showed quantized conductance along the edge of the sample which confirmed Zhang's prediction. This quantum spin Hall state is essentially the same as the 2D topological insulating state in the sense that it can be classified by $Z_2$ invariant, see figure 1.1[8].

Following the work of Kane and Mele, in 2007 Moore[9] showed that in 3D materials it is also possible for electronic conduction to be confined on surfaces and only on surfaces. In fact, it is Moore's team that gave the name Topological Insulators (TIs) to these 3D materials. Also in 2007[10] Fu and Kane predicted that $Bi_{1-x}Sb_x$ alloy should be a TI based on its $Z_2$ topological invariant property for certain compositions and they also pointed out that Angle-Resolved Photoemission Spectroscopy (ARPES) can be used to verify the existence of the topological states. Then in 2008, Hsieh[11] *et al.* experimentally confirmed that $Bi_{1-x}Sb_x$ is a 3D TI. This is the first experimental identification of a 3D TI, and since then other 3D TIs[12] such as $Bi_2Se_3$[13], $Bi_2Te_3$[14,15] and $Sb_2Te_3$[9,16,17] have been discovered and measured by transport[18], ARPES studies[19] and

Scanning Tunneling Spectroscopy (STS) studies[20]. From these theoretical and experimental studies, we have learned that TIs are materials characterized by gapless surface or edge states that coexist with gapped bulk states. From the topology view of the band structure, this gapped state is a novel electronic state that is different from conventional insulators and semiconductors because its band structure cannot continuously deform into an insulating gap or semiconducting gap state without gap closing at the boundary. A naïve explanation for why TIs have gapless surface states is that TIs have very strong spin-orbital coupling which results to band inversion of valence band and conduction. For this band-invert bulk state to accommodate the band structure of the vacuum or insulator outside the TI that are topological trivial, the gap must close and reopen passing from one side to the other. The close and reopen process leads the gapless surface state.

What is more interesting in TIs is that the surface state has spin-momentum locking. This novel property of TIs opens a door towards a world of new quantum states of matter. As predicted by Fu and Kane[21], superconductivity induced by proximity effect on topological insulating surface state leads to a state where Majorana Zero Modes (MZMs) can exist. ARPES study[22,23] shows the chemical potential of undoped $Bi_2Se_3$ is within the bulk conduction band and surface state has linear dispersion relation near the Dirac Point. This also makes $Bi_2Se_3$ based Superconductor-TI system a good candidate[24,25] for studying MZMs. Although several studies have been done on heterostructure of TIs/S[26,27] 2D arrays of S-TI-S junctions have not been investigated yet. Superconductivity in 2D junction arrays on normal metals have been studied by researchers such as Resnick, Lobb, Tinkham,[28,29] and Eley[30],etc. Arrays fabricated on semiconductors have been studied recently by Charlotte Georgine Lang Bøttcher[31]. In terms of carrier densities, materials used in previous array studies are either very high, $10^{17}/cm^2$ for Cu, or very low, $10^{12}/cm^2$ for InGaAs/InAs heterostructure. Carrier density of topological insulators $Bi_2Se_3$ and $Bi_xSb_{(2-x)}Te_3$ used in this study is within a range of $2\times10^{12}$~$7\times10^{13}/cm^2$, filling the gap of material carrier density used in previous JJAs studies. Therefore, electronic properties of JJAs on TIs may exhibit novel features. Out of interest of fundamental physics of electronic properties of TIs and of searching for MZMs, study of Josephson junction array on TIs is conducted.

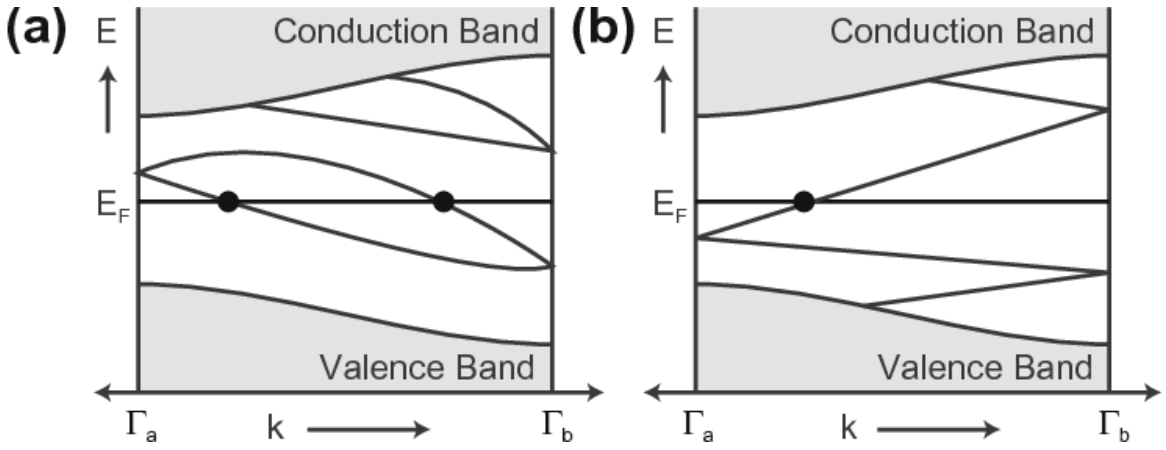


Figure 1.1 Electronic dispersion relation of two kinds of systems. (a) The Fermi energy crosses even number of surface states ($Z_2$ topological trivial). (b)The Fermi energy crosses odd number of surface states ($Z_2$ topological nontrivial), this odd parity leads to the topologically protected boundary state. This picture is from reference [8].

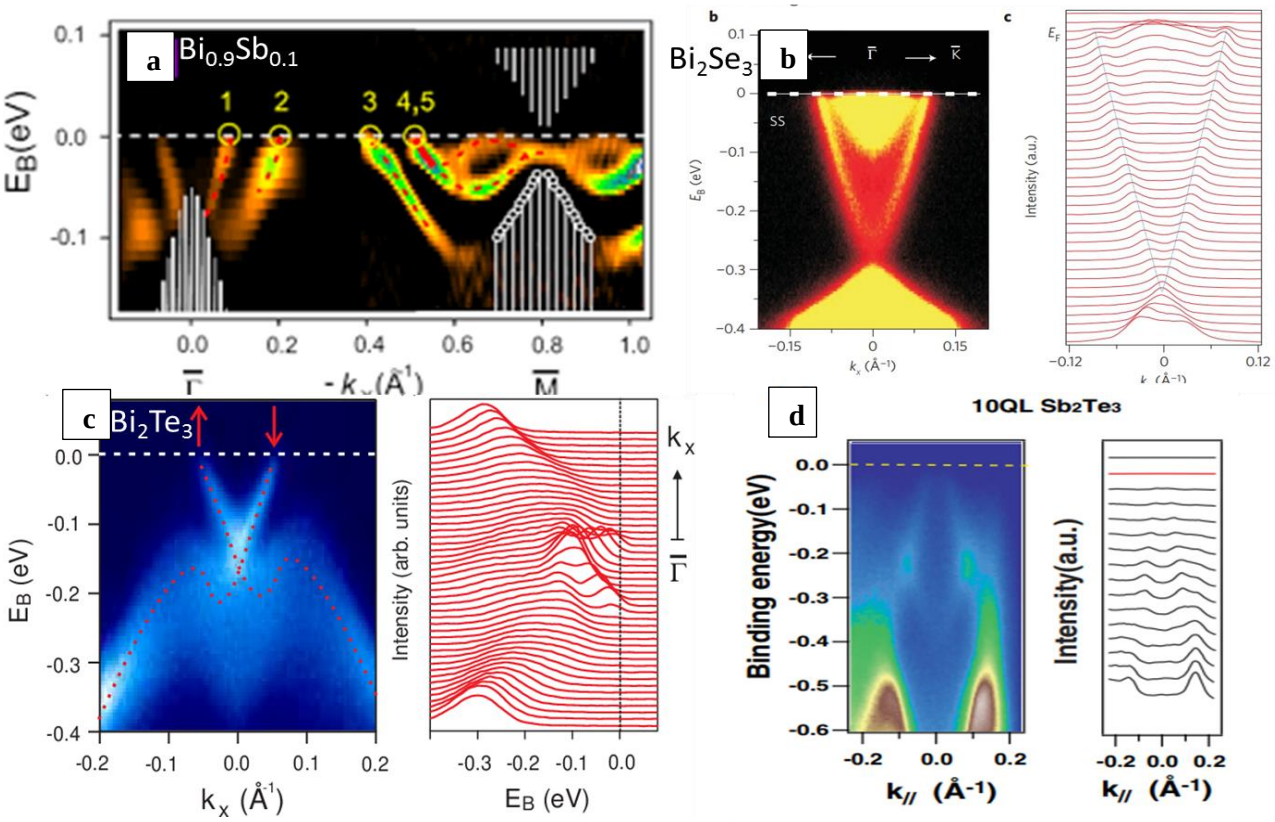


Figure 1.2 ARPES study of $Bi_{0.9}Sb_{0.1}$[11], $Bi_2Se_3$[13], $Bi_2Te_3$[15] and $Sb_2Te_3$[17]. (a) is the second derivative of ARPES of $Bi_{0.9}Sb_{0.1}$, white lines indicate bulk bands, surface states of $Bi_{0.9}Sb_{0.1}$ take a ∞ shape, it crosses the Fermi energy five time so it is $Z_2$ nontrivial; (b) (c) (d) are ARPES of $Bi_2Se_3$, $Bi_2Te_3$ and $Sb_2Te_3$ respectively showing surface states that cross at a single Dirac point.

## 1.2 $Bi_2Se_3$ and $Bi_xSb_{(2-x)}Te_3$

Band structure of $Bi_2Se_3$ (Bismuth Selenide) was first calculated in 2009 by Shou-Cheng Zhang *et al* [32] and was found to have a single Dirac cone at the surface, that is, a gapless surface state. Since then this material has been extensively studied both experimentally and theoretically. $Bi_2Se_3$ crystal structure is rhombohedra, along the C-axis, it has layered structure. The unit cell consists of 15 atomic layers but usually the smallest repeating unit is the 5-layer structure: Se-Bi-Se-Bi-Se. Each atomic layer has triangular lattice structure, and the stacking pattern is shown in figure 1.3. Bi and Se layers are bonded by covalent bonding while between the Se-Se it is the Van der Waals force. This is a very import feature for all TIs such as $Bi_2Se_3$, $Bi_2Te_3$, $Sb_2Te_3$ and the ternary and quaternion TIs which makes these TIs are very tolerant to lattice mismatch to the substrate when using molecular beam epitaxy growth method.

$Bi_xSb_{(2-x)}Te_3$ has the same lattice structure as of $Bi_2Se_3$. Bi and Sb atoms share the equivalent sites and are interchangeable (right panel of figure 1.3). The motivation for growing $Bi_xSb_{(2-x)}Te_3$ is to study topological superconductivity purely in surface state. Although proximity effect induced superconductivity in $Bi_2Se_3$ have been realized and studied as mentioned in the Introduction and also in my only study as will be shown in Chapter 3, it is hard to determine whether the superconductivity really only happens in surface state or it is a mixed proximity effect between surface and bulk states. It is well known that $B_2Te_3$ is always n-type doped and $Sb_2Te_3$ is p-type doped. A lot of study has shown that buy doping $Bi_2Te_3$ using Sb (or doping $Sb_2Te_3$ using Bi), the Fermi level can be tuned so that it only crosses surface states[33]. In the results section, I will present data from array samples on both $Bi_2Se_3$ and $Bi_xSb_{(2-x)}Te_3$, the superconductivity in $Bi_2Se_3$ has higher critical temperature bigger critical current due to the assistance of bulk state while in $Bi_xSb_{(2-x)}Te_3$, where the superconductivity is strictly 2D with only surface carriers participate, critical temperature and current massively decrease.

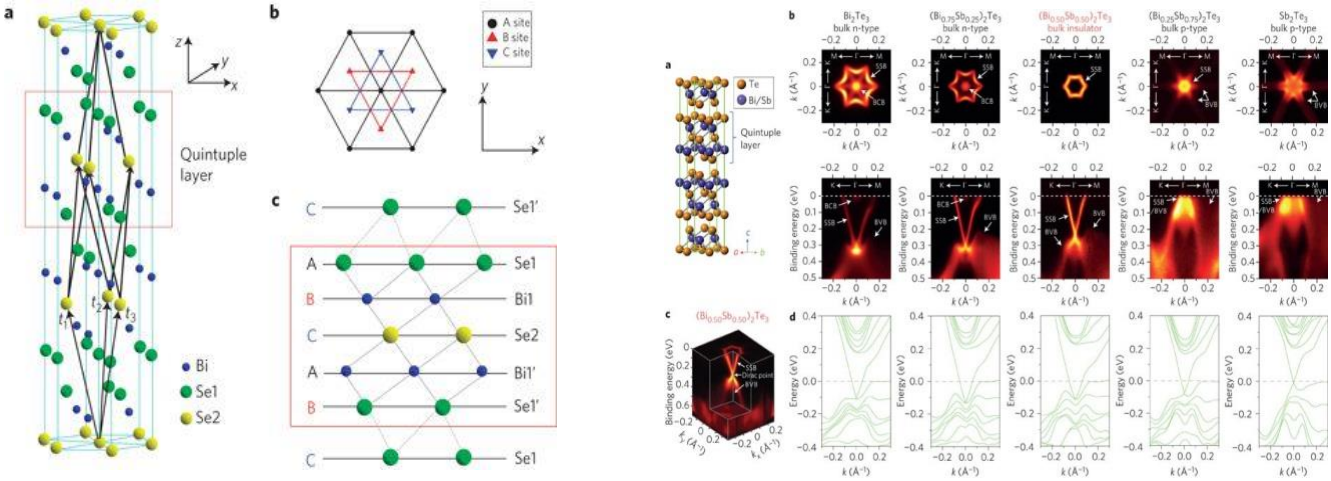


Figure 1.3 The left one is extracted from reference: [Liu, Chao-Xing, et al. "Model Hamiltonian for topological insulators." *Physical Review B* 82.4 (2010): 045122.] which shows lattice structure and stacking order of $Bi_2Se_3$. The right one shows the structure of ternary alloy $Bi_xSb_{(2-x)}Te_3$ and an ARPES [33] study of the evolution of states from bulk n-type to bulk p-type as *x* decreases.

## 1.3 Superconducting Proximity Effect

In the book[34], *Introduction to Superconductivity*, on page 197, Tinkham writes: *the so-called proximity effect (in which Cooper pairs from a superconducting metal in close proximity diffuse into the normal metal)*. That is the only sentence where the superconducting proximity effect is mentioned, and it is in the chapter for Josephson Effect. This sentence is too simple to explain any physics behind the proximity effect, but it does point out one very useful application of it: to introduce superconductivity into other non-superconducting materials such as insulators, semiconductors, and topological insulators. A well accepted theory for proximity effect is the Andreev Reflection mechanism[35]. For example in a bilayer system of a normal metal and a superconductor (NS), from Andreev Reflection perspective, when an electron is incident into the superconductor, it is required that another electron to enter the superconductor at the same time to form a Cooper pair, which can be viewed as the reverse process of a hole enters the normal metal side. The incident electron and the retro-reflected hole together form an Andreev pair. The Andreev pair also carries the phase information of the formed Cooper pair.

In superconducting proximity effect, the coherence length, $\xi_N = \sqrt{\frac{\hbar D_N}{2\pi k_B T}}$ characterizes how far Cooper pairs or non-paired electrons can travel in a non-superconducting material (TIs in this thesis) or in the superconductor before completely loose phase coherence. $D_{S,N}$ is the respective diffusion constant for superconductor and normal metal.

## 1.4 Josephson Effect

Josephson Effect is a phenomenon that happens in a structure of Superconductor-normal metal-superconductor (S-N-S) which is called Josephson junction. A supercurrent can flow cross the junction without any external voltage source applied. The Josephson junction is a link between two superconductors that is weak enough to only allow a slight overlap of electron pair wave-functions of two superconductors. Electron pairs can pass from one superconductor to the other with no applied external voltage. Josephson Effect was first postulated by Brian David Josephson in 1962[36] and was confirmed experimentally by Philip Anderson and John Rowell in 1963[37] . Josephson Effect can be classified into two categories: DC and AC Josephson Effect.

For DC Josephson Effect, equations that describe the behavior of the electron pairs are:

$$J = J_c \sin\phi \quad (1\text{-}1)$$

$\phi$ is the phase difference across the junction, $J$ is the current density, $J_c$ is the critical current density. This equation shows that the DC Josephson current is purely controlled by the phase difference and is linear to the sine product of phase difference.

For AC Josephson Effect, when applied a constant voltage $V$ crossing the Junction, the phase difference is time dependent, and it changes with time following:

$$\frac{\partial\phi}{\partial t} = \frac{2e}{\hbar}V \quad (1\text{-}2)$$

This will induce an AC Josephson current:

$$J = J_c \sin\frac{2eV}{\hbar}t \quad (1\text{-}3)$$

The oscillation frequency is:

$$f = \frac{2eV}{h}$$

One direct prediction by Josephson from the AC Josephson equation is that if driven by a RF source at frequency *f*, I-V characteristics of a Josephson junction will show steps feature at $V = n\frac{hf}{2e}$, *n* is an integer. This prediction was verified firstly by Sidney Shapiro in 1963[38] and is known as Shapiro Steps. Shapiro Steps is one of the hallmarks of Josephson Effect.

There are a few characteristic energy scales of Josephson junctions：

The coupling energy of a Josephson junction and charging energy:

$$E_J = \frac{\hbar I_c}{2e} \qquad (1\text{-}4)$$

$$E_C = \frac{e^2}{2C} \qquad (1\text{-}5)$$

$I_C$ is supercurrent, $C$ is capacitance of a junction. This coupling energy characterizes the strength of coupling between two superconducting wave functions at each side of the normal metal slab. When $E_J >> E_C$, junction energy dominates, the uncertainty of phase difference small described classically. While when charging energy dominates, uncertainty of phase difference is large, quantum phase fluctuation prominent. The coherence length, $\xi_N = \sqrt{\frac{\hbar D_N}{2\pi k_B T}}$, mentioned in the Proximity Effect section sets the scale of the normal metal length. To have two superconducting wave functions coupled, the length of the normal metal needs to be comparable or smaller than the coherence length of the superconductor.

Another characteristic energy scale is the $I_C R_N$ product which is the product of Josephson supercurrent and the resistance of the Junction when it is at normal state. $I_C R_N$ product is proportional to $\Delta(T)/e$[39] where $\Delta$ is the energy gap of the superconductor, *e* is electron charge. This product therefore should only depend on materials used in a junction and should not be affected by the size of it. Josephson junctions made on TIs have shown unconventional size dependence of $I_C R_N$ product. In 2012, a study on a single Josephson junction (Al-$Bi_2Se_3$-Al)[40] reported an unconventional Josephson effect that the $I_C R_N$ product is inversely proportional to the width of a junction which is contrast to the conventional understanding of $I_C R_N$. This phenomenon was explained by the crossing surface states of TIs: as in low temperature supercurrent $I_C$ is controlled by the physics near zero-energy crossing (possible Majorana Zero Modes) and energy scale is set by $hV_{ex}/2eW$ where *h* is the Planck constant, $V_{ex}$ is velocity of carriers, *W* is width of the junction.

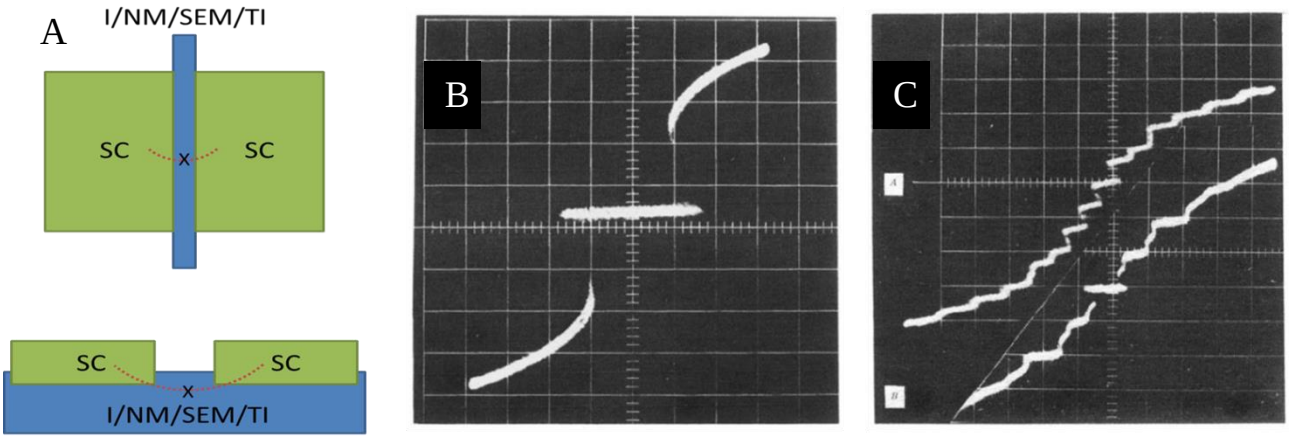


Figure 1.4 A is drawings of two typical designs of Josephson junctions. The upper one is a lateral Josephson Junction with the bridge layer in between, the lower one is a planar Josephson Junction with the bridge layer under superconductors, the layer between superconductors can be insulator, normal metal, semiconductor, or topological insulators. B is I-V characteristic of a Josephson junction. C is the first published picture of Shapiro Steps. B and C are abstracted from Shapiro's paper [38].

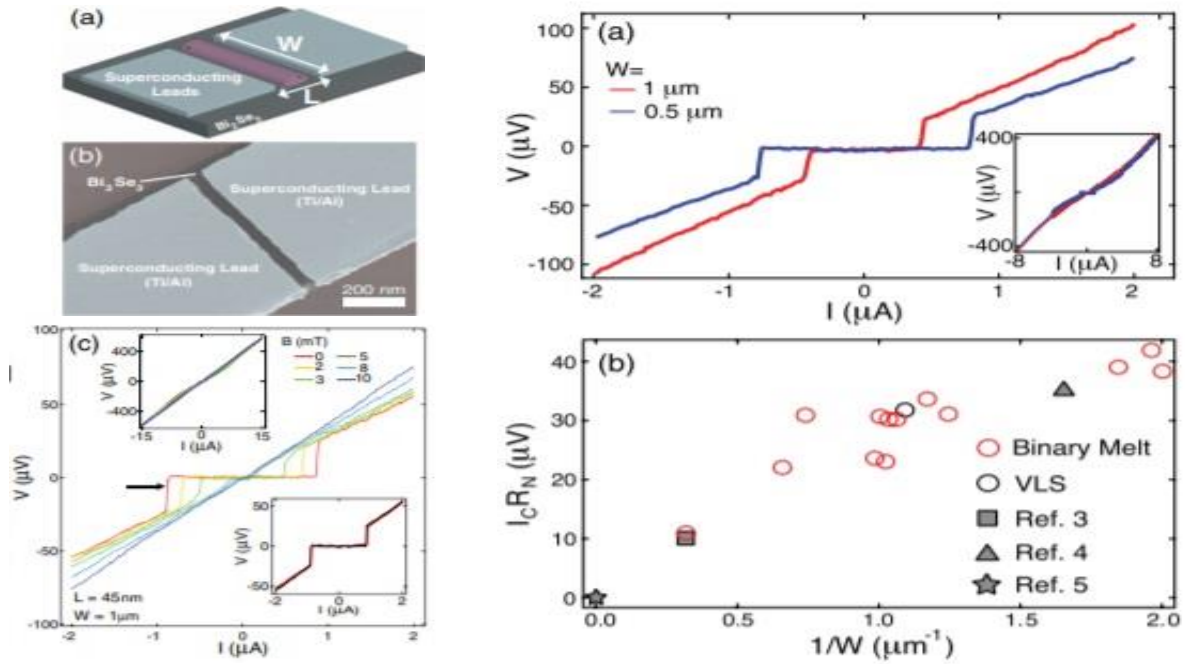


Figure 1.5 On the left side, (a) (b) are device photos and (c) are I-V characteristics of Al-$Bi_2Se_3$-Al junctions. *W* is junction width and *L* is junction length. On the right side, plot (a) shows comparison between two junctions of different width, the normal state resistance of them are about the same while the wider one has smaller $I_C$, in (b) the inverse trend between $I_CR_N$ and *W* is shown [40].

## 1.5 Topological Superconductivity (TSC) and Majorana Zero Modes (MZMs)

The concept of Majorana fermions (MFs) which are their own antiparticles was suggested by Ettore Majorana in 1937[41]. MFs were originally proposed as fundamental particle of nature and not yet have been experimentally observed so far. Recent years, MFs have attracted extensive attention in condensed matter physics as it was found that MFs can be observed as emergent quasiparticle excitations, Majorana Bound State (MBS) or Majorana Zero Modes (MZMs) in spinless p-wave superconducting systems. Majorana excitations obey non-Abelian statistics which are basis for fault-tolerant quantum computation[42]. Majorana excitations must always appear in pairs, each pair can be viewed as a qubit which is the building block of quantum computing circuits. As mentioned in the previous section, Fu and Kane[43] predicted that MZMs can emerge at vortex cores created in a hybrid system of s-wave superconductor-TIs. The theoretical explanation for why this hybrid system can host MZMs is that by combining ordinary s-wave superconductivity and topological surface states, one can effectively create a spinless $p_x+ip_y$ superconducting state. And it has been theoretically predicted that a spinless $p_x+ip_y$ is the simplest platform to host non-abelian Majorana excitations[44,45,46,47].

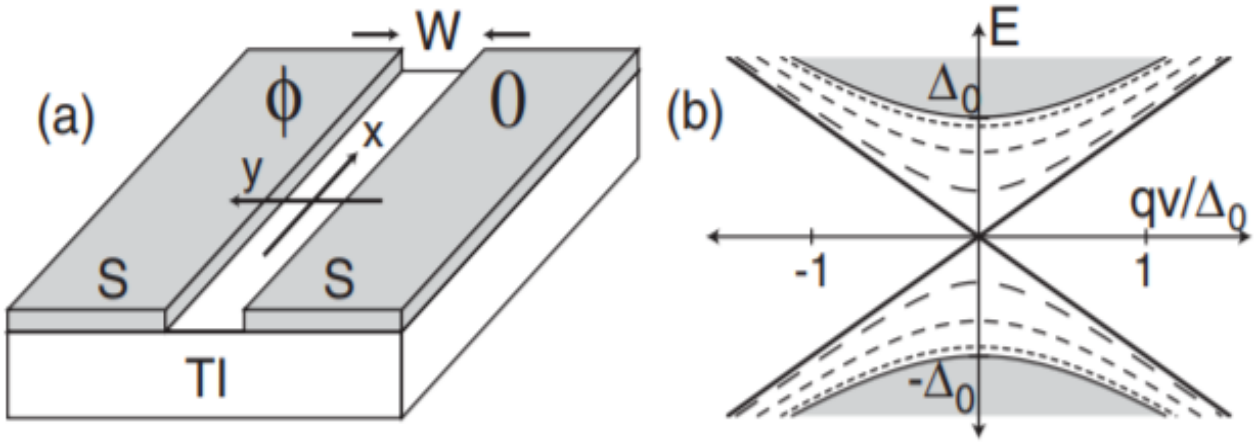


Figure 1.6 (a) The S-TI-S line junction proposed by Fu and Kane. MZMs locate at two ends of the junction (x direction). (b) The energy spectrum as a function of the phase difference, ϕ, crossing the junction (assuming W=μ=0), dashed lines are for ϕ=1/4 π, 2/4 π, 3/4 π; solid line is π.

Fu and Kane's proposal opened an entire new and practical route to searching for Majorana Fermions. There have been extensive studies on Josephson junction fabricated on TIs recent years such as $Bi_2Se_3$-W[48], $Bi_2Se_3$-Al/Ti[49,50,51], Nb- $Bi_2Se_3$-Nb[52], Nb-$Bi_2Te_3$-Nb[53], Pb-$Bi_2Te_3$-Pb[54]. It has

been demonstrated experimentally that a SC-TI-SC Josephson junction with measurable critical current (100nA~10uA) and anomalous $I_CR_N$ behavior (see figure 1.5), and good I-V characteristics of both AC and DC Josephson effect. Beyond the realization of devices proposed by Fu and Kane, there also have been work on signatures of MZMs in these experimental devices. Zero Bias Conductance Peak (ZBCP) has been reported as an indication of MZMs, firstly reported in Scanning Tunneling Microscopy (STM) study because of its ability of imaging real and energy space on heterostructures of TI-SC[55,56]. Although zero bias peak can also be explained by other low energy bound states at the interface of TI-SC, it has been studied by scanning tunneling spectroscopy (STS) combined with angle-resolved photoemission spectroscopy(ARPES) that ZBCP from MZMs is much stronger than other bound states so it is still believed as an evidence of presence of MZMs.



TABLE I. Comparison of the parameters of two of the junctions realized in this work with those available in the literature.

| Reference | Junction | $L$ (nm) | $I_c$ ($\mu$A) | $eI_cR_n/\Delta$ | $\gamma$ | $\mu$ (m$^2$/V s) | $n$ ($10^{12}$ cm$^{-2}$) | Notes |
|---|---|---|---|---|---|---|---|---|
| This work (Ti buffer layer) | Al/$Bi_2Se_3$ | 400 | 0.228 | 0.011 | 0.6 | – | 4.1–4.8 | Fig. 7 |
| This work (Pt buffer layer) | Al/$Bi_2Se_3$ | 300 | 1.67 | 0.086 | 0.9 | – | 4.1–4.8 | Figs. 5, 6, 7(b) (inset) |
| Veldhorst *et al.* [30] | Nb/$Bi_2Te_3$ | 50 | 18 | 0.02 | – | 0.8 | 1.2 | Ballistic proximity effect |
| Sacepe *et al.* [24] | Al/$Bi_2Se_3$ | 400 | 0.3 | 0.073–0.093 | – | 0.5 | 1–5 | Gate tunability of $n$ and $I_c$ |
| Williams *et al.* [25] | Al/$Bi_2Se_3$ | 45 | 0.850 | 0.067–0.267 | – | – | – | Anomalous Fraunhofer patterns |
| Rokhinson *et al.* [11] | Nb/InSb | 30 | 0.45 | 0.13 | >0 | – | – | Anomalous Shapiro steps |
| Oostinga *et al.* [34] | Nb/HgTe | 200 | 3.8 | 0.19 | 0.5 | 2.6 | 0.5 | No bulk losses |

Figure 1.7 A very informative table from reference [51] which summaries size, $I_C$ and $I_CR_N$ information from several work of SC-TI Josephson junctions. All TI flakes from bulk crystals presented in this table have extremely low carrier density ~ $10^{12}cm^{-2}$ compare to thin film $Bi_2Se_3$ grown by molecular beam epitaxy method ~ $3\times10^{13}cm^{-2}$.

Besides in heterostructures of TI-SC, there have also been studies on growing intrinsic topological superconductors which have topological surface states and superconducting gap at sufficiently low temperature such as $Cu_xBi_2Se_3$ [57] and $Sr_xBi_2Se_3$ [58] and iron-based superconductor $FeTe_{0.55}Se_{0.45}$[59].

## 1.6 Josephson Junction Arrays (JJAs)

The origin of interest in Josephson Junction Arrays (JJA) probably can be traced back to the study of arrays of superconducting particles[60] or granular superconducting films. It was soon realized that an artificial JJA is one of the best experimental platforms for studying phase transition[61,62,63,64,65], spin-glass[66], Ising model, flux or vortex dynamics[67,68,69,70], frustration[71,72] and many other interesting topics[73]. And to create variations of Josephson junctions, the weak link connecting superconducting islands can be insulators, normal metals, and semiconductors or topological insulators. By engineering the superconducting material, island size, array geometry, the spacing between islands, weak-link materials, and external magnetic field or RF signal, JJA provides a powerful platform with possibilities to study rich physics such as superconductivity, paraconductivity, Josephson effect and of course phase transition. Many JJAs have been fabricated and reported but no previous study of JJA fabricated on topological insulators has been reported. Current research on TI-SC system mainly focuses on bilayer[54,74,75,76] and single Josephson junction[77] or Josephson interferometry and SQUID[78], this research is the first attempt of this kind and may provide new aspect of studying electronic properties of TIs.

Array properties have been summarized in a nice review paper by P Martinoli and C Leemann[79], here I will just briefly list some basic and important findings on JJAs from previous study. Figure 1.8 is a sketch drawing of a typical JJA with square lattice structure. Each '×' represents a Josephson junction link, $\Phi_i$ is the superconducting phase at island *i*. From Josephson effect, we know that phase difference crossing a junction $\delta_{ij} = \Phi_i - \Phi j_i$ regulates Josephson current in the manner of $I = I_C sin\delta_{ij}$. Josephson coupling energy is given by $E_J = \hbar I_c/2e$ , energy stored in a Josephson junction is $E_J(1 - \cos\delta_{ij})$. The total energy of an array is simply the sum of energy stored in each junction:

$$E = \sum_{i,j} E_J(1 - \delta_{ij})$$

The array can be modeled as a X-Y model of island phases, and of course frustration term should be added if a magnetic field is present.

One of the most often used theories to explain the temperature-dependent resistance transition and current-voltage relation is the BKT phase transition theory. The Berezinskii-

Kosterlitz-Thouless (BKT) [80,81] transition describes the phase transition in a 2D XY model, from bound vortex-antivortex pairs to unbound vortices and antivortices at the BKT transition temperature as temperature increases. BKT transition temperature is defined as the temperature when the I-V curve follows a power law of form:

$$V \sim I^3 \qquad (1\text{-}6)$$

Above $T_{BKT}$ , I-V curve has a leading term which can be expressed as :

$$V = IR_0\, exp\left(-A\sqrt{T_{BKT}/(T - T_{BKT})}\right) \qquad (1\text{-}7)$$

where $R_0$ and $A$ are constants and can be calculated from fitted R-T data. A good example of an experimental confirmation is a study by Resnick and Garland[82], see figure 1.9 for details. One thing of BKT transition is that Lobb, Abraham and Tinkham [83] (LAT), in their theoretical evaluation paper of array data, have found that due to interactions between islands, the Ambegaokar-Haperin temperature-dependent resistance that happens for an isolated Josephson junction is suppressed, leaving the resistance caused by vortex unbinding the dominant source of

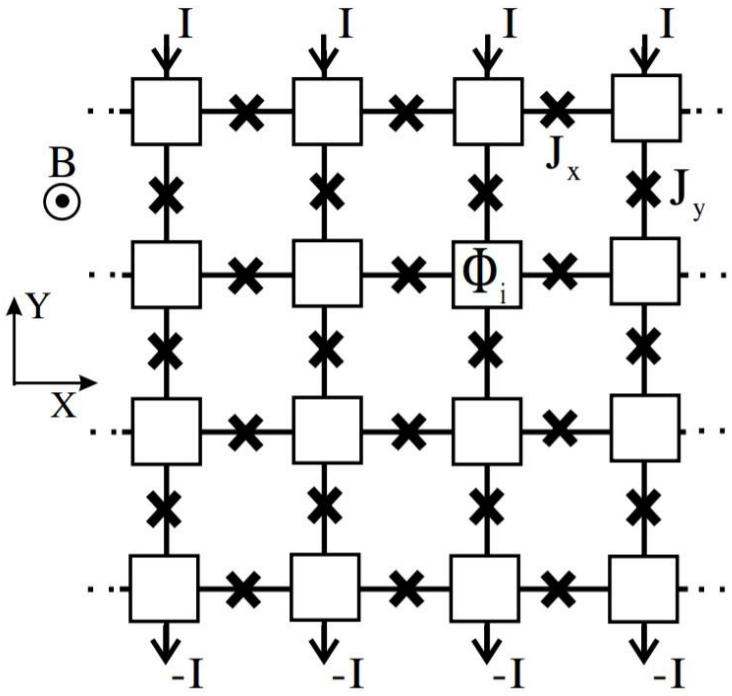


Figure 1.8 Sketch of a JJA borrowed from reference[74]. Each '×' represents a Josephson junction, current flows along Y axis towards negative direction. Because of the direction of current, junctions along column direction will experience most of current flow, due to inhomogeneity there will always be current flowing along row direction.

resistance. This also agrees with the BTK theory. In my thesis research, Josephson junctions between square niobium islands form an array of S-TI-S Josephson junctions and can be treated using XY model (LAT). Comparison of results from these S-TI-S JJAs and BKT theoretical predictions will be made using both R-T and V-I results.

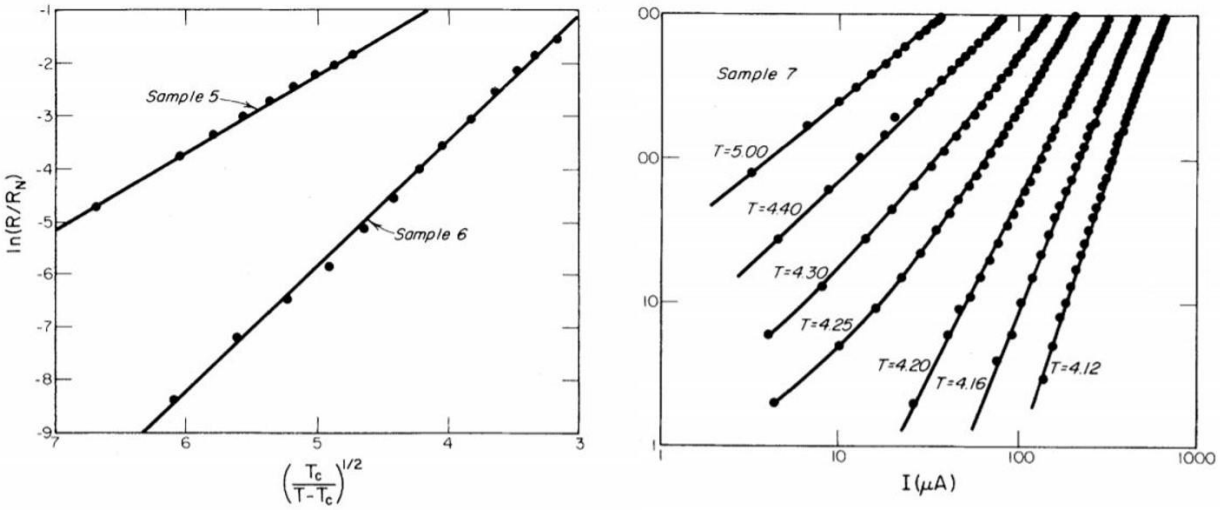


Figure 1.9 BKT transition fitted to experimental data from Resnick and Garland's paper. In the left panel, black dotted lines are experimental data of temperature-dependent resistance of two samples, solid lines are theoretical fitting of formula 1.6-2, a linear fitting between lnR~ $\sqrt{\frac{T_c}{T-T_c}}$ agrees with BKT theory. In the right panel V-I data fitting to power law predicted by BKT theory. As temperature increases, exponent decreases and equals to 3 at the BKT transition temperature.

# CHAPTER 2: EXPERIMENTAL DESIGN AND METHODS

## 2.1 Molecular Beam Epitaxy (MBE) Method

MBE is a physical vapor deposition method for growth of high-quality thin films by putting atoms or molecules on a heated substrate layer by layer. MBE growth takes place inside an ultra-high vacuum (UHV) chamber. UHV lowers the background contamination and provides longer mean free path for atoms or molecular beams evaporated from the source material crucibles. Shutters are used for every crucible to start or stop flux flow source materials. Beam flux can be accurately determined by a quartz crystal microbalance (QCM). The core element of the QCM is a crystal oscillator which has a known resonant frequency $\omega_0$ when fabricated by its manufacturer. Change of the mass of the crystal will introduce a change of the resonant frequency $\delta\omega$. By monitoring the frequency change rate $\delta\omega/\delta t$, the mass change rate can be deduced, combing with the density of the material the beam flux can be obtained. By tuning the source material temperature, desired grow flux and be achieved. By controlling beam flux, opening and closing shutters, and the substrate temperature, MBE offers a broad range of adjustments that can be done to film growth which makes it the most powerful method for high quality thin film growth.

The MBE chamber I used is called Oxide because it was originally used for growth of oxides. Ever since Selenium(Se) and Tellurium(Te) were introduced into the chamber, it is designated to grow topological insulators. Now this chamber has 13 sources and is equipped with a quadruple mass spectrometer (QMS) and a reflection high energy electron diffraction (RHEED) system (figure 2.1). A QMS is equipment that is sensitive to the mass to charge ratio of ions in the surrounding environment. The QMS in the oxide chamber is used as a contamination profiler when there is leakage happening in the chamber. The RHEED is a real time and *in-situ* technique used to monitor and determine the film surface structure during the growth. It consists of an electron gun, a photo-

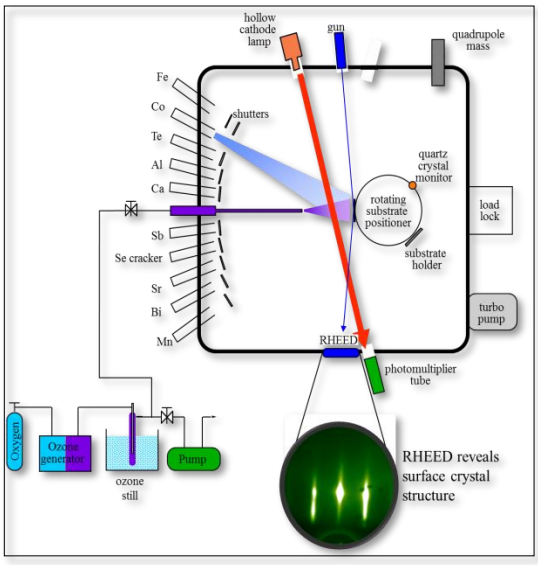


Figure 2.1 Drawing of the Oxide system.

luminescent detector screen and a CCD camera. For a nice MBE grown film, RHEED pattern should show narrow bright streaky lines. Film growth rate can be extracted from RHEED intensity oscillation. Figure 2.2[84] explains how RHEED intensity oscillation relates to the film growth rate. RHEED patterns and intensity oscillations of $Bi_2Se_3$ and $Bi_xSb_{(2-x)}Te_3$ will be shown in section 2.3, the film characterization section.

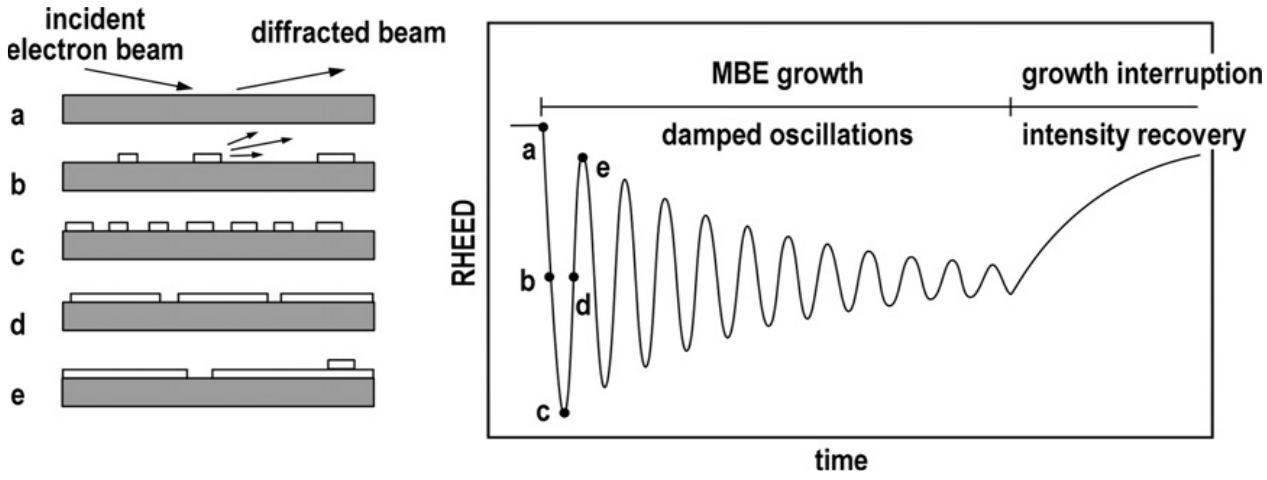


Figure 2.2 How to understand RHEED intensity oscillation. **a.** At the beginning, electron beam hits the flat and clean surface of a substrate and the diffracted beam gives the highest intensity on the recorded area on the fluorescent screen. **b.** Small pieces of films start to grow, they are not connected yet. The incident electron beam is diffracted by these pieces, only part of the diffracted beam can be recorded, so the intensity decreases. **c.** More islands formed, and the surface is highly disordered, the beam is diffracted to all directions, so the intensity drops to lowest value. **d.** As growth keeps going, pieces of film grow larger and merge together to form big areas and the diffracted intensity starts to rise again. **e.** A complete layer has been grown and the intensity reaches its first peak after the growth starts. The time interval between **a** and **e** is the time elapsed for one repeated unit of the film to grow which is the growth rate.

## 2.2 $Bi_2Se_3$ and $Bi_xSb_{(2-x)}Te_3$ Growth

$Bi_2Se_3$ and $Bi_xSb_{(2-x)}Te_3$ films used in my research are all grown in the Oxide chamber in our lab. I will first talk about $Bi_2Se_3$ then briefly go through $Bi_xSb_{(2-x)}Te_3$. The c-plane sapphire

substrates used for growth are bought from a Japanese company, Shinkosha. This company offers sapphire substrates with nice atomic-step finishing surface (figure 2.3). For MBE growth, this atomic level flatness is very important to achieving films with long crystallinity and large terrace. C-plane sapphire substrates provide a 2:1.73 in-plane triangular surface net lattice match with the $Bi_2Se_3$ film. Due to the lattice mismatch, usually there are always triangular dislocations in $Bi_2Se_3$. This kind of dislocation is rooted in the interface of the film and the substrate. To reduce the density of dislocations it is intuitive to put effort on the growth of first few layers. Dr. Kane Scipioni, who was a PhD student in Professor Vidya Madhavan's group, found that annealing the film can increase the flatness and grain size. Inspired by his study, I developed a two-step growth recipe for growing $Bi_2Se_3$, this recipe is afterwards found also applicable to the growth of $Bi_xSb_{(2-x)}Te_3$. A typical growth of one $Bi_2Se_3$ film using the two-step growth is illustrated in figure 2.4. Firstly, 3QL is grown at 220ºC with Se shutter open all the time and Bi shutter opens and closes when each QL starts and ends, then the substrate temperature is increased to 260ºC, and then film will be annealed at this temperature for 30mins, during the annealing Se flux should be provided all the time. After 30mins annealing the growth temperature will be tuned back to 220ºC slowly. When the temperature is stabilized at 220ºC, Bi shutter opens to start the growth of rest of the film. After the desired film thickness has been grown, again the substrate temperature is increased to 260ºC and film is annealed for 4hours with Se flux supplied. Using this two-step growth, super flat film can be obtained, see figure 2.5 for the comparison.

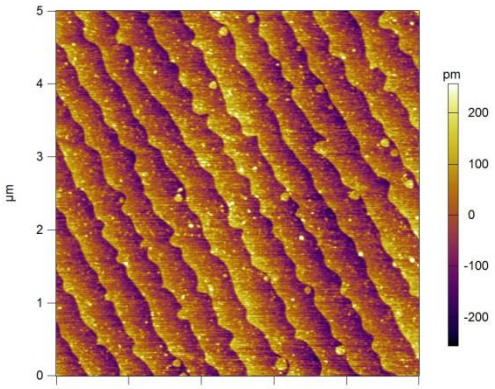


Figure 2.3 AFM of a c-plane sapphire substrate from Shinkosha, shows uniform atomic-step, each step is about 200pm.

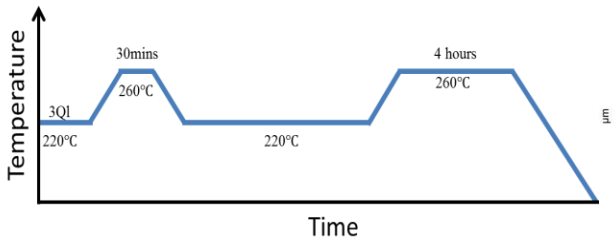


Figure 2.4 Two-step growth for $Bi_2Se_3$ timeline. Film growth rate is controlled by Bi flux, Se/Bi flux ratio is > 8. Se shutter is always open during the entire growth.

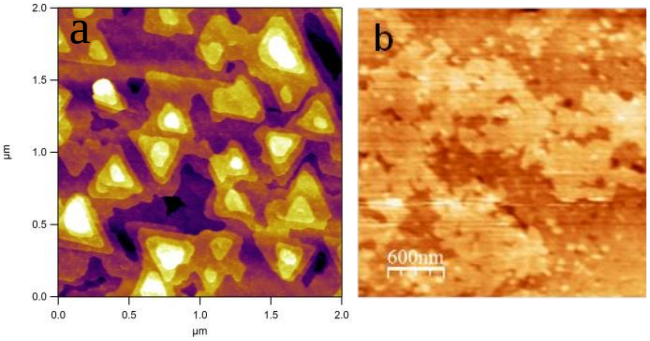


Figure 2.5 AFM of $Bi_2Se_3$ films. a. Grown without post annealing shows triangular dislocations; b. Grown on a Shinkosha substrate with post annealing.

For the growth of $Bi_xSb_{(2-x)}Te_3$, two-step growth method is also applicable. The complete and detailed growth procedure is as following: C-plane sapphire substrates from a company called Shinkosha are used to grow $Bi_xSb_{(2-x)}Te_3$ films. Before introducing the substrate into the growth chamber, the substrate is sonicated for 15mins in acetone followed by 15mins in IPA. After that, the substrate is checked under an optical microscope to make sure no visible contaminations are still present. If the substrate cannot be cleaned by sonication, one can use a TCE rinsed Q-tip to scrub the substrate, and then use IPA to clean up TCE residue. Once the substrate is clean, load it into the chamber immediately. Before starting to grow a film, the substrate needs to be heated up to 600 ºC (or even 700 ºC if necessary, to obtain a nice Rheed reflection pattern) to outgas for at least 2 hours. Any organic residues left on the substrate will leave the substrate after the outgassing. Now the vacuum-level clean substrate is ready for MBE growth. Tune the Bi, Sb and Te fluxes to the desired values by adjusting cell temperatures, make at least two times flux measurements using the QCM to confirm fluxes are stable. Bi/Sb ratio is determined by their flux ratio. For example, if a $BiSbTe_3$ is to be grown then the Bi/Sb is 1. EDS study was not carried to accurately determine the exact ratio Bi/Sb for each film, but flux ratio of Bi/Sb is proportional to the actual Bi/Sb of films. Te/(Bi+Sb) should be bigger than 6 to make sure enough Te is provided. The growth temperature is typically around 200 ºC. Here one thing needs to pay attention to is this 200 ºC is measured by a pyrometer, not the thermocouple, the thermocouple reading is usually around 240 ºC when the pyrometer reads 200 ºC. The substrates used in all films in my thesis work are all back-side coated with 200nm E-beam evaporated Titanium film to make the pyrometer able to read substrate temperature because sapphire

itself is transparent. The emissivity used for Ti is 0.6. Once the substrate temperature is stable, first open the Te shutter 10 seconds before opening Bi and Sb shutters. As introduced before the lattice structure of $Bi_xSb_{(2-x)}Te_3$ is stacked layers of Te-(Sb/Bi)-Te-(Sb/Bi)-Te, and each five layers together is called a quintuple layer (QL). Because Te monolayer is always the starting layer on sapphire substrate so it is very important to create a Te rich environment at the surface before supplying Bi and Sb. During the growth, Sb and Bi shutters open and close together. 3QL is grown after first-step growth, and then the substrate temperature is increased to 280 ºC (pyrometer) slowly (5ºC/min) to anneal for 30mins. After 30mins (should confirm by Rheed for streaky lines, longer annealing time may be needed), substrate temperature is slowly ramped back to 200 ºC, wait for 5mins for the temperature to stabilize and then start to grow the rest of the film. After the deposition is finished, increase temperature again to 280 ºC (pyrometer) slowly (5ºC/min) and anneal film for 4 hours. During the entire growth and annealing, Te shutter should always open to ensure enough Te flux so that the film does not re-evaporate or decompose. Temperatures and flux numbers can vary slightly for each growth, the best way to secure a nice film is to constantly check the Rheed pattern to see whether a nice streaky pattern is present. Copying the recipe that I present here is a safe starting point, but modifications based on experience is encouraged and usually found necessary.

## 2.3 $Bi_2Se_3$ and $Bi_xSb_{(2-x)}Te_3$ Characterization

This section describes surface morphology, and carrier type and concentration information of MBE grown $Bi_2Se_3$ and $Bi_xSb_{(2-x)}Te_3$. Surface morphology is characterized by Rheed and AFM, carrier type and concentration are determined by Hall measurement.

### 2.3.1 Rheed and AFM

Rheed images and oscillations of a 30QL $Bi_2Se_3$ and 5QL $Bi_xSb_{(2-x)}Te_3$ films are shown in first column of figure 2.6. Rheed images show streaky lines that confirm the epitaxy growth of films. Rheed oscillations help determine the growth rate is about 5.8 Å/min and 2.35 Å/min for $Bi_2Se_3$ and $Bi_xSb_{(2-x)}Te_3$, respectively.

To determine the film surface roughness, we refer to AFM images. As displaced on the top side of figure 2.6. $B_2Se_3$ films grown by the two-step method have fewer dislocations within a unit area and show larger terraces. From the AFM of $Bi_2Se_3$, we can tell the longest continues flat film piece is around 2um (film 3638), number of pyramid-shape dislocations per unit area ($um^2$) ranges

from zero (film 3359) to about 4 (film 3638), height of dislocations is less than 6Ql steps (film 3654). $Bi_xSb_{(2-x)}Te_3$ films have more dislocations and smaller terraces. The shape of dislocations is not strictly triangular, the density of dislocations ranges from 4 (film 3615) to 10 (film 3616), height of dislocation is about 5ql steps. By counting number of dislocations and step height of each dislocation, number of steps per unit area can be obtained and it gives the total area of steps per unit area. The importance of area of steps is that it affects the effective contacting area between the film and niobium islands. The effect contacting area combined with the contact conductance will determine the quality of contact which plays the essential role in the superconducting proximity effect. In results chapters, the contacting area and contact conductance will be further discussed.

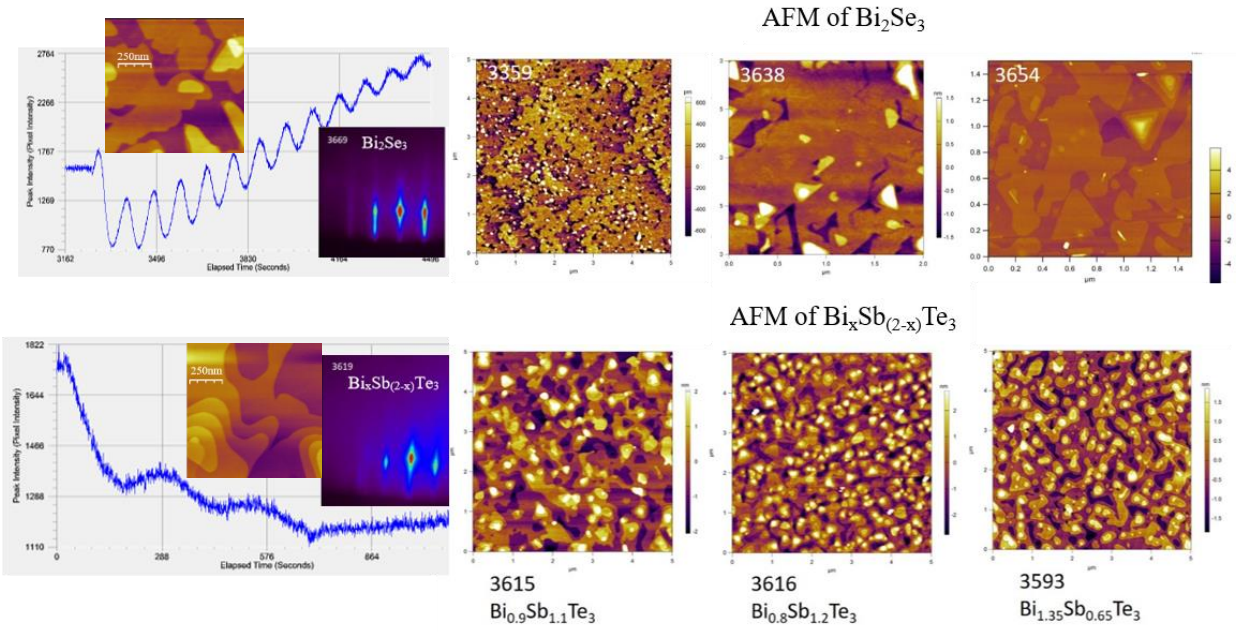


Figure 2.6 Rheed and AFM characterization of $Bi_2Se_3$ and $Bi_xSb_{(2-x)}Te_3$. On the left side two typical AFM images of $Bi_2Se_3$ and $Bi_xSb_{(2-x)}Te_3$ are displayed on top of Rheed oscillation curves. Terraces consisting of QL steps of 1nm high and a few hundred nanometers long are also shown, each step correspond to one oscillation, within a step is a flat film piece.

### 2.3.2 Hall effect

Hall measurement is performed to get carrier density and mobility of $Bi_2Se_3$ and $Bi_xSb_{(2-x)}Te_3$ films. A Hall bar is patterned using E-beam lithography and lifted off, the bar size is 5 by 1, the longitudinal resistance of Hall bar is 5 times the square resistance of the film. Figure 2.7 shows

the drawing of Hall bar and contact pads, dark blue area is etched down to the insulating sapphire substrate by ion milling. Flow a constant DC current, typically 1uA, through the Hall bar and measure longitudinal voltage drop, then apply a magnetic field perpendicular to the bar plane and measure the field dependent transverse voltage, carrier density and mobility can be obtained using the following formulas:

$$R_{\square} = \frac{V_+ - V_-}{5I}$$

$$n_{2D} = \frac{IB}{e(V_{+1} - V_{+2})} = \frac{B}{eR_{xy}}$$

$$\mu = \frac{1}{en_{2D}R_{\square}}$$

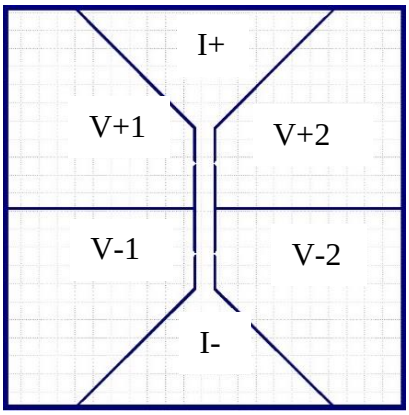


Figure 2.7 Hall bar drawing.

$R_{\square}$ is square resistance, $n_{2D}$ is 2D carrier density, $e$ is one electron charge, μ is carrier mobility.

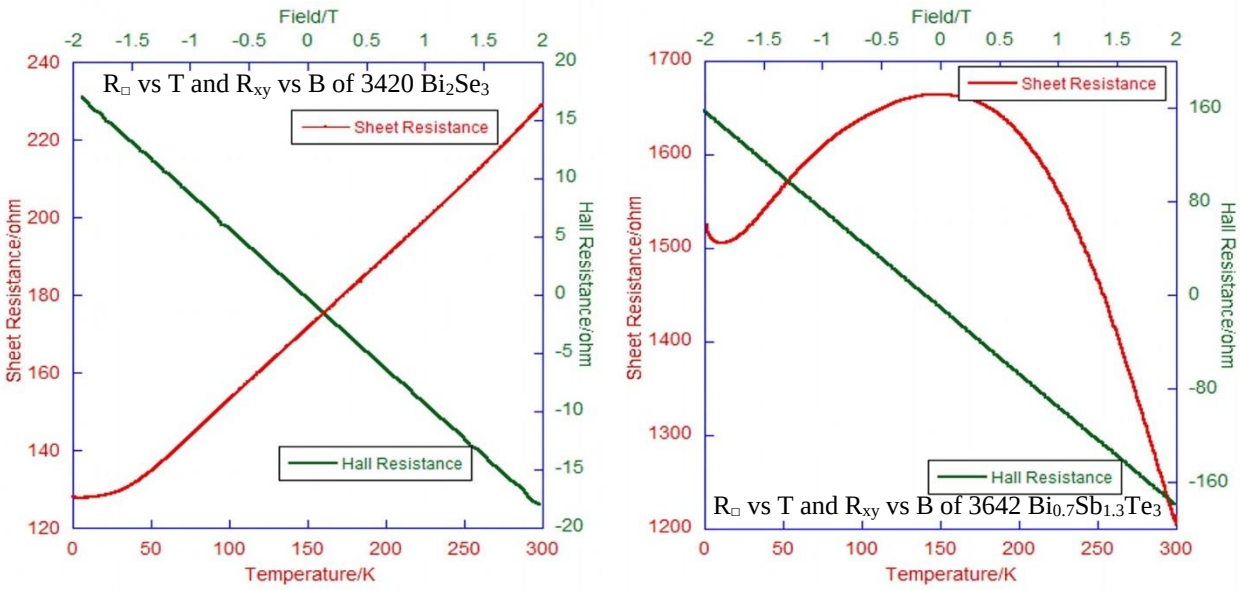


Figure 2.8 Hall results of $Bi_2Se_3$ and $Bi_xSb_{(2-x)}Te_3$. Two kinds of films show different temperature dependent resistance, $Bi_2Se_3$'s $R_{\square}$ keeps decreasing with temperature and flat out at low temperature while $Bi_xSb_{(2-x)}Te_3$'s $R_{\square}$ rises first then decreases and has a tail of increasing again at very low temperature region.

Hall results of two films are shown in figure 2.8 Two-dimensional resistivity of $Bi_2Se_3$ grown in our lab is usually around hundred ohms while for $Bi_xSb_{(2-x)}Te_3$ it is a few thousand ohms and varies with the ratio of Bi/Sb. In Figure 2.9, there are three Hall resistance curves of $Bi_xSb_{(2-x)}Te_3$ films with different Bi/Sb ratios. As Bi/Sb ratio increases, carrier type can change from p-type to n-type as expected, from $Sb_2Te_3$ type to $Bi_2Te_3$ type.

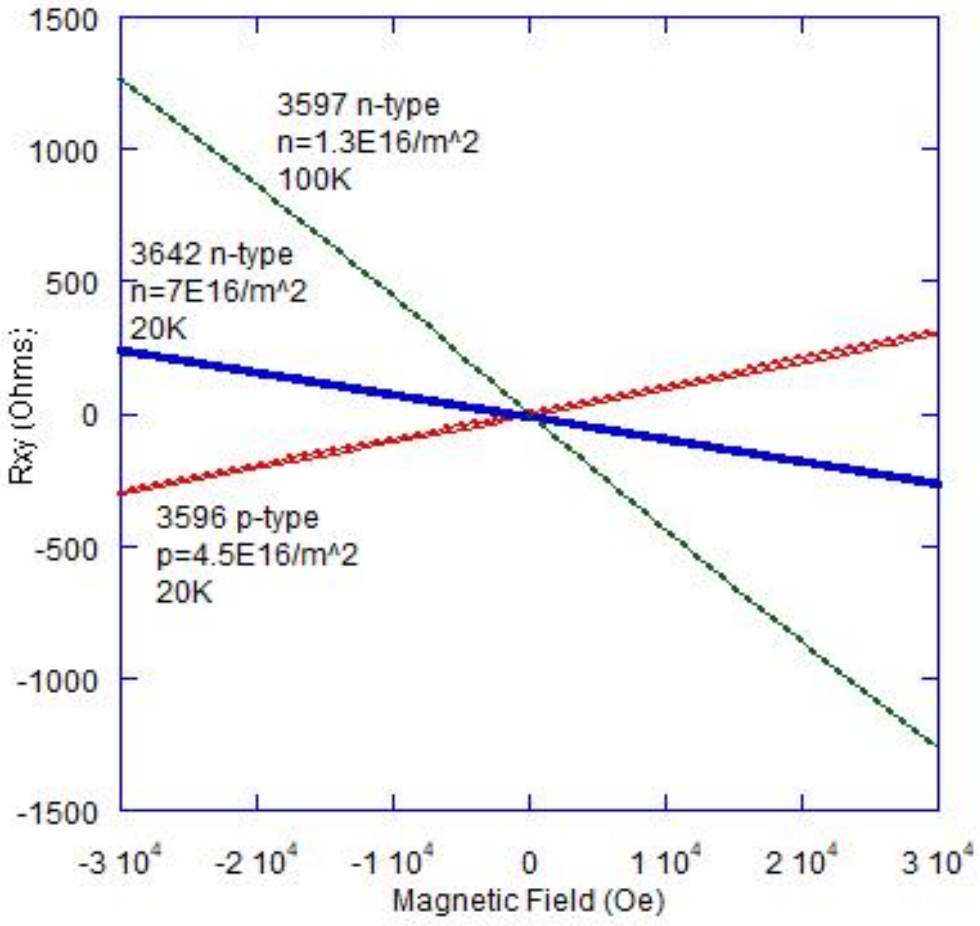


Figure 2.9 Hall results of three $Bi_xSb_{(2-x)}Te_3$ films 3596, 3597 and 3642. Carrier type can be tuned from n-type to p-type.

## 2.4 Film Growth Notes

During the development of the growth recipe for $Bi_xSb_{(2-x)}Te_3$, it was found that films of very thin thickness grown on c-plane sapphire substrates always have holes. As the film thickness increases, size and density of holes decrease (Figure 2.10).

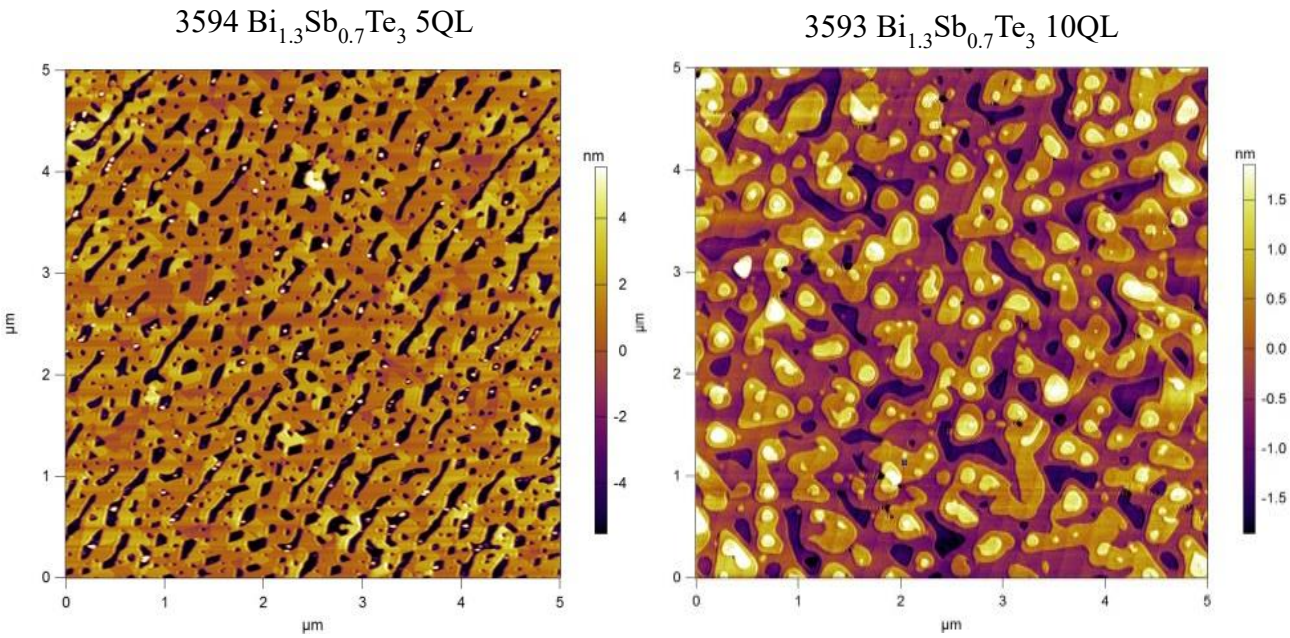


Figure 2.10 When *x* is fixed, density of holes decreases with increasing film thickness for $Bi_xSb_{(2-x)}Te_3$

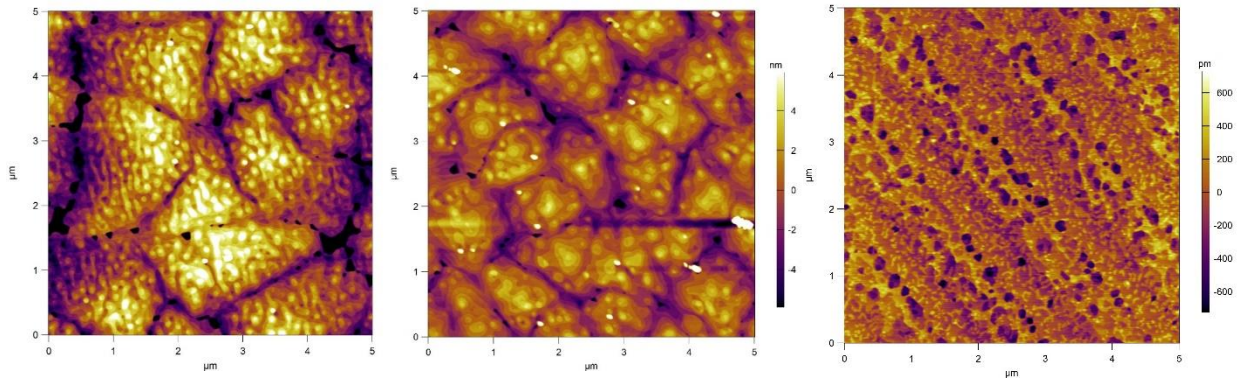

3617 $Bi_{0.69}Sb_{1.31}Te_3$ 10QL on Graphene/SiC

3618 $Bi_{0.7}Sb_{1.3}Te_3$ 10QL on Graphene/SiC

Graphene/SiC substrate used for film 3618.

Figure 2.11 $Bi_xSb_{(2-x)}Te_3$ films grown on Graphene/SiC bilayers and an AFM image of the base substrate before used to grow film 3618.

As a comparison, films grown on Graphene/SiC show a lot of dislocations, bulky grains surrounded by holes (figure 2.11). The shape of grains do not directly relate to the substrate since the substrate used for film 3618 (the film show spiral dislocations) is very flat and have line-shape features just like c-plane sapphires.

## 2.5 Device Fabrication

On film 3248, 3420, 3446 and 3525, arrays of big square niobium islands are fabricated, on film 3642 and film 3678 arrays of nanodot-islands are fabricated. The processing procedure is basically the same, but for nanodot-island arrays, E-beam writing process is slightly different and will be described separately at the end of this section.

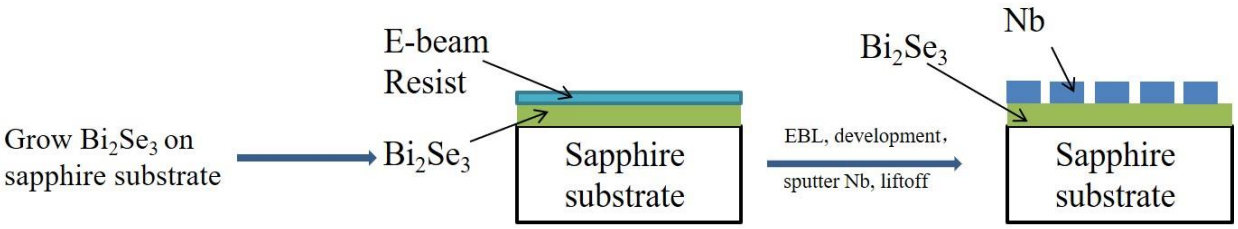


Figure 2.12 Flow chart of fabrication process of island arrays. In the case of nanodot-island arrays on 3642, film is $Bi_xSb_{(2-x)}Te_3$.

Following growth, films were processed into bar-shaped transport samples of either 5 (arrays on 3248, fabricated and tested by Dr. Brian Mulcahy) or 1 (other films) square between longitudinal contacts using standard microelectronic processing. Between contact pairs arrays of big square-islands/nano-dot islands of niobium were lifted off. The pattern was writted by E-beam lithography and the surface of the film was lightly ion milled to remove the layer contaminated by air and previous processing step before niobium was sputtered on the sample. This leaves the region between the islands free of any processing induced contamination. This fabrication process has been depicted in figure 2.12. On each film different gap sizes between the islands were chosen to explore the distance dependence of the transition. Figure 2.13 and figure 2.14 show mask designs for big square-island arrays and nanodot-island arrays.

PMMA is used as E-beam resist for big square-island arrays. Two layers of PMMA were coated to reduce dog ears caused by lift-off. Spin coating speed is 3000/rpm, first layer baked at 105˚C for 2mins, second layer baked at 180˚C for 5mins followed by a thin layer of AquaSave which is a conductive polymer that prevents electrons from accumulating on surface because the sapphire substrate is insulating. After E-beam writing, firstly remove AquaSave using DI water, then develop in solution of 1 part of MIBK and 3 parts of IPA for 1 minute, then load into the sputtering chamber, ion mill and deposit 60-70nm of niobium. Finally put wafer into Acetone overnight to lift off PMMA.

For nanodot-island arrays, ZEP-520A7 E-beam resist is used because it is more resistive to developer than PMMA is so overdevelopment can be prevented. Because of dot size is very small, overdevelopment can affect dot size dramatically. Also, for nanodot-island arrays, instead of writing an area of a dot-shape circle, an actual dot is exposed. See figure 2.14 for E-beam mask of nanodot-island arrays. On the mask, the array is not made of many circular areas but many pixel dots. During the E-beam exposure, electron beam will stop at the location of each dot and dwell for a certain amount of time. Depends on electron beam focal point size and dosage, a dot pattern of a certain diameter will be exposed. Therefore, the dot size is purely controlled by electron beam size and intensity, and pitch size of the array depends on spacing between pixel dots. To achieve desired dot size, a careful dosage test is required to determine the right gun voltage and aperture size. And because the E-beam status may change, this dosage test may be repeated each time before E-beam lithography of an array device is performed.

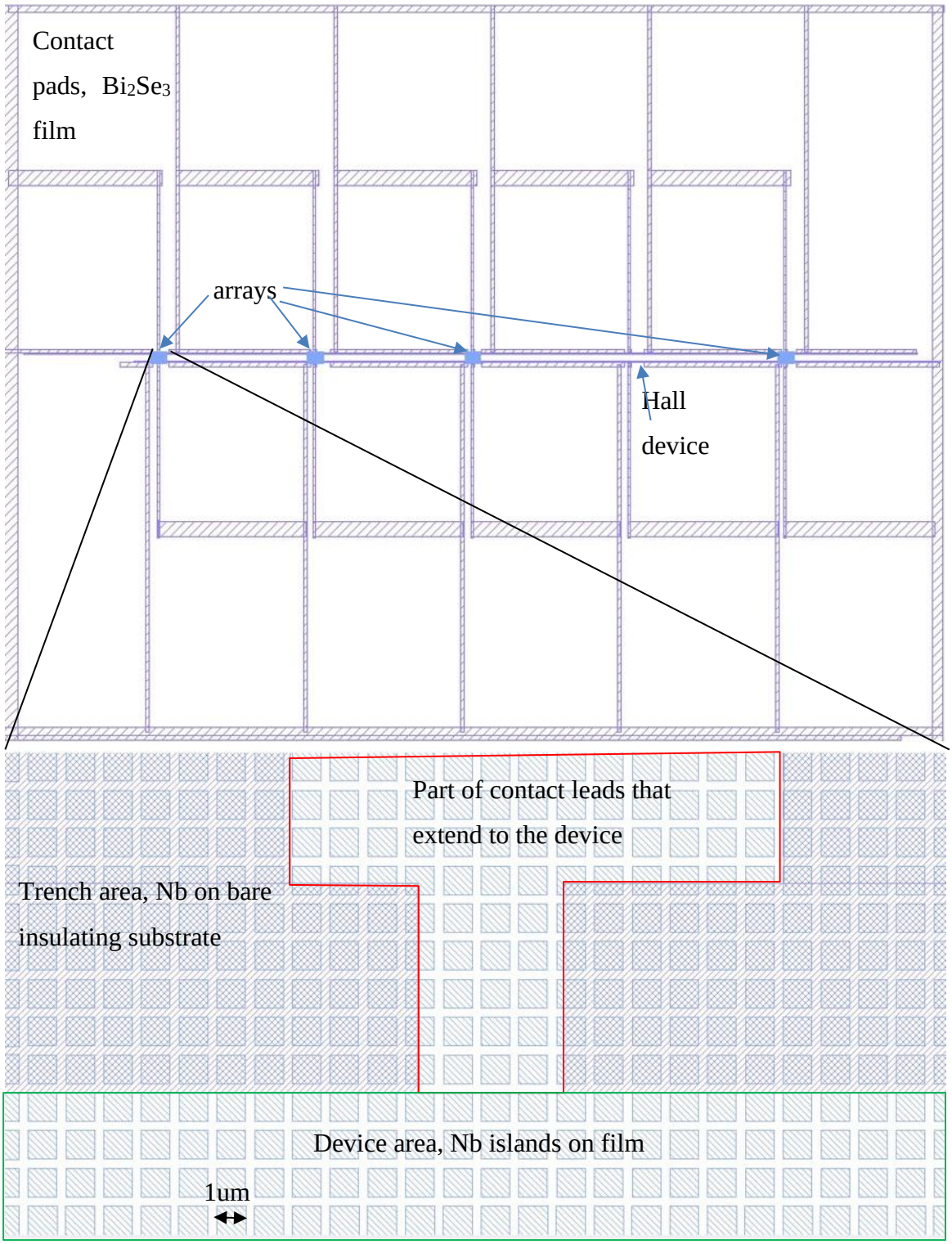


Figure 2.13 E-beam Mask design for square-island array, lower one is the zoom-in view of an array to show each island. Each array is a 1 by 1 square consisting of islands that are designed to be a 1um by 1um squares, spacing varies. Totally four arrays on each film. The blank one is for Hall measurement.

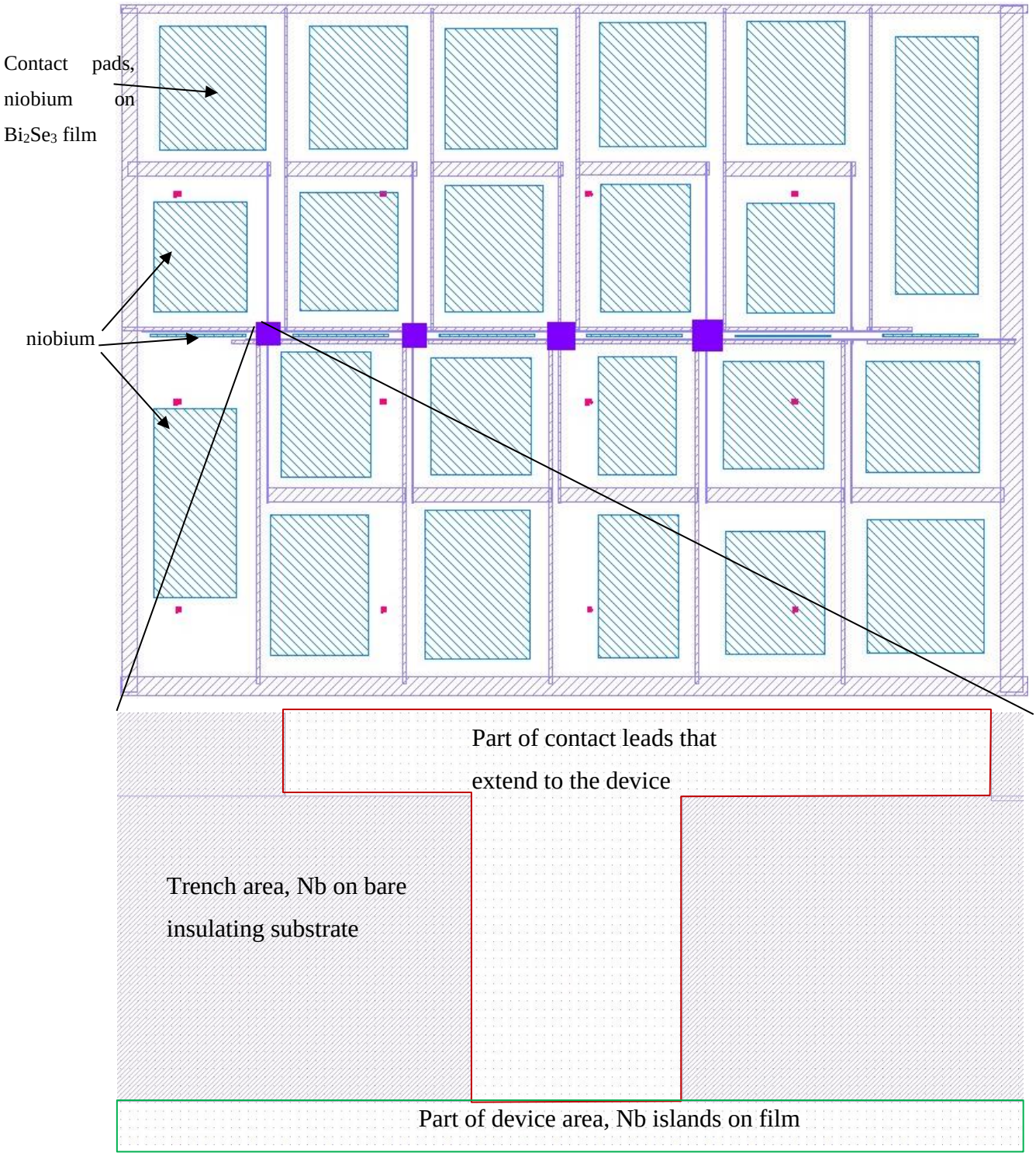


Figure 2.14 E-beam Mask design for nanodot-island array, lower one is the zoom-in view of an array to show each pixel dot. Each array is a 1 by 1 square consisting many dots. Spacing between dots are 200nm, 230nm,260nm and 290nm. Totally four arrays on each film. The blank one is for Hall measurement. Additional niobium is deposited on contact pads and between arrays to get better contact and reduce heat dissipation.

## 2.6 Device Characterization

Devices are characterized by AFM and SEM to check the actual pitch sizes and spacing sizes between islands and to determine whether neighbored islands are shorted.

Figure 2.15 shows AFM and SEM images of big square-island arrays on film 3420, the 1.28um one has been sized down to compare its size with the other 2 AFMs, AFM and SEM of nanodot-island arrays are shown in figure 2.16 :

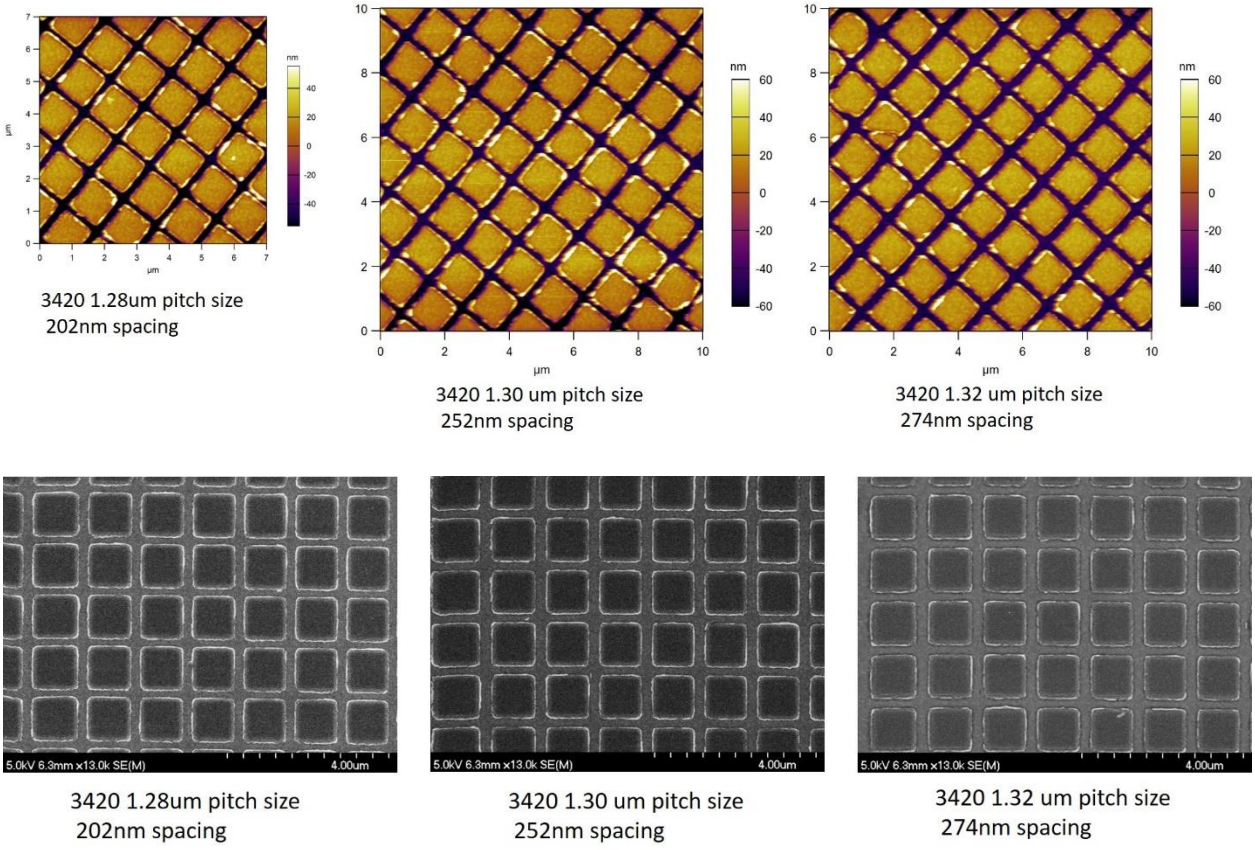


Figure 2.15 The upper panel displays AFM images of three arrays of different spacings and pitch sizes. The lower panel displays SEM images of the same arrays.

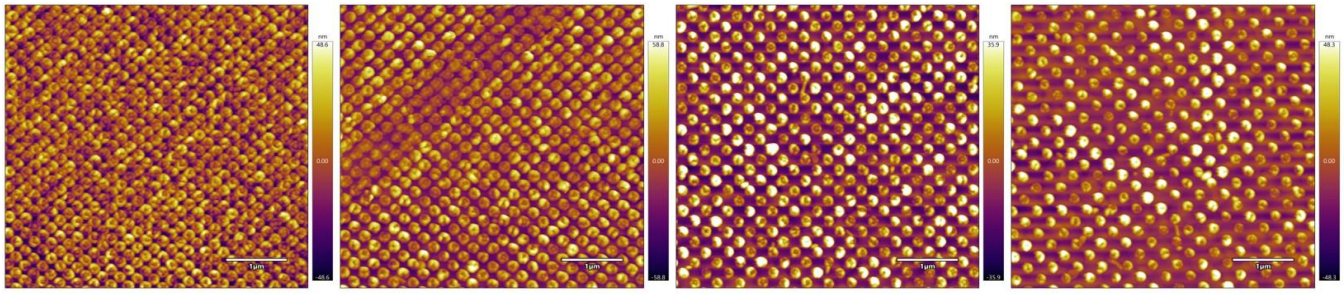

3642 dot-island arrays. From left to right, pitch size is: 200nm, 230nm, 260nm, 290nm

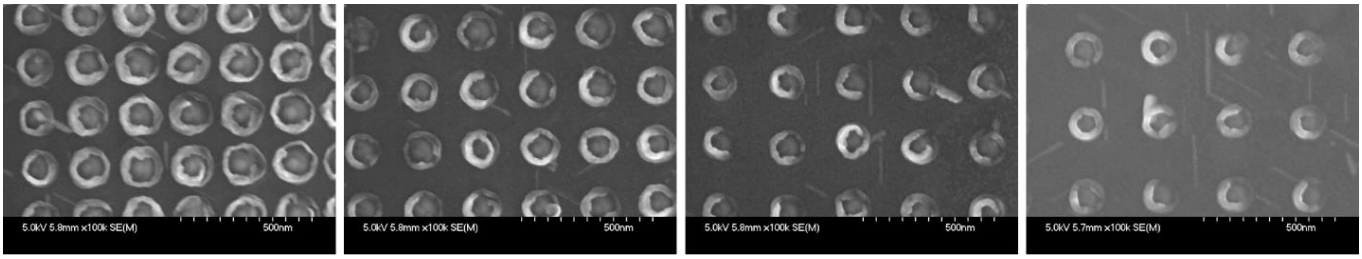


Figure 2.16 The upper panel displays AFM images of four nanodot-island arrays of different pitch sizes made on film 3642. The lower panel displays SEM images of the four nanodot-island arrays made on a different wafer using the exact same fabrication process.

## 2.7 Measurement Set-up

A physical property measurement system (PPMS) by Quantum Design equipped with a magnet of $\pm$ 9T field range is used for Hall measurement, resistance-temperature, and magnetoresistance measurements. A dilution fridge by Oxford is also used to take temperature-resistance, current-voltage, magnetoresistance, and differential resistance measurements at ultra-low temperature (50mK). Figure 2.17 shows a PPMS measurement set-up. For V-I and dV/dI-I measurement, figure 2.18 shows dilution fridge measurement set-up and circuit diagrams for AC R-T and V-I measurements.

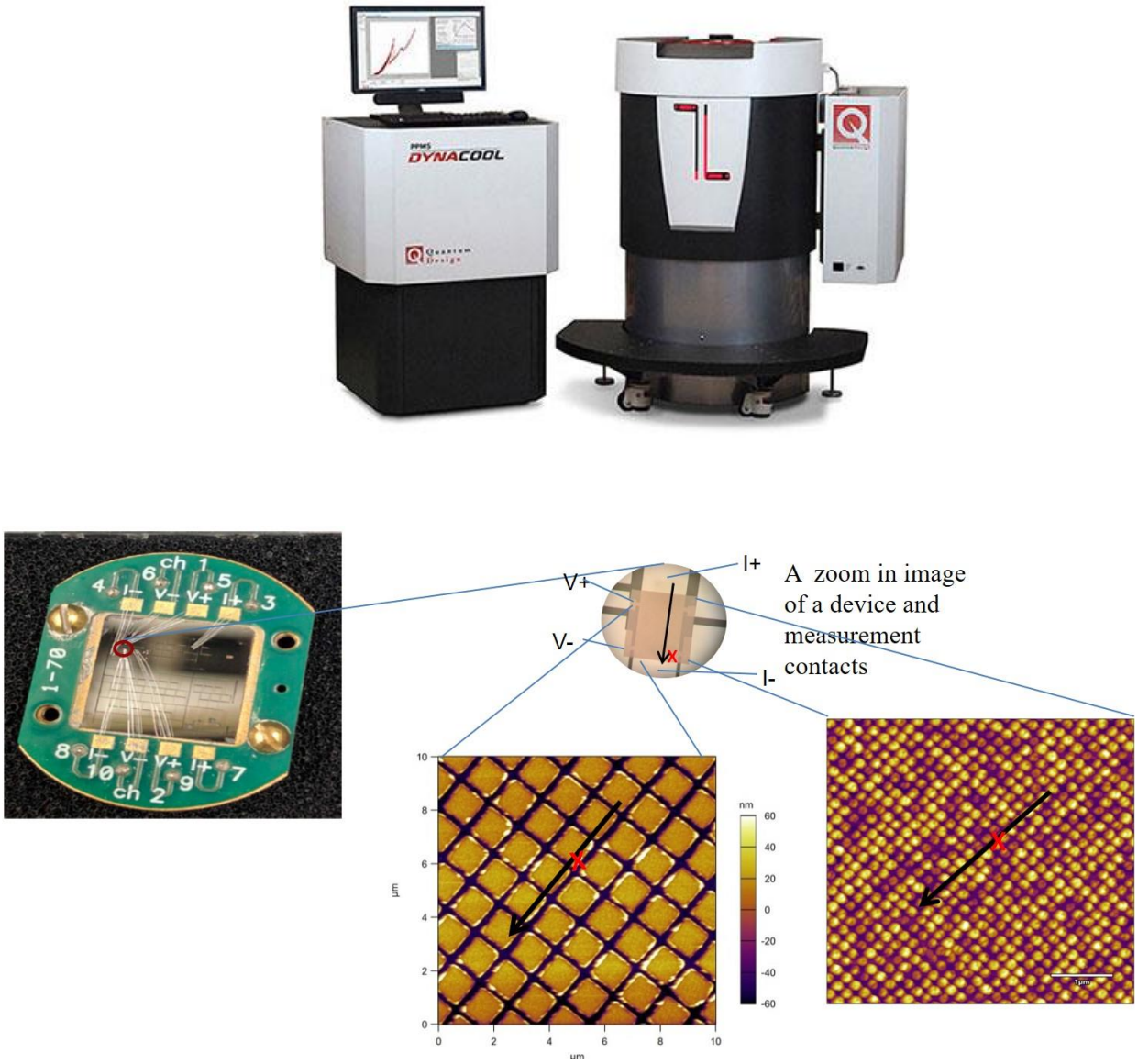


Zoomed in view of measured array which can be a square-island array or a nanodot-island array.

Figure 2.17 Upper panel is an image of a Dynacool PPMS system from company website, lower panel left is a PPMS sample mounting chuck with a real sample wafer on it. The area circled by red circle is the array.

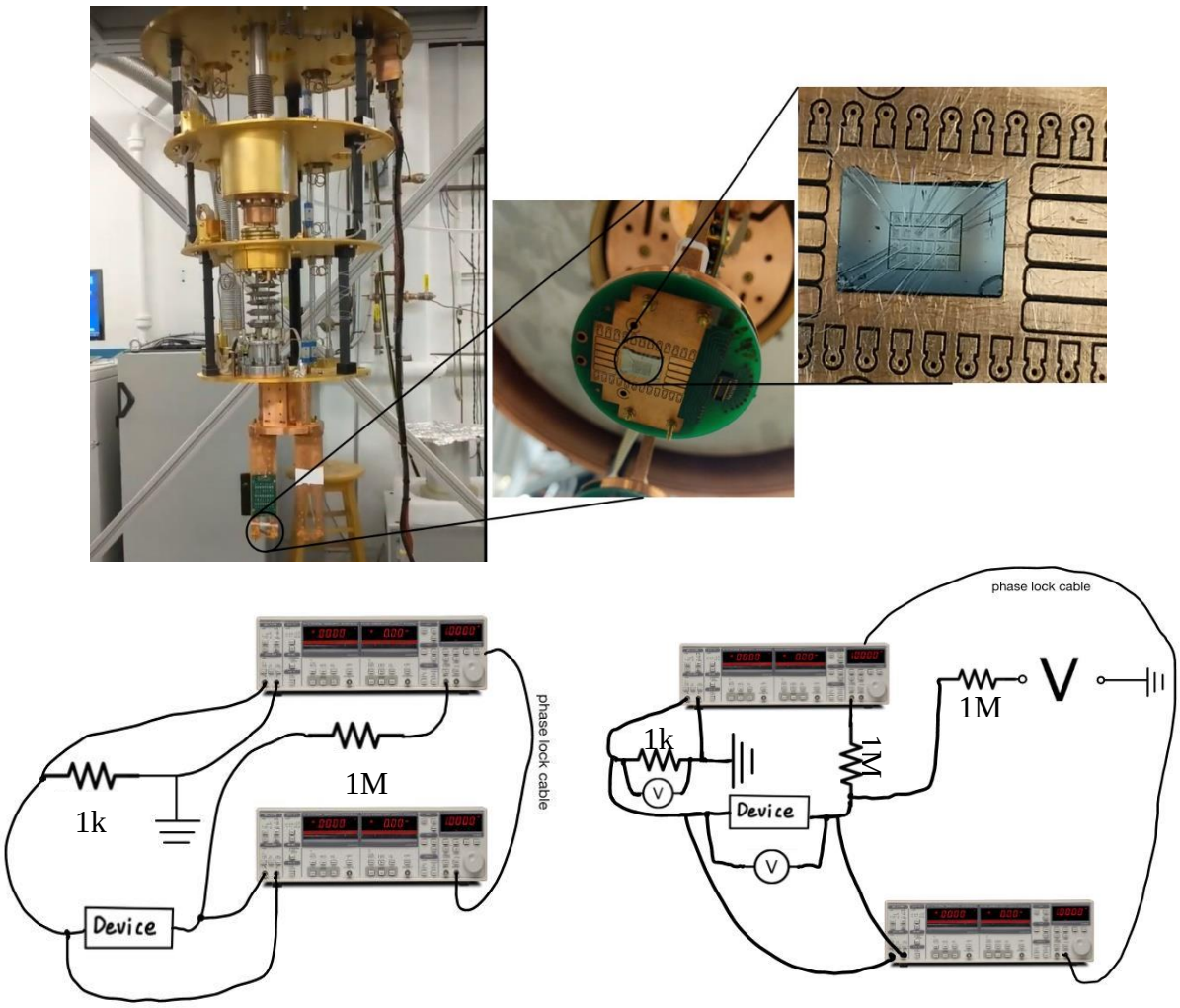


Figure 2.18 Top panel, from left to right, are photos of the dilution fridge without shields, sample mounting chip and a wafer with nanodot-island arrays on. Lower panel, on the left is the circuit diagram for measurement of complex R-T, on the right is the circuit diagram for dynamic V-I and dV/dI-I measurements. 1kΩ is the current sensing resistor, 1MΩ is the load resistor for lock-in and dc voltage source.

# CHAPTER 3: PROXIMITY INDUCED SUPERCONDUCTIVITY IN NIOBIUM - $BI_2SE_3$ ARRAYS

In this chapter, data from big square-island arrays fabricated on $Bi_2Se_3$ is presented and analyzed. Arrays consist of niobium island squares of length around 1um with various spacings (65nm to 320nm). Totally 11 arrays on 4 different $Bi_2Se_3$ films have been tested. All $Bi_2Se_3$ films are 60QL thick. Firstly, Hall effect results will be presented, film carrier density varies from 3.1 E+13/cm$^2$ to 6.7E+13/cm$^2$. Then results of R-T, R-B, and V-I characteristics will be presented and discussed.

## 3.1 Transport of $Bi_2Se_3$ films

For all films used in this study, Hall measurement was performed, results are summarized in figure 3.1.

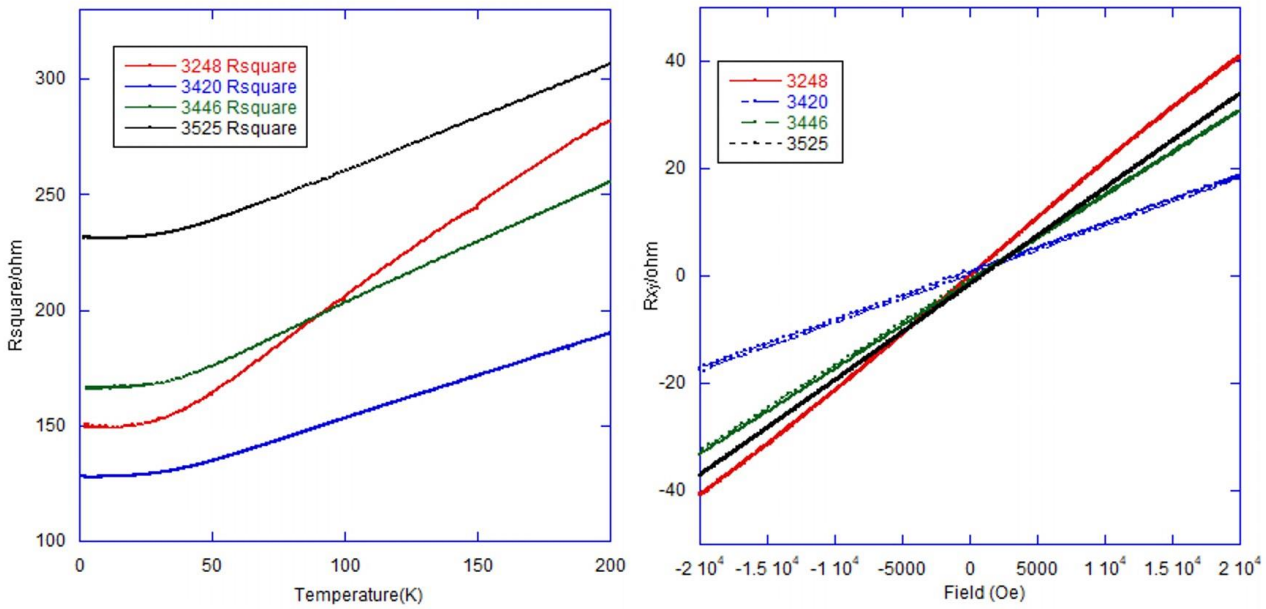


Figure 3.1 $R_{\square}$ and $R_{xy}$ vs temperature results. Left one shows temperature dependent $R_{\square}$ of four films, the right one shows $R_{xy}$ results of them.

Using the following formulas, carrier density and mobility and mean free path are obtained:

$$R_{\square} = \frac{V_+ - V_-}{I} \qquad (3\text{-}1)$$

$$n_{2D} = \frac{B}{eR_{xy}} \qquad (3\text{-}2)$$

$$\mu = \frac{1}{en_{2D}R_{\square}}\frac{q\tau}{m^*} = \frac{ql}{m^* v_F} = \frac{ql}{\hbar k_F} \qquad (3\text{-}3)$$

$$l = \frac{\mu\hbar k_F}{q}; \quad k_F = \sqrt{2\pi n} \qquad (3\text{-}4)$$

Here we assumed that carriers are 2D. Values obtained have been summarized in table 3.1.

| Film Index | Thickness (QL) | Carrier type | Carrier density ($/m^2$) | Mobility ($cm^2/Vs$) | Square resistance (Ω) | Mean Free Path (nm) |
|---|---|---|---|---|---|---|
| 3248 $Bi_2Se_3$ | 60 | n-type | 3.1E+17 | 1344 | 150.0 | 120 |
| 3420 $Bi_2Se_3$ | 60 | n-type | 6.7E+17 | 730 | 127.8 | 96 |
| 3446 $Bi_2Se_3$ | 60 | n-type | 3.9E+17 | 963 | 166.5 | 96 |
| 3525 $Bi_2Se_3$ | 60 | n-type | 3.5 E+17 | 800 | 223.0 | 75 |

Table 3.1Summary of carrier transport results and calculated mean free paths for four films used in big square-island arrays.

## 3.2 Low Temperature Resistive Transition Results

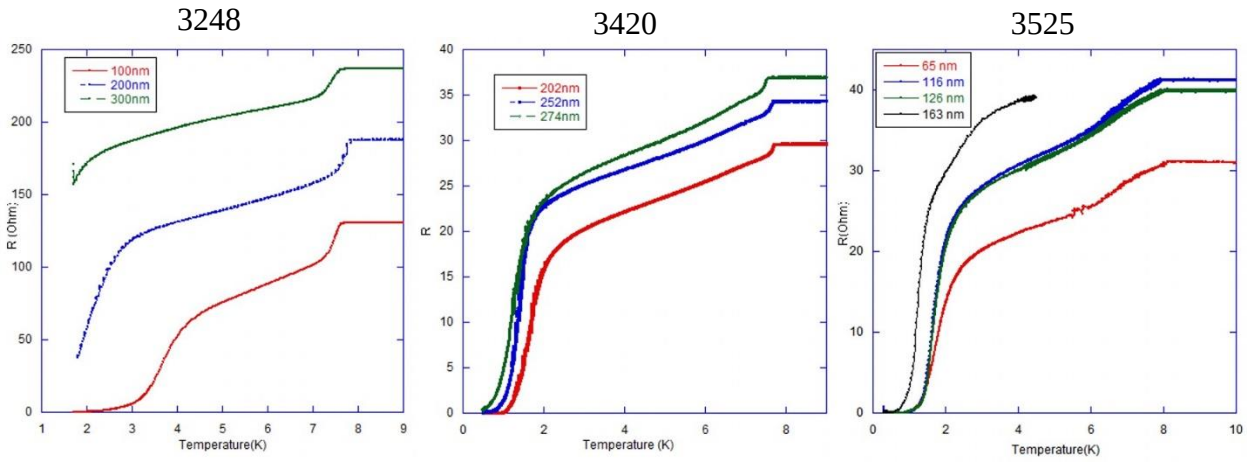


Figure 3.2 R vs T results of all measured arrays of three wafers, from left to right, 3248, 3420, 3525, respectively. The legends of each graph show the spacing size of each array. For arrays on 3248, resistance is of 5 square arrays, and because of limit of cooling ability , arrays did not reach zero-resistance.

The R-T results of measured arrays on three wafers are shown in figure 3.2. All R-T curves take similar shapes: arrays undergo a two-stage proximity effect and a phase locking transition at very low temperature. Due to limit of cooling ability, arrays on 3248 did not reach zero-resistance state. Smallest spacing array of 3420 and all arrays made on 3525 have reached zero resistance state, their data will be used for low temperature analysis while the 3248 one will contribute to the higher temperature analysis.

I will use the R-T result of smallest spacing array on 3420 to explain the physical process it undergoes as temperature is lowered. Figure 3.3 is the R-T curve of the 202nm spacing array on wafer 3420. Definitions of labeled temperatures are given in the caption. Above $T_{onset}$, array resistance is just the sum of normal niobium islands and $Bi_2Se_3$ film; resistance of niobium islands

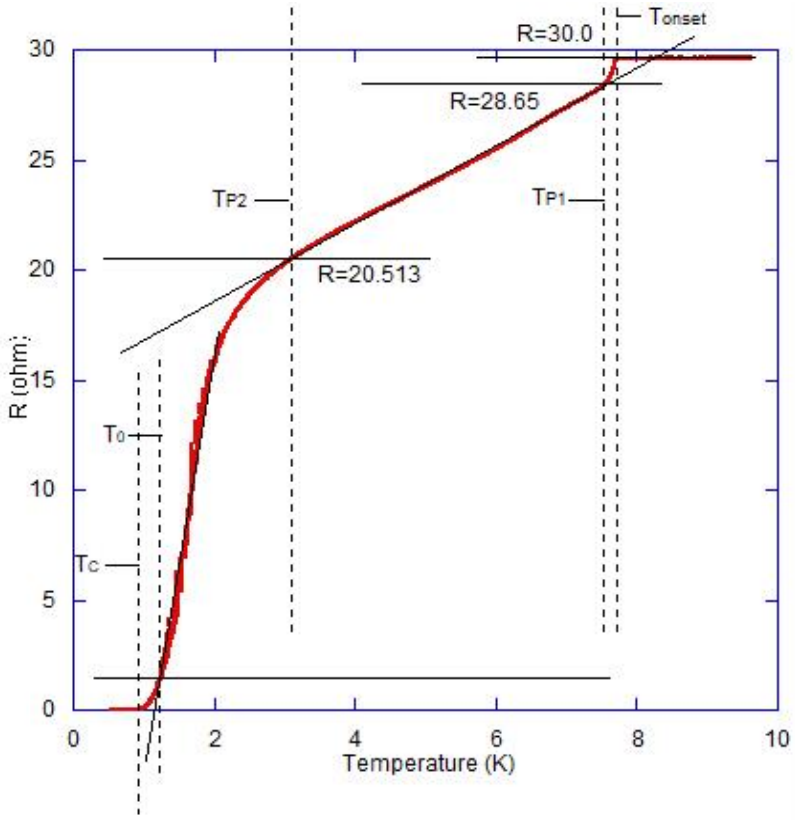


Figure 3.3 R vs T result of the 202nm spacing array made on wafer 3240. Definition of labeled temperatures: $T_{onset}$ is the temperature of niobium island; $T_{P1}$ is the first proximity effect onset temperature, the first proximity effect happens at interface of the film and islands; $T_{P2}$ is the second proximity effect temperature, it happens in the film area between islands; $T_0$ is the onset temperature from where the resistive behavior starts to deviate from linearity; $T_C$ is the temperature when entire array just reaches zero resistance.

drops to zero at $T_{P1}$, the resistance value labeled in the graph at $T_{P1}$ consists of resistance of film and contact resistance which will be discussed in the next section; between $T_{P1}$ and $T_{P2}$, proximity effect at interface of islands and film occurs, see figure 3.4 **A**, at $T_{P2}$, resistance mostly comes from the film area between islands; below $T_{P2}$ and above $T_0$, the second proximity effect plays the role, see figure 3.4 **B**, coherence length increases as temperature lowers, proximity effect propagates further from the niobium island source so the resistance keeps dropping. Starts from $T_0$, Josephson effect begins to show up. In following sections, detailed analysis of R-T above $T_0$ and below $T_0$ will be presented.

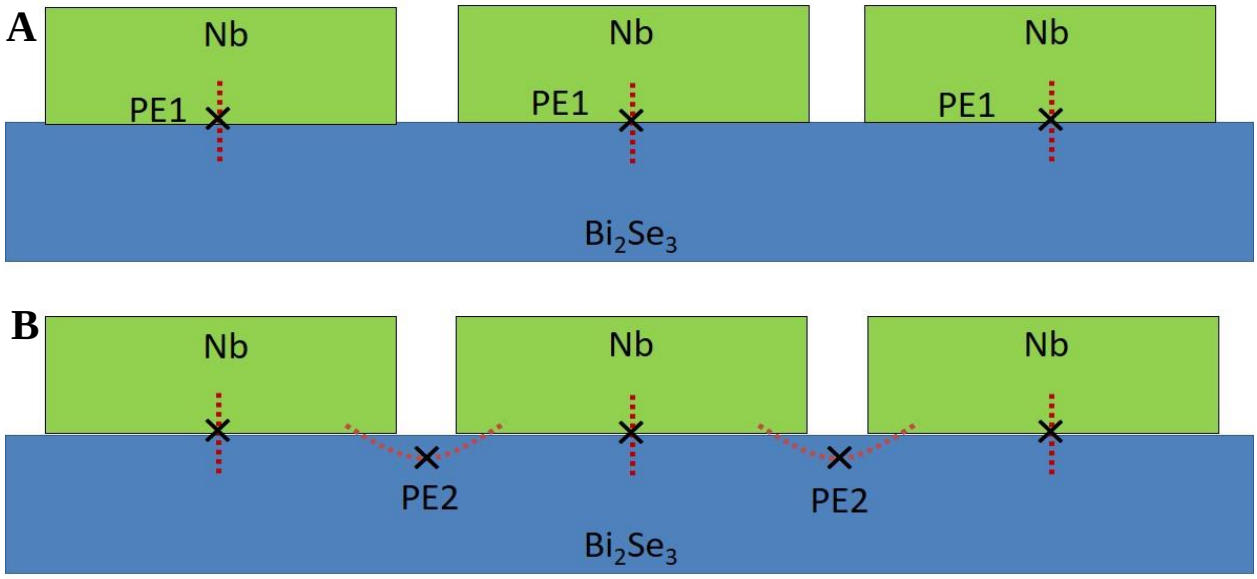


Figure 3.4 Cartoon drawings to illustrate two proximity effects. Panel **A** shows first proximity effect happens between niobium island and the film in direct contact underneath. Panel **B** shows the second proximity effect in the film area between two neighborhood islands. Josephson effect also happens at the area indicated by the second proximity effect.

A slight variation of onset temperature of niobium islands are observed but the trend cannot be related to neither the array size nor island size: for 3248, 200nm spacing array has higher onset transition temperature than the 100nm spacing one while for 3240 they are the same and for 3525 larger spacing one has lower onset temperature. In Serena Eley's work[85] of niobium island arrays on gold film, she proposed an explanation for spacing dependent onset transition

temperature that there is an inter-coupling energy $J'$ that helps stabilize fluctuations in granular niobium islands, therefore transition temperature is spacing dependent. In our research, the spacing variation is similar what her arrays have while the island size is larger, hers are 300nm diameter discs while ours are 1 by 1 um squares. The absence of spacing dependent onset transition temperature may be attributed to the large size of islands which indicates that phase fluctuation of grains of niobium is not as important for island of size of $1um^2$.

### 3.2.1 Resistance model above $T_{P1}$

#### *3.2.1.1 Transfer length of niobium island-$Bi_2Se_3$ contact*

In superconducting island array samples, a sudden drop in the array resistance is observed at the temperature where the island becomes superconducting. For samples like ours where the normal material has many fewer carriers than the superconductor, we ignore the effect of the normal film to the superconductivity in the islands and treat the sample resistance classically. At the island transition temperature, the resistance can be calculated by considering the resistance of the normal film to be unchanged. Then the resistance of the array consists of the series and parallel combination of the resistance of the normal film between the islands plus a contribution to the resistance from the transfer of current between the two layers.

To model this, we consider a somewhat simpler situation where an infinitely long normal strip of width *w* is covered by a zero-resistance layer extending from the origin to negative infinity in the *x*-direction as shown in the figure. The normal film has a two-dimensional sheet resistance of $R_{\square}$. The contribution to the series resistance due to the transfer of current from the zero resistance top layer to the normal film below is given by $R_{\text{tran}} = R_{\square}\eta/w$, where $\eta = 1/\sqrt{R_{\square}G_C}$ is known as the transfer length and $G_C$ is the specific contact conductance (SI units Siemens/$m^2$) characterizing the interface between the superconductor and the normal layer. This simple result can be derived from a straightforward model which we do here.

Figure 3.5 shows the model. Note that positive *x* extends to the left in the figure. An infinitely long ribbon of normal metal of width *w* is covered by a superconducting film that extends from $x = \infty$ to $x = 0$. The contact is characterized by the contact conductance $G_C$. We take the voltage of the superconductor to be zero, and the voltage in the normal film is a function of position, $V(x)$. This determines the current flow between the superconductor and the normal film underneath. The local current density between the superconductor and the normal film is given by $J_C(x) = G_C V(x)$. The two-dimensional sheet current density in the normal film at coordinate *x* is given by the sum of the currents entering the film "upstream" of *x*, or $K(x) = \int_{\infty}^{x} dx' J_C(x')$.

Since $dV/dx = R_{\square} wK(x)$,

we obtain

$$\frac{d^2}{dx^2}V(x) = G_C R_{\square} V(x)$$

which is solved by $V(x) = V(0)e^{-x\sqrt{G_C R_{\square}}}$. The physical significance of $V(0)$ is that it is the voltage in the normal layer that

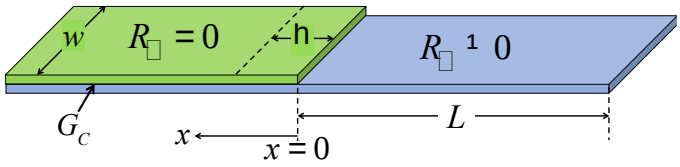


Figure 3.5 Transfer length model calculation. The superconducting layer (green) ends at $x = 0$. The normal layer is covered by superconductor and extends beyond.

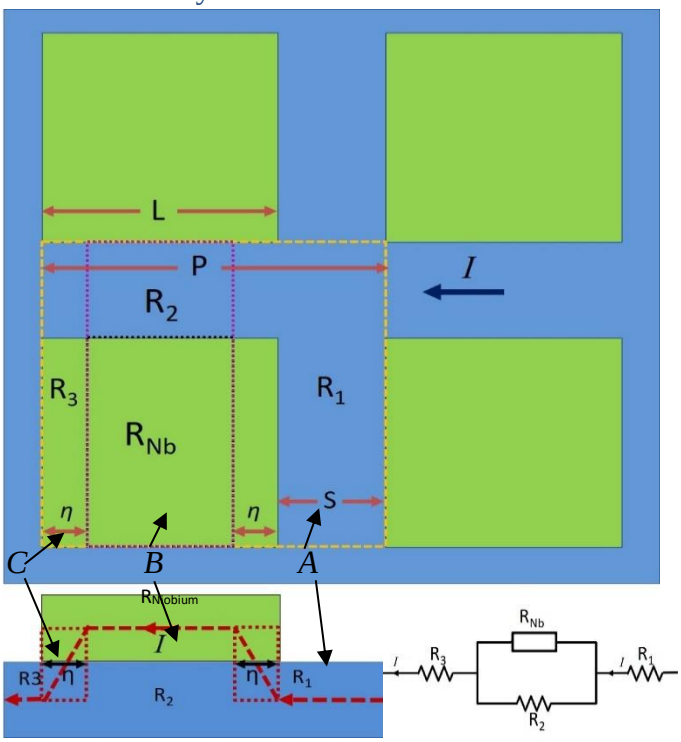


Figure 3.6 Top and Side view of part of the island - array. A unit cell is boxed by the yellow dashed line, blue region is $Bi_2Se_3$ film, green region is Niobium island, current flows from left to right as indicated by the black arrow. The lower right is the modeled effective circuit, contact resistance is not considered here because it is very small (less than 1Ω, estimated from 202nm spacing array).

arises from the transfer of current from the zero resistance layer completely into the normal layer. Using this solution to evaluate $K(0) = I/w$, we find that

$$I = wK(0) = G_C V(0) \int_{\infty}^{0} dx\, e^{-x\sqrt{G_C R_\square}} = -G_C \frac{V(0)}{\sqrt{G_C R_\square}} \qquad (3\text{-}5)$$

The additional resistance that this adds to the transport in the normal film to the right of the origin is $\sqrt{R_\square / G_C} = \eta R_\square$ where $\eta = 1/\sqrt{G_C R_\square}$ is the exponential current transfer length. This is the result we set out to prove. There are certainly limitations on this result. It does not cover the case where the superconductivity influences transport in the normal conductor via a proximity effect. Typically, this occurs at temperatures well below the transition temperature of the superconductor or in samples with thin normal layers such that critical distances that characterize electronic motion such as the mean free path are not large compared to the sample thickness.

The result proved above can be applied to the island array to obtain transfer length and $G_C$ from *R-T* results. The resistance of an array can be analyzed by studying a unit cell as shown in Figure 3.6. In Figure 3.6, the unit cell is boxed by a yellow dashed line, ***S*** is spacing size between islands, ***P*** is length of the square unit cell, ***L*** is length of niobium island. Current transfers from the $Bi_2Se_3$ into the niobium film over an exponential transfer length $\eta = \sqrt{\frac{1}{G_C R_{\square film}}}$, where $G_C$(S/m$^2$) is the specific contact conductance between the layers and $R_{\square film}$ is the sheet resistance of the $Bi_2Se_3$ film. The unit cell is divided into three resistance regions (*A,B,C* from right to left) by the red dashed line rectangular box. Resistance of region *A* and *C* purely come from $Bi_2Se_3$ film and can be expressed as:

$$R_A = \frac{S + \eta}{P} R_{\square film}$$

$$R_C = \frac{\eta}{P} R_{\square film}$$

Resistance of region *B* can be expressed as:

$$\frac{1}{R_B} = \frac{1}{R_2} + \frac{1}{R_{Nb}} = \frac{1}{\frac{L - 2\eta}{P} R_{\square film}} + \frac{1}{R_{Nb}}$$

$$R_{Nb} = \frac{L}{L - 2\eta} R_{\square Nb}$$

$R_{\square Nb}$ is the sheet resistance of niobium. The total resistance of the unit cell which is also the total resistance of a square array is :

$$R_{\square array} = R_A + R_B + R_C = \frac{S+2\eta}{P} R_{\square film} + \frac{R_{Nb} \times \frac{L-2\eta}{P} R_{\square film}}{\frac{L-2\eta}{P} R_{\square film} + R_{Nb}} \qquad (3\text{-}6)$$

With this formula now we can use the R-T data to calculate η and $G_C$. 100nm spacing array of wafer 3248 will be used as the example and then η and $G_C$ of 202nm spacing array of wafer 3240 will also be calculated for the purpose of comparing $G_C$ between these two wafers.

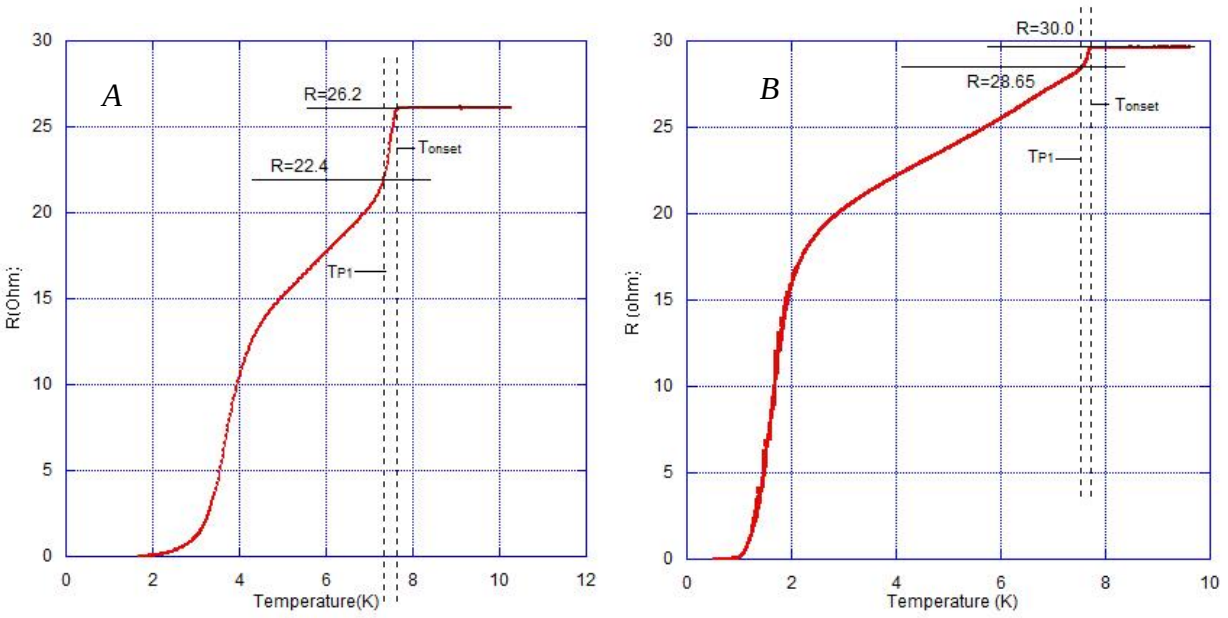


Figure 3.7 Plot *A* is R-T curve of the 100nm spacing array on wafer 3248; Plot *B* is R-T curve of the 202nm spacing array on wafer 3420. $T_{onset}$ is the onset temperature of niobium, $T_{P1}$ is the onset temperature of proximity effect under niobium islands, at $T_{P1}$ resistance of niobium islands are zero.

When resistance of niobium islands is zero, formula (3-6) takes a simpler form:

$$R_{\square array} = R_A + R_B + R_C = \frac{S+2\eta}{P} R_{\square film} \qquad (3\text{-}7)$$

From plot *A* of figure 3.7, we know the resistance at $T_{P1}$ for 100nm spacing array on wafer 3248 is 22.4(Ω), this number is for one square of the array so can be directly plugged into the formula (3-7). With knowledge of the two-dimensional sheet resistance of 3248 $Bi_2Se_3$ film which is 150 (Ω) , η and $G_C$ can be obtained:

$$\eta = \frac{1}{2}\left(\frac{R_{\square array}}{R_{\square film}} \times P - S\right) = \frac{1}{2}\left(\frac{22.4}{150} \times 1.1 - 0.1\right) = 0.0321(um)$$

$$G_C = \frac{1}{\eta^2 R_{\square film}} = 6.47E + 12(S/m^2)$$

η and $G_C$ of 202nm spacing array of 3420 can be obtained using the same method:

$$\eta = 0.0425\ (um)$$

$$G_C = 4.33E + 12(S/m^2)$$

η and $G_C$ for all arrays of these two wafers have been summarized in Table 3.2.

| Index | Thickness (QL) | Pitch (um) | Spacing (um) | Island Length (um) | $R_{\square array}$ ($T_{P1}$) | η (nm) | $G_C$(S/m²) |
|---|---|---|---|---|---|---|---|
| 3248(A)G | 60 | 1.10 | 0.100 | 1.00 | 22.40 | 32.1 | 6.47E+12 |
| 3248 E | 60 | 1.20 | 0.200 | 1.00 | 33.60 | 33.9 | 5.80E+12 |
| 3248 D | 60 | 1.30 | 0.319 | 0.981 | 44.00 | 30.6 | 7.12E+12 |
| 3420(B) | 60 | 1.28 | 0.202 | 1.078 | 28.65 | 42.5 | 4.33E+12 |
| 3420 | 60 | 1.30 | 0.252 | 1.048 | 33.17 | 42.7 | 4.29E+12 |
| 3420 | 60 | 1.32 | 0.274 | 1.046 | 35.62 | 41.0 | 4.65E+12 |

Table 3.2 Summary of sizes, $\eta$ and $G_C$ of 3248 and 3420 arrays

### *3.2.1.2 Surface roughness-dependent $G_C$*

In this section we will prove that the ab-plane conductance of $Bi_2Se_3$ is much larger that c-axis conductance and this difference contributes to the difference of $G_C$ and tunneling transmission coefficient $|T|^2$.

In the previous section we have derived and calculated $G_C$ for two wafers, see Table 3.2. Now we firstly derive a formula for $|T|^2$. The transmission coefficient here is a measure of probability of wavefunctions transfer through the junction between Niobium and $Bi_2Se_3$. In the case that the junction is purely planar, the formula for $|T|^2$ can be expressed as :

$$G_C = \frac{2e^2}{h} N|T|^2 \qquad (3\text{-}8)$$

$$N = \left(\frac{2}{\lambda_F}\right)^2 \qquad (3\text{-}9)$$

*N* is number of quantum conducting channels per unit area, $\lambda_F$ is the fermi wavelength of $Bi_2Se_3$ film. In actual experiment, there are two types of junction conducting channels. See figure 3.8, one is the c-axis channel indicated by black arrows, the other one is ab-plane channel indicated by red arrows. Define the c-axis channel conductance to be $G_T$, ab-plane conductance to be $G_{ab}$.

$$G_C = G_T + G_{ab}\frac{area\ of\ steps}{unit\ planar\ area} = \frac{2e^2}{h}N_T|T|_T{}^2 + \frac{2e^2}{h}N_{ab}|T|_{ab}{}^2 \qquad (3\text{-}10)$$

$$N_T = (\frac{2}{\lambda_F})^2 \qquad (3\text{-}11)$$

$$N_{ab} = \frac{1}{l\cdot\lambda_F} \qquad (3\text{-}12)$$

$1/l$ is step length per unit area.

In Figure 3.8, AFM of two films show very different morphologies: ***A*** has a lot of spiral dislocations while ***B*** is essentially flat. For type ***A*** film, $G_{ab}$ has unneglectable contribution while for type ***B***, $G_C$ is basically equal to $G_T$. Film 3248 falls into the type ***A*** category and 3420 falls into the type ***B*** category because different growth procedures were used for each one respectively. Now we will use equation (3-10)-(3-12) to derive $G_T$, $T_T$ and $G_{ab}$, $T_{ab}$.

The step length in AFM of type A film is about 30 to 50 nm, we use 40nm to do the calculation, step size is height of QL which is 1nm. From Hall measurement, carrier density of film 3248 and film 3420 is 3.1E+13/cm$^2$ and 6.7E+13/cm$^2$, respectively, assuming all carriers are 2D so $\lambda_F = \sqrt{\frac{2\pi}{n_{2D}}}$. $G_T$ of 3248 is about half of it of 3420. Put all these numbers into equation (3-10), one can obtain:

$$\frac{G_{ab}}{G_T} = 80$$

$G_{ab}$ *and* $G_T$ here are both for film 3248.

This number of course may change depending on how the number of steps is counted and how the step length is estimated as well as the value $\lambda_F$ but the conclusion that $G_{ab}$ is much larger than $G_T$ should remain valid. If instead assuming all carriers are bulk carries, the $G_{ab}/G_T$ will be about 74.

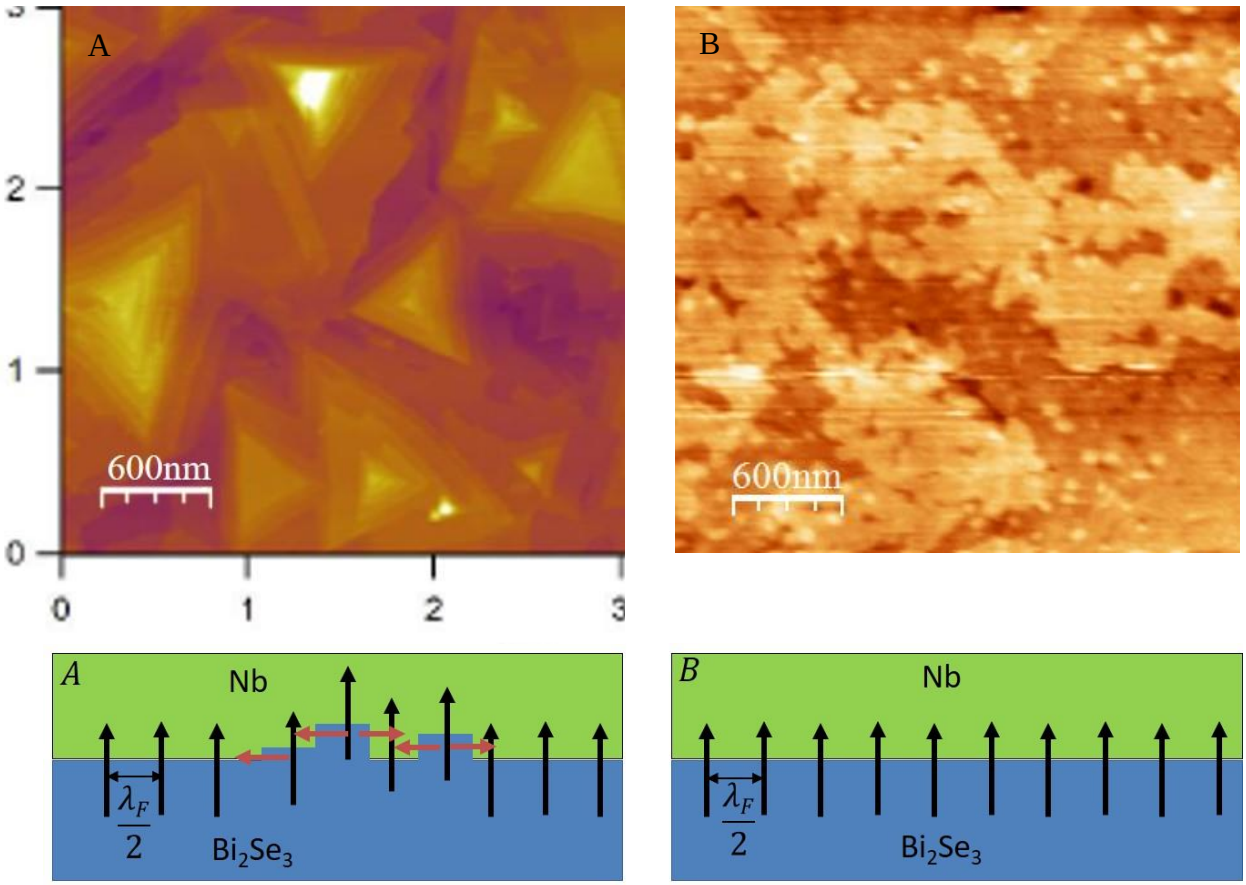


Figure 3.8 Upper left AFM ***A*** shows representative morphology of film 3248, ***B*** shows representative morphology of film 3420. The lower part are two drawing illustrating junction conductance channels at interface of niobium and these two different surface morphologies.

### *3.2.1.3 Junction tunneling coefficient $|T|^2$*

For film 3248, assuming all carrier are 2D so $\lambda_F$=4.5nm, from formula (3-10—3.6-12), one can obtain:

$$\frac{|T|^2_{ab}}{|T|^2_T} = \frac{G_{ab}}{G_T}\frac{area\ of\ steps}{unit\ planar\ area}\cdot\frac{N_T}{N_{ab}} = 70.7$$

This result shows that the planar tunneling probability is much higher than the c-axis one. This is also consistent with the proved difficulty of proximity effect along c-axis in bilayer Niobium-$Bi_2Se_3$ system studied by ARPES[86].

### 3.2.2 Transport between $T_{P1}$ and $T_{P2}$

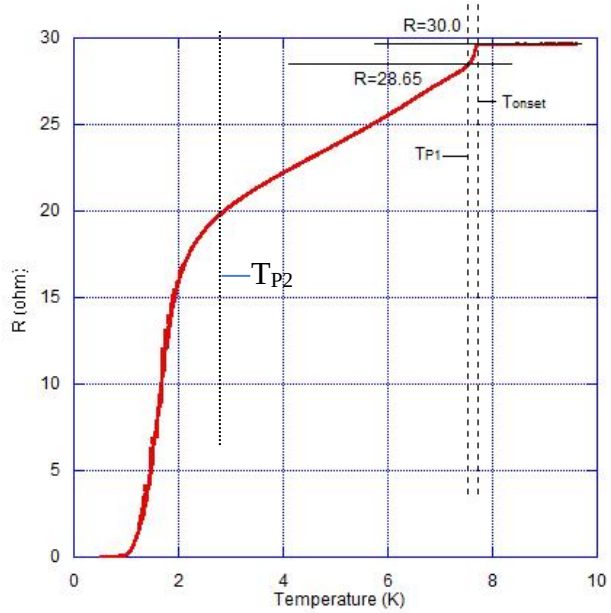


Figure 3.9. R-T curve of 202nm spacing array fabricated on film 3420.

As shown in figure 3.9, resistance between $T_{P1}$ and $T_{P2}$ decreases linearly with temperature. From $R_{\square}$ measurement of bare film, see figure 3.1, resistance of $Bi_2Se_3$ does not vary a lot at low temperature region (below 20K) so the change of resistance of array must be caused by niobium islands, or in other words, the superconducting proximity effect. As already explained at the beginning of this chapter, there are two types of proximity effect, the interfacial one that happens at the interface of each island and the film area underneath it and the inter-island one that occurs at the area between nearest islands. The proximity effect between $T_{P1}$ and $T_{P2}$ is the interfacial kind. As temperature lowers, proximity effect penetrates deeper and spreads wider into contacting area under each island, the contact conductance increases, and transfer length becomes shorter. At $T_{P2}$, contact resistance should be very small or even near zero and resistance mostly come from area between islands. For the R-T curve of 202 nm spacing array shown in figure 3.9, the extracted resistance $R_{TP2}$ at $T_{P2}$ is 20.53ohms, compared with the resistance $R_{spacing}$ from area between two nearest islands which can be obtained as following:

$$\frac{202nm}{1280nm} \times 127.8ohms = 20.16(\Omega)$$

These two number are essentially the same which support the argument that the resistance solely comes from film area connecting two islands. In the equation, 202nm is the spacing, 1.28um is the pitch size and 127.8ohms is $R_{\square}$ of film 3420. Values of $R_{TP2}$ and $R_{spacing}$ are summarized in table 3.3.

| Film index | Spacing(nm) | Pitch(um) | R□ | $R_{spacing}$ | $R_{TP2}$ |
|---|---|---|---|---|---|
| 3248 | 100 | 1.10 | 150.0 | 13.63 | 14.10 |
| | 200 | 1.20 | 150.0 | 25.00 | 25.27 |
| | 300 | 1.30 | 150.0 | 34.60 | 36.66 |
| 3420 | 202 | 1.28 | 127.8 | 20.16 | 20.53 |
| | 252 | 1.30 | 127.8 | 24.77 | 24.89 |

Table 3.3 Summary of $R_{TP2}$ and $R_{spacing}$ from sample 3248 and 3420. The 274nm spacing array of 3420 is not shown for its spacing is very close to the 256nm spacing one.

Now let us take a look at the spacing dependence of $T_{P2}$. $T_{P2}$ of three arrays of film 3248 are plotted in figure 3.10. At $T_{P2}$, the current consists both supercurrent (from superconducting niobium islands) and normal current (film between islands). As spacing between islands increases, it takes lower temperature for area between islands become supercondcuting, so $T_{P2}$ decreases linearly with incrasing spacing. This can also be explained by the increasing of coherence length of $Bi_2Se_3$ as temperature decreases. Phase information from a supercondcuting niobium island is carried by carriers in $Bi_2Se_3$ as current travels furthur away from the island. The inset of figure 3.10 shows the linear dependence of $T_{P2}$ of spacing, and if follows the trend it predicts that around spacing of 560nm $T_{P2}$ will be zero which means the array will reach a metalic state as demonstrated by Serena Eley in her paper. Although the 560nm crossover spacing is very carelessly estimated, it is possible the whole array can reach a static metalic states since the spacing can always be made longer than zero temperature coherence length of $Bi_2Se_3$, it will be interesting to see wheather an array can reach an insulating state by increasing the spacing and decreasing the island size (it is not likely because the sheet resistance of $Bi_2Se_3$ is very small compare to quantum of resistance which is $h/4e^2$=6.45kΩ which is the superconducting-insulating crossover shunting resistance for a Josephson junction[87])

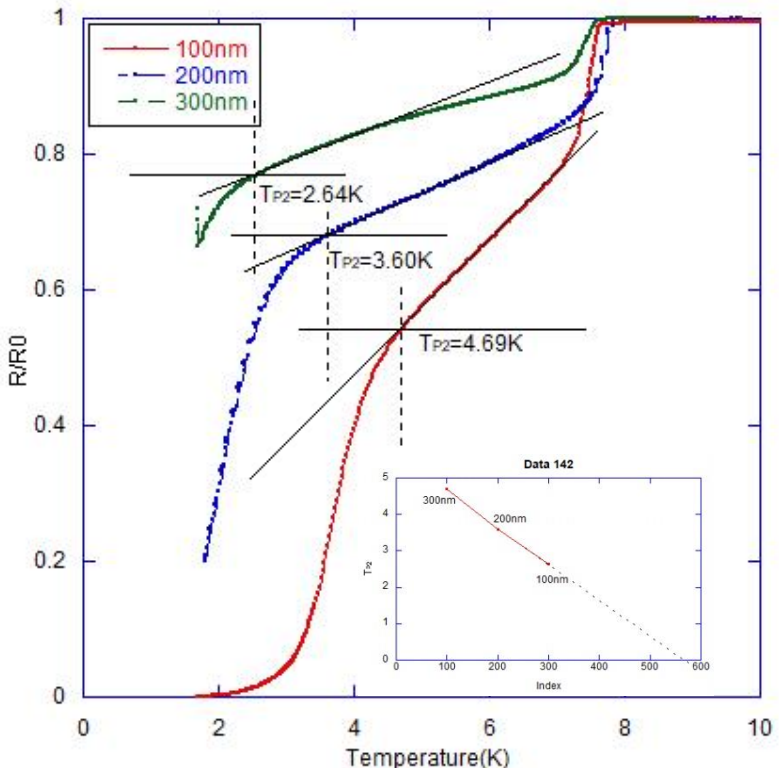


Figure 3.10 R-T results of three arrays fabricated on film 3248. Resistance has been normalized to normal state resistance $R_0$ respectively for each array. Value of $T_{P2}$ is indicated. $T_{P2}$ are plotted verse spacing in the inset, it shows a clear linear trend and intersects with zero temperature at spacing about 560nm.

Inset of figure 3.11 summrizes $T_{P2}$ of 9 arrays fabricated on film 3248, 3420, and 3525. For arrays on the same film, $T_{P2}$ decreases as the ratio of spacing to pitch, s/p, increases, as expected. Film dependence of $T_{P2}$ is very obvious. 3248 arrays have the highest $T_{P2}$, 3420 arrays $T_{P2}$ are in the middle, 3525 arrays have the lowest $T_{P2}$. Film dependent $T_{P2}$ cannot be explained solely by film properties of mean free path, mobility or carrier densty listed in table 3.1.1. It is possbile that contact resistance is the key factor affecting $T_{P2}$. Comparing the R-T curves of 200nm spacing array of 3248 and 202nm spacing array of 3420 in figure 3.11, one finds that $T_{P2}$ of 3248 is higher that it of 3420. Two arrays were fabricated using the same process so the contact quality should be the same. But their contact resistances are different. As discussed in the contact conductance section, contact conductace of bumpier films are higher than it of flatter films. The array wih higher conducatnce (200nm spacing of 3248) therefore has higher $T_{P2}$ than the one with lower contact conductance (202nm spacing of 3420). For the $T_{P2}$ difference between 3420 arrays and 3525 arrays, although their contact resistances are comparable because they both have flat

surface, film 3525 has higher sheet resistance and shorter mean free path. This can explain why 3525 arrays have lower $T_{P2}$.

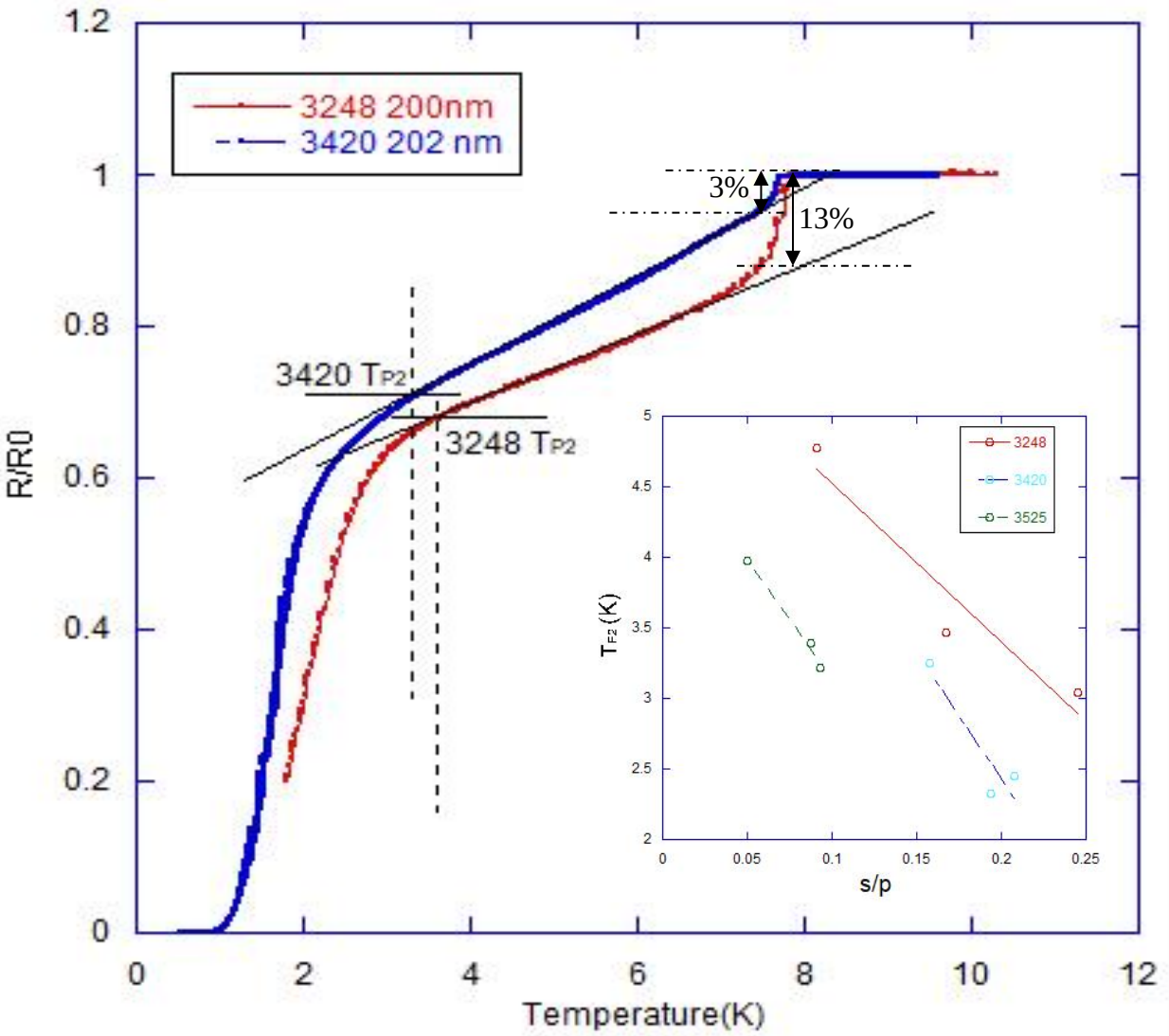


Figure 3.11 R-T results of 200nm spacing array on film 3248 and 202nm spacing array on 3420 and spacing-dependent $T_{P2}$. Resistance has been normalized to normal state resistance $R_0$ respectively for each array. $T_{P2}$ of 3248 is higher than it of 3420. Another thing needs to be pointed out is that the percentage drop from superconducting transition of niobium islands for 3248 which is 13% is much bigger than it of 3420 which is 3%. This is due to the smaller contact conductance of 3420 which has been discussed in section 3.2.1. The inset is a plot of $T_{P2}$ vs s/p of arrays on three films, 3248, 3420, and 3525, s/p is a unitless factor of spacing divided by pitch size, data are summarized in table 3.4.

### 3.2.3 Transport between $T_0$ and $T_{P2}$

We again use the R-T curve of 202nm spacing array as an example to explain the temperature dependent resistance above $T_0$ but below $T_{P2}$. Look at the Figure 3.12, the R-T curve experiences a slop change at $T_{P2}$. The steeper temperature dependence below $T_{P2}$ can be attributed to the increase coherence length of both niobium and $Bi_2Se_3$ and the fact that in this temperature range the dominate proximity effect is happening in ab-plane. As have been shown in previous

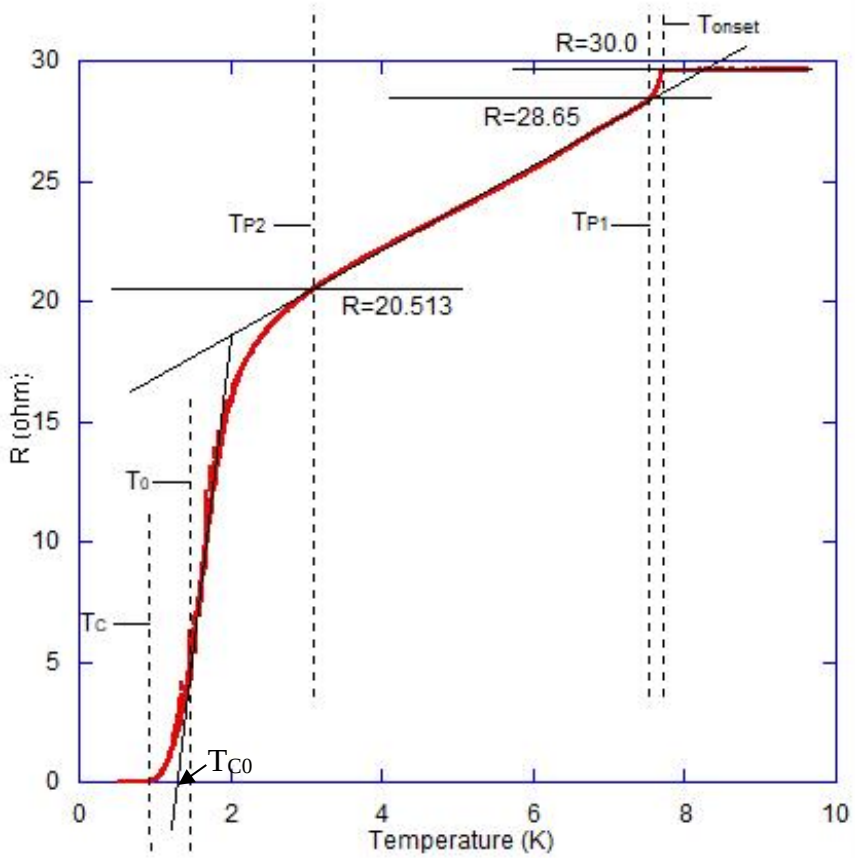


Figure 3.12 R vs T result of the 202nm spacing array made on wafer 3240. Two lines overlapping with the R-T curve indicating linear R-T dependence at corresponding temperature range. Definition of indicated temperature: $T_{onset}$ is the temperature of niobium island; $T_{P1}$ is the first proximity effect onset temperature, the first proximity effect happens at interface of the film and islands; $T_{P2}$ is the second proximity effect temperature, it happens in the film area between islands; $T_0$ is the onset temperature from where the resistive behavior starts to deviate from linearity;$T_{C0}$ is the crossing point of extrapolated linear line and temperature axis. $T_C$ is the temperature when entire array has zero resistance.

section, superconducting proximity effect in $Bi_2Se_3$ is much stronger in ab-plane than it is in c-lace direction due to different contact conductance and tunneling coefficient.

### 3.2.4 Transport below $T_0$

$T_0$ is defined as the temperature where R-T curve starts to deviate from linear relation and below which the BKT transition dominates, $T_C$ is where the resistance of an array becomes zero. In between $T_C$ and $T_0$, $T_{C0}$ is the crossing point of zero resistance axis and the extrapolated linear R-T line, see figure 3.12. We were only able to get R-T data below $T_0$ for 202nm spacing array of 3420 and arrays on 3525, and only these arrays reached zero-resistance stage because of their mean free paths are long enough. For film 3420, mean free path is 96nm, at base temperature of 0.7K of PPMS , spacings of 250nm and 274nm are too big for mean free path and coherence length to establish phase coherence among all islands. Arrays of film 3525 were measured in a $He_3$ dilution

| Array Index | Spacing /um | Pitch/um | S/P | Tc(K) | $T_{BKT}$ from fitting (K) | $T_{BKTo}$ from fitting (K) | $T_{C0}$ (K) | $T_0$(K) | $T_{P2}$(K) |
|---|---|---|---|---|---|---|---|---|---|
| 3248 100nm | 0.1 | 1.1 | 0.090909 | NA | 1.78 | 3.12 | 3.10 | 3.40 | 4.78 |
| 3248 201nm | 0.201 | 1.2 | 0.1675 | NA | NA | NA | 1.37 | NA | 3.47 |
| 3248 319nm | 0.319 | 1.3 | 0.24538 | NA | NA | NA | NA | NA | 3.04 |
| 3420 202nm | 0.202 | 1.28 | 0.15781 | 0.90 | 0.92 | 1.19 | 1.26 | 1.43 | 3.25 |
| 3420 252nm | 0.252 | 1.3 | 0.19385 | NA | 0.57 | 1.13 | 1.12 | 1.26 | 2.32 |
| 3420 274nm | 0.274 | 1.32 | 0.20758 | NA | 0.31 | 0.86 | 0.89 | 1.09 | 2.45 |
| 3525 65nm | 0.065 | 1.3 | 0.05 | 0.90 | 0.89 | 1.32 | 1.34 | 1.51 | 3.97 |
| 3525 116nm | 0.116 | 1.33 | 0.087218 | 0.85 | 0.82 | 1.38 | 1.37 | 1.46 | 3.39 |
| 3525 126nm | 0.126 | 1.35 | 0.093333 | NA | NA | NA | 1.39 | 1.48 | 3.22 |
| 3525 163nm | 0.163 | 1.38 | 0.11812 | 0.48 | 0.52 | 1.08 | 1.02 | 1.14 | NA |

Table 3.4. Summary of sizes and $T_C$, $T_{C0}$, $T_0$, and $T_{P2}$ of arrays on 3248, 3420 and 3525. Boxes labeled as NA mean data not available due to limited base temperature, for 163nm of 3525, $T_{P2}$ is missing because R-T data misses high temperature part. $T_{BKT}$ and $T_{BKTo}$ are temperatures obtained from fitting R-T data to BKT transition formula, the latter one is the onset temperature of BKT transition . Noticing that $T_{BKT}$ and $T_{BKTo}$ of 116nm spacing array of 3525 are less than 1/2 of $T_{BKT}$ and $T_{BKTo}$ of 100nm array of 3248, this is because of 3248 has rougher surface which results a higher contact conductance.

fridge in Professor Alexey Bezryadin's lab by his student Xiangyu Song. That fridge has 300mK cooling ability. Although film 3525 has shorter mean free path, at 300mK zero-resistance stage of all four arrays were reached. $T_C$ and $T_0$ are summarized in table 3.4 and plotted vs s/p in figure

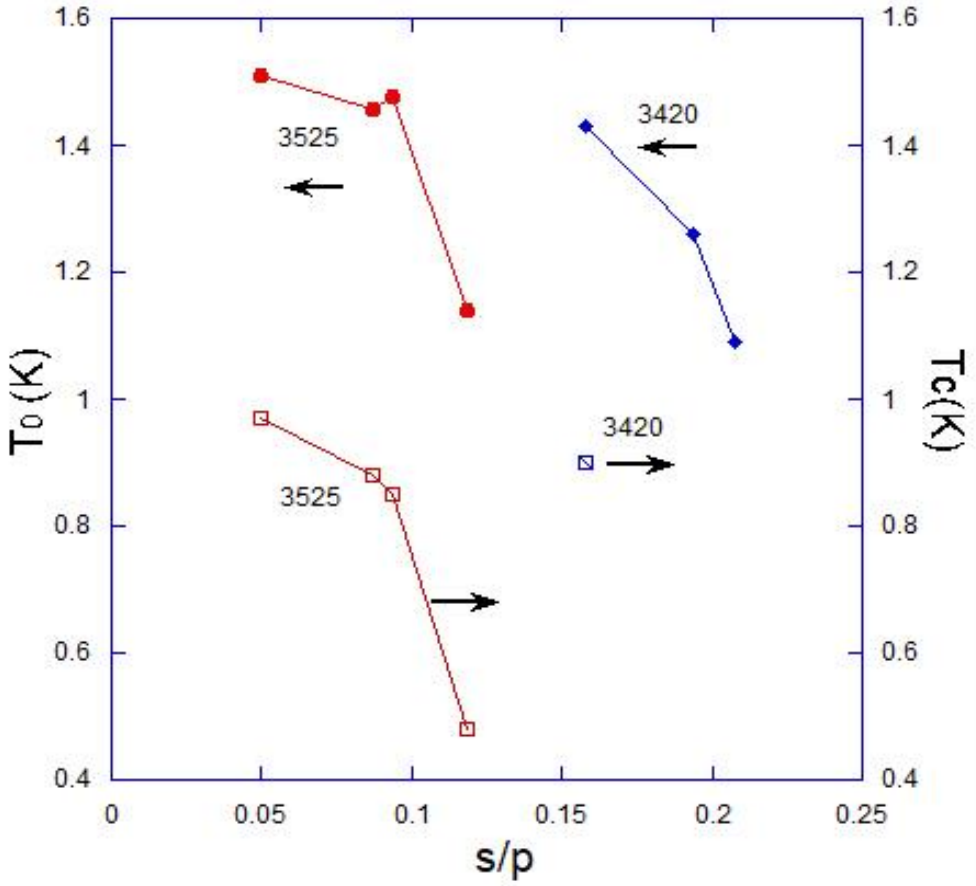


Figure 3.13 $T_0$ and $T_C$ of 3420 and 3525 vs spacing/pitch (s/p). Left axis is the $T_0$, right axis is the Tc ( zero resistance temperature). The temperature difference, $T_0$-$T_C$, does not vary a lot as s/p changes for arrays made on film 3525, assuming this also applies to arrays made on 3420, we can estimate their $T_C$.

3.13. Both $T_0$ and $T_C$ are s/p dependent, as s/p increases, they decrease. $T_0$ and $T_C$ of arrays on 3525, if extend s/p to bigger values, will be lower than them of arrays on 3420, this may be attributed to shorter mean free path of film 3525. The difference between $T_0$ and $T_C$ is about 0.5~0.6K for arrays on 3525. Although only Tc of 202 nm array of 3420 was obtained from experiment, one can predict $T_C$ of the 252nm and 274nm arrays, assuming the difference between $T_0$ and $T_C$ does not differ a lot for various s/p, are 0.6~0.7K and 0.5~0.6K, respectively.

BKT temperature can be estimated using the standard formula for BKT transition:

$$R(T) = R_0\, exp\left(-A\sqrt{T_{BKT}/(T - T_{BKT})}\right) \qquad (3\text{-}13)$$

A is a constant.

This can be simplified to :

$$R(T) \sim exp\left(-B/\sqrt{T}\right) \qquad (3\text{-}14)$$

Below a certain temperature and above the BKT temperature, R-T data can be fitted to this formula, and if plot ln(R(T)) vs $1/\sqrt{T}$, the fitting is simply linear. Data of six arrays have been fitted to this formula, see figure 3.14. We use $\ln(R/R_0)$ as Y-axis and decide that when $R/R_0$=0.001(that is $\ln(R/R_0) \approx -7$), resistance is considered as zero. For a small range of temperature (0.2~0.5K, dependents on specific array), data fits very well and show a clear linear dependence which confirms that arrays reach zero-resistance with assistance of vortex-antivortex

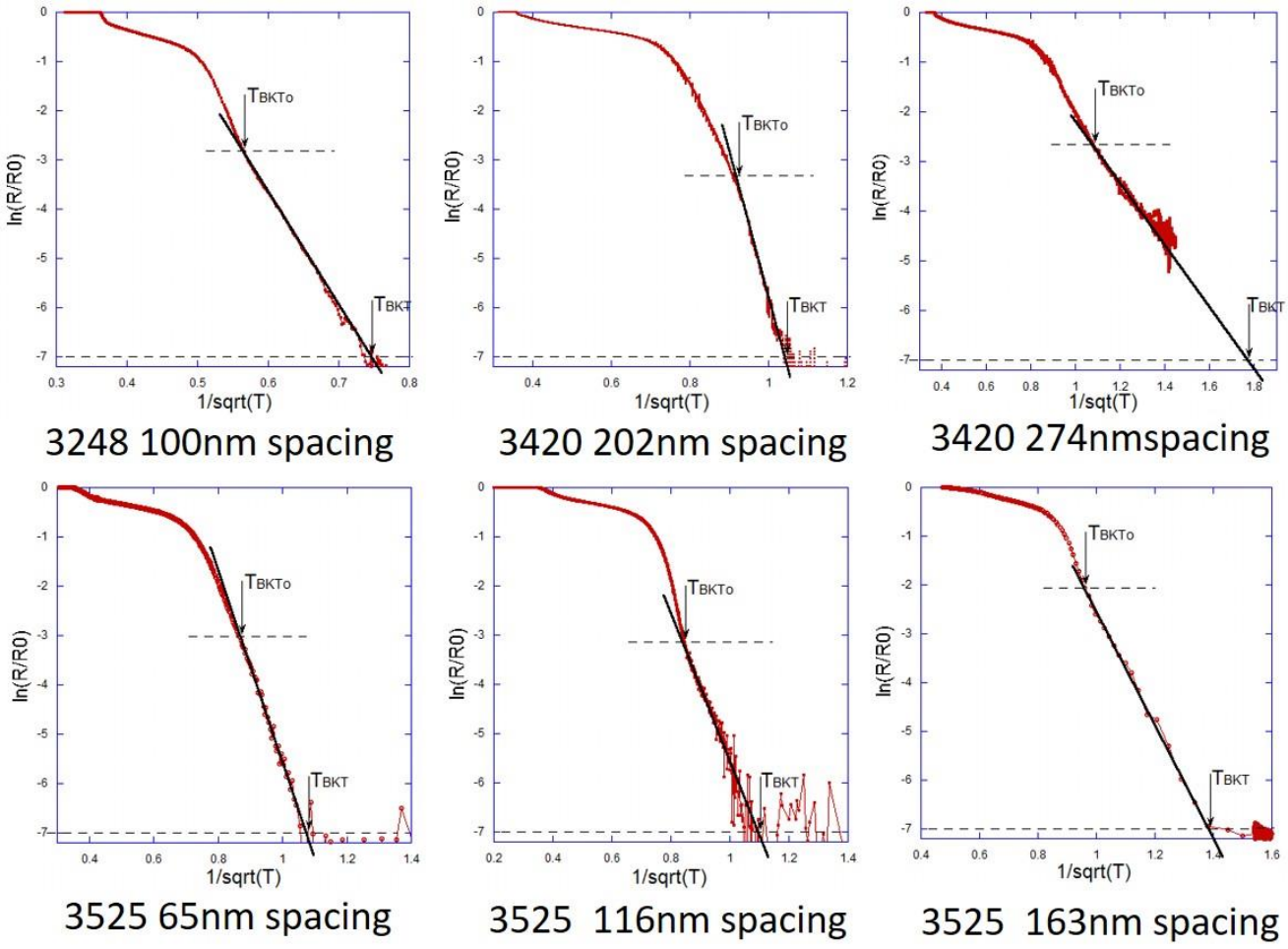


Figure 3.14 BKT fitting of four arrays. $T_{BKTo}$ is is the onset BKT temperature where data starts to deviate from the linear fitting as temperature is increased, $T_{BKT}$ is the crossing point of linear fitting line and Y= -7, these two temperatures are also summarized in table 3.4)

binding mechanism. BKT temperatures obtained from fitting are very close to Tc directly read from R-T data, and the beginning temperature of BKT, $T_{BKTo}$, are also close to $T_{C0}$. This suggests it is a good way to estimate BKT temperature by extrapolating the linearity of low temperature R-T curve crosses zero-resistance axis.

## 3.3 V-I and dV/dI-I Results

### 3.3.1 Shapiro steps, V-I and dV/dI-I results

To show that there is true Josephson effect in island arrays, Shapiro steps measurements are performed on a few arrays, and results of two arrays that show obvious voltage steps are presented in figure 3.15. The RF frequency used for both arrays is 1GHz, voltage step of the 250nm array is 162.5uV. Using the formula for Shapiro steps:

$$\Delta V = n\frac{h\omega}{4\pi e} \qquad (3\text{-}15)$$

Number of junctions in series is 80 which matches the number of rows of Josephson Junction in this 250nm array: pitch size is 1.25um, array size is 100um by 100um yields 80 rows of junctions. The array fabricated on film 3525 is of pitch size 1.28um, 30um by 30um, the total number of junctions in series is about 24. It is hard to directly read the voltage step size from I-V data of this array, so a fitting is performed (see below) and the extracted value of voltage step is 48.33 uV. Plug this number into formula (3-15), calculated value of n is 23.7 which perfectly agrees with the expect value of 23. The importance Shapiro steps is, firstly it is arguably confirmed that the array is indeed an array of Josephson junction and it exhibits AC Josephson Effect; secondly, phase stiffness exists up to 20uA in the array of 3446 which indicates the strength of phase stiffness is very strong and tolerant to bias current. The figure 3.16 explains how voltage step size is extracted.

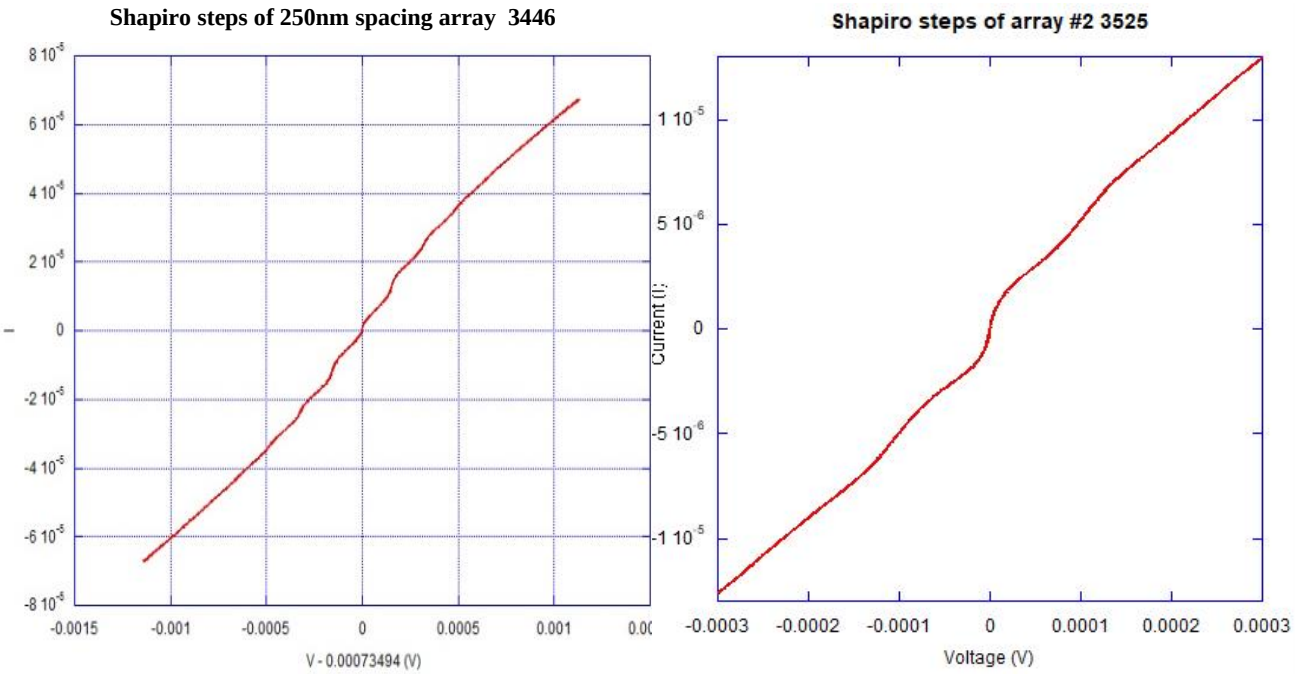


Figure 3.15 Shapiro steps of two arrays. The left one is a 250 nm spacing array fabricated on film 3446, the right side one is the 116 nm spacing array fabricated on film 3525.

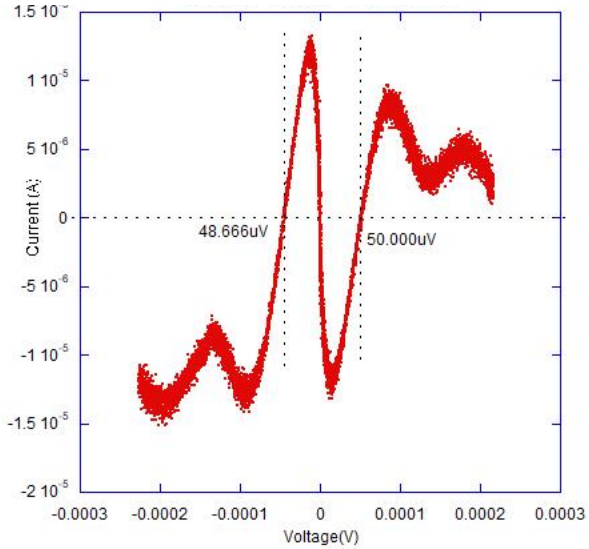


Figure 3.16 Linear fitting to extract step size value of the 116nm array fabricated on film 3525. The wavy red curve is the measured current value subtracted by a fitted value obtained by the linear I-V relation at high current. Simply read the voltage value of this curve at zero-current, one can get the voltage step size. From this one, the first voltage plateau is at positive 50uV and negative 48.666uV, average over them, voltage step value of 48.33uV is obtained. This way is much more reliable and practical than directly reading from raw I-V data.

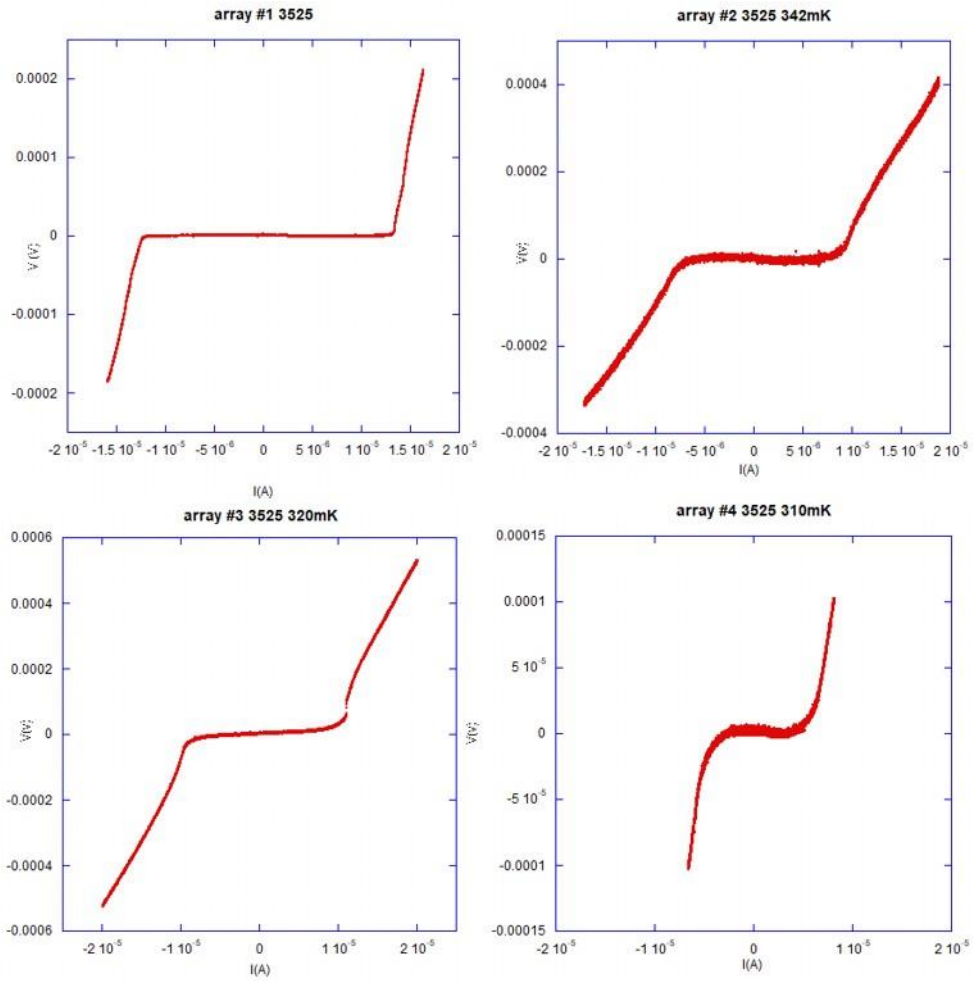


Figure 3.17 V-I results of four arrays on film 3525. From top left to lower right are 65nm spacing array, 116nm spacing array, 126nm spacing array, 163nm spacing array. Temperatures at which these measurements were taken are indicated in the title. Temperature of 65nm spacing one is missing but should be somewhere between 300mK and 340mK.

V-I results of arrays fabricated on film 3525 are presented in figure 3.17. Among these four arrays, not surprisingly the smallest spacing array has largest critical current which is 12.665uA. Critical current per junction is 0.53uA and line critical current density is 0.422A/m. Since the film thickness is 60nm, the area critical current is 703A/cm$^2$, here we assumed current is uniformly distributed in the junction cross section area. Now let us look at the $I_CR_N$ product. $I_CR_N$ per junction is 30Ω/□×0.53uA/junction=15.9μV. The superconducting gap of niobium at zero temperature is 1525μeV. The $I_CR_N$ product is much lower than expected values based on conventional Josephson junction . The very small $I_CR_N$ product of Josephson junction made on $Bi_2Se_3$ has been reported[88]. The quality of array measured in this thesis study is comparable to arrays in reference [8]. In

reference, the $I_CR_N$ product of a junction of width 1um (same width of one junction in arrays in this thesis) is 30.6uV at 12mK and has about the same normal resistance which is 35Ω ( the 65nm spacing array has 30Ω) so the difference of $I_CR_N$ of the reference and the 56nm spacing array is from the doubled critical current. According to study on Josephson junction made on $Bi_2Te_3$[89] which is similar to $Bi_2Se_3$ (transport property and crystal structure), critical current tends to increase as temperature lowers and then saturates at very low temperature region see figure 3.18. for reference. From figure 3.18, it can be estimated that ratio of $I_C$ around 300mK to $I_C$ at 12mK is about 2. Therefore, we can conjecture that, if measured at 12mK, $I_C$ of the 65nm spacing array is expected to have doubled $I_C$ as well as a doubled $I_CR_N$ product, 31.8uV. This number can be used to compare to the $I_CR_N$ product of the nanodot-island arrays, this will be discussed in chapter 4.

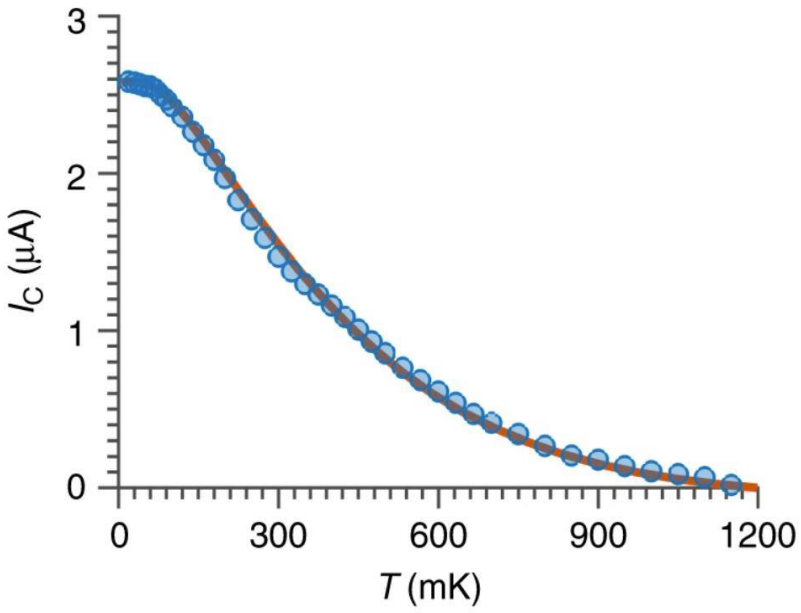


Figure 3.18 Temperature dependent critical current of a Josephson junction on $Bi_2Te_3$ borrowed from reference[9], blue circles are experimental data, solid line is theoretical fitting. At 330mK, $I_C$ is 1.3μA, at 30mK, $I_C$ is about 2.6μA.

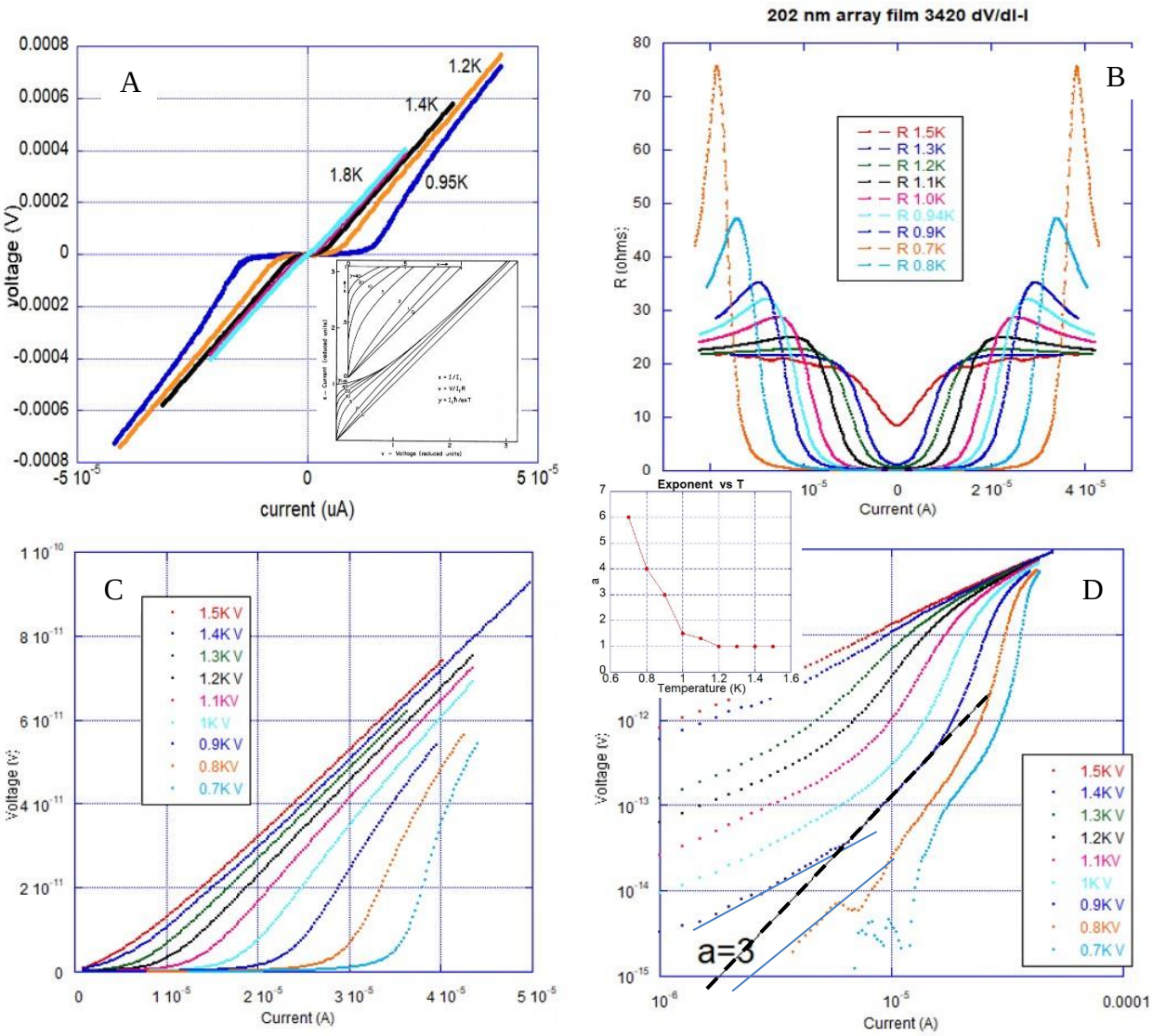


Figure 3.19 V-I characteristics of 202nm spacing array of film 3420. (A) Voltage vs DC current bias taken at different temperatures. (B) Differential resistance vs DC bias current taken at different temperatures. (C) V-I curves integrated from differential resistance results, noise level is decreased and more suitable for BKT power law investigation. (D) Integrated IV data plotted in log-log scale. The $V \propto I^3$ one is indicated by black dot-dash line. Inset is the exponent of V-I curves fitted to $V \propto I^a$ for the measured range of temperature.

V-I results of 202 nm spacing array of film 3420 are shown in figure 3.19 along with differential resistance results. There is excess current starting from temperature below 1.2K as can be seen on panel (A) and from the panel B where differential resistance touches zero at 1.2K and flats out at lower temperature. Base temperature of the PPMS is not low enough to have a V-I

curve without any Ohmic current. Thermal noise rounding effect is very pronouncing in V-I and dR-I curves. To estimate thermal rounding noise level by theory of Ambegaokar and Halperin[90], dimensionless parameter $\gamma \equiv \hbar I/ek_BT$ is calculated. At 0.7K which is the lowest temperature the PPMS can maintain, using value of excess current of 32.5uA, $\gamma$=2095. This number compared to theoretically produced number (see inset in V-I panel (A)) is too large that it is hard to believe the resistance at low temperature is solely due to thermal noise rounding effect. Another source of resistance at low temperature is the free vortices which has been explained by BKT theory. According to BKT theory, in 2D superconducting system, free vortices can cause resistance at finite temperature with finite current. At finite temperature, some vortex-antivortex pairs can be broken by thermal fluctuations to form free vortices which will cause resistance as current flows cross vortices. To investigate BKT transition in the array system, differential resistance (dR) is taken intending to obtain high signal to noise ratio data, panel (B) is the dR data taken at a range of temperature. As temperature is lowered from 1.5K, the lowest point of dR gradually approaches zero value and finally touches it at temperature about 1.0K, this agrees with the R-T measurement where lowest resistance is reached at about 0.9K. When temperature is lowered more, dR curve opens a flat region at dR=0 and the range of this region spreads wider as temperature lowers more. Panel (C) is a collection of V-I curves integrated from dR data of panel(B). To fit V-I results to power law predicted by BKT theory, current and voltage numbers are plotted in log-log scale in panel (D), exponent of 3 at 0.9K is indicated by the black line. The inset plots all exponents extracted for V-I curves. The temperature dependent exponent shows a continuous change from 6 to 1 as temperature increases from 0.7K to 1.2K then stays at 1, since above 1.2K all vortices are free and there are no other nonlinear resistive response.

Although a(T)=3 was observed, it is debating whether a clean BKT transition was experienced by the array since an abrupt jump from 3 to 1 was not observed. There are two reasons for absence of the abrupt jump. Firstly, superconductivity in the JJAs is not strict 2D. Since there are bulk carriers in $Bi_2Se_3$, with the bulk part being conductive, superconductivity from top surface layer can extend to bottom surface thorough the bulk, resulting a 3D superconducting system. This can be experimentally investigated by measuring V-I characteristics of arrays with the exact same structure but on films of different thickness. If bulk conductivity does affect V-I characteristics, a crossover transition should be overserved when thickness is lowered to some critical value where top and bottom surfaces directly interact without bulk assistance. The second possibility is the

finite-size-induced free vortices at temperature lower than BKT transition temperature. This finite-size effect has been studied by Herbert *et al*[91], the probability of finding a free vortex is given by the following formula in their paper:

$$P_f \sim e^{-F(T)/k_B T} = (\frac{L}{a_0})^{2-2T_{BKT}/T} \qquad (3\text{-}16)$$

*F(T)* is free energy of a vortex, *L* is the array size, $a_0$ is pitch size or lattice constant if taking the array as a 2D lattice, $T_{BKT}$ is the BKT transition temperature at which a(T)=3. When $T<T_{BKT}$, for an infinite array, $P_f$ is zero as expected from the original theory. For an array of finite *L* and $a_0$, there is always a finite probability of finding a free vortex. At sufficiently low current below $T_{BKT}$, current induced free vortices will leave an Ohmic tale in V-I characteristic curve, as can be seen in panel D of figure 3.19, although those tales do not exhibit exactly exponent of 1, V-I curves clearly show a trend of bending towards a(T)=1.

## 3.4 Magnetoresistance Results

In this section I will focus on magnetoresistance results of arrays fabricated on film 3525, a 60QL $Bi_2Se_3$ film. In the following text, array #1 has spacing of 65nm, #2 is 116nm, #3 is 126 nm, and #4 is 163nm. Their MR results are displayed in figure 3.21A and B.

In a magnetic field, vortices are introduced into arrays and cause resistance. An artificial Josephson junction arrays can provide uniform lattice to study how magnetic field induced vortices are pinned and migrating in the system. Results of magnetoresistance of four arrays are displayed below, spacing and temperature are labeled in the title. Magnetic field has been converted to number of fluxes per unit cell. Under integer number of fluxes, magnetoresistance (MR) dips are observed as expected except for when number of fluxes is 2, this irregular behavior will be discussed latter. Compare array #1 and #4, at low temperature region where four arrays are superconducting and have zero resistance, smaller spacing arrays can sustain more magnetic fluxes threading indicating existence of higher critical current. Above certain temperature, MR starts to show up at small frustration ($f<1$, *f* is number of fluxes). For $f<1$, vortex pinning in MR can be analyzed using the vortex pinning study done by Rzchowski, M.S, *et. al* [92]. Dips at *f=1/2*, *f=1/3*, *f=2/3* can be explained by the overlapping of the magnetic flux vortices with the underlying Josephson junction lattice. At low temperature region where thermal fluctuation energy is less than pinning strength, vortices are pinned to Josephson junction lattice sites. When thermal fluctuation

is stronger than pinning strength of vortices, vortices are mobile, and resistance appears (MR dips at small $f$ with finite resistance at higher temperature). The linear behavior of MR at vicinity of *f=1, f=1/2* which is the indication of Bardeen-Stephen[93] flux flow behavior has also been observed. We will not discuss too much in details of MR data form #3 and #4 arrays since various bias currents were used which make data sets less useful for comparing the effect of bias current and magnetic fluxes.

The MR dip at *f=2* is missing for all arrays. This could be due to inhomogeneity of islands which causes current not distribute uniformly. But it is still not understood why the 2nd dip is universally missing for all arrays. Since the origin of dips in MR is the vortex pinning effect, missing of 2nd dips means when there are two quantum fluxes threading the array lattice unit cell, there is no ground state which is energetically favored. This can be explained if there are multiple vortex-pinning sites and they do not have the same pinning potential. Simulation studies of square lattice JJAs have shown there are two types of vortex sites, Josephson junction sites (site A) and the sites that are equidistant from four nearest islands (sites B) , the latter ones have lower pinning potential[94] ( energetically favored). When *f=1,* vortices of fluxes are pinned at sites B. When *f=2,* sites A are not fully filled so vortices are still mobile, resulting a missing dip. When *f=3,* both sites A and B are filled with one vortex on each site, so MR shows a dip, see figure 3.20 for illustrative drawings.

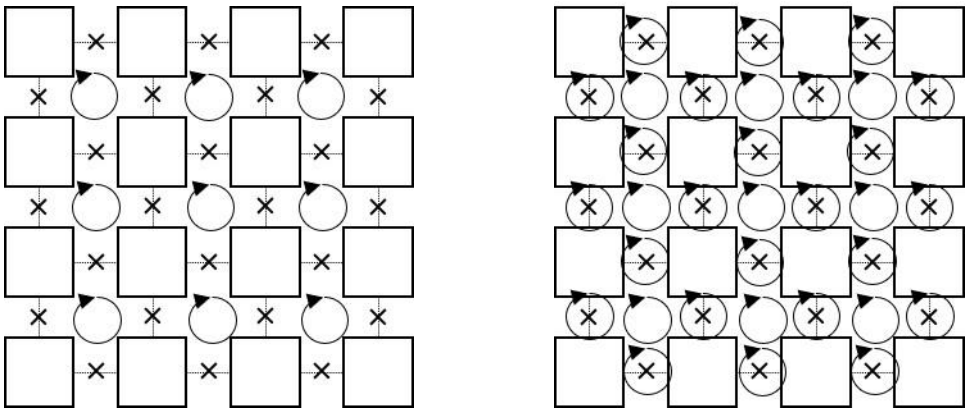

Figure 3.20 *f=1* and *f=3* configurations of vortices. Big square are niobium islands, Josephson junctions are indicated by crosses, dashed lines are guiding lines of Junction lattice.

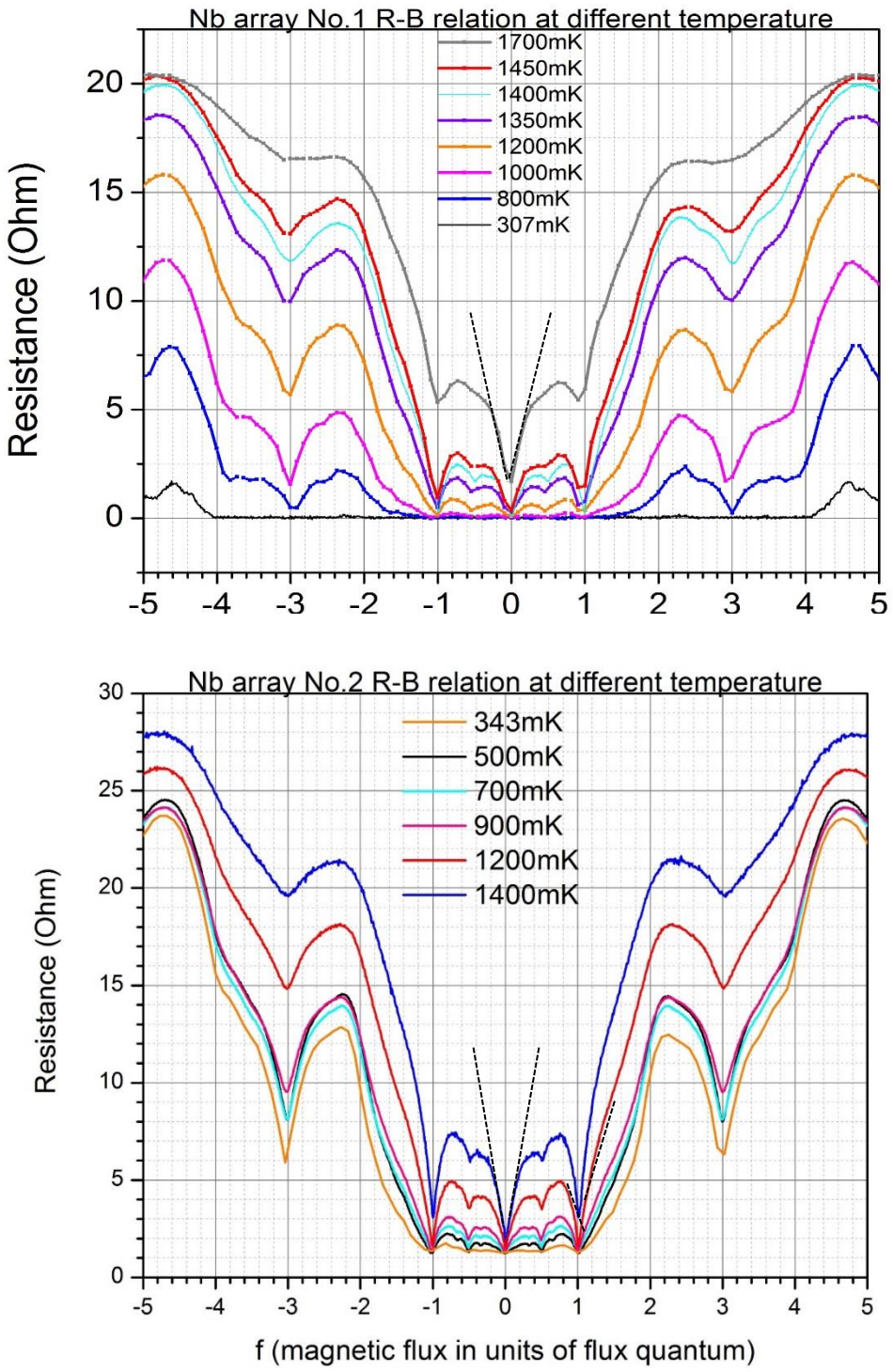


Figure 3.21 A. MR of #1 and #2 arrays. The upper right one is a zoom-in view of smaller of MR of #1 array at smaller field region. Linear Bardeen-Stephen MR is indicated by black dashed line. As temperature increases, dips at 1/3 and 2/3 disappear before the1/2 dip vanishes. At $f$ near 2, instead of a dip, MR reaches a peak.

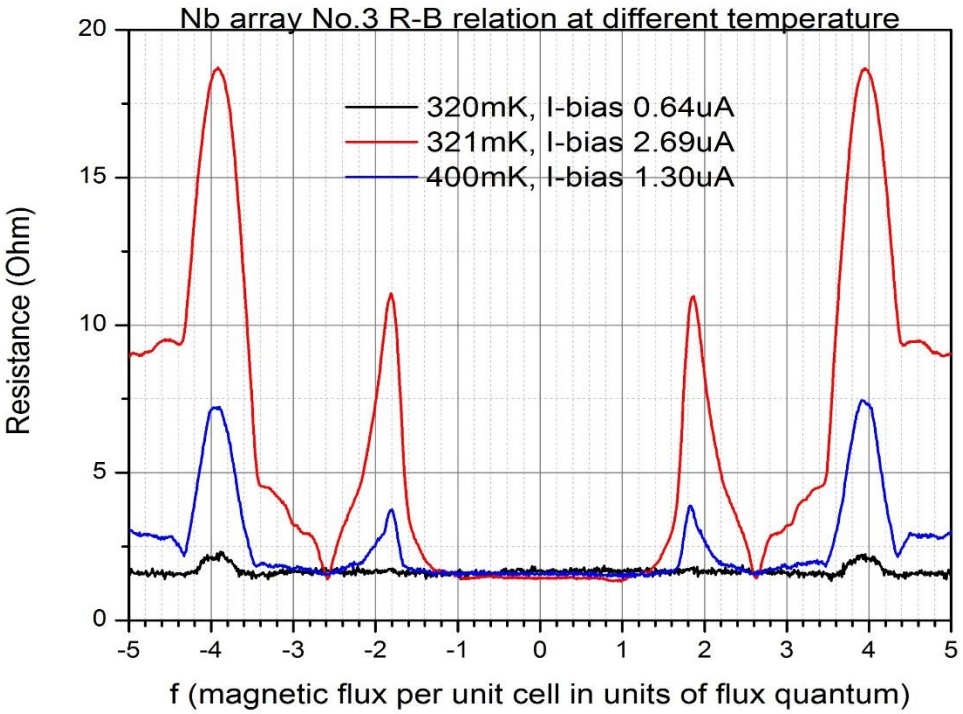


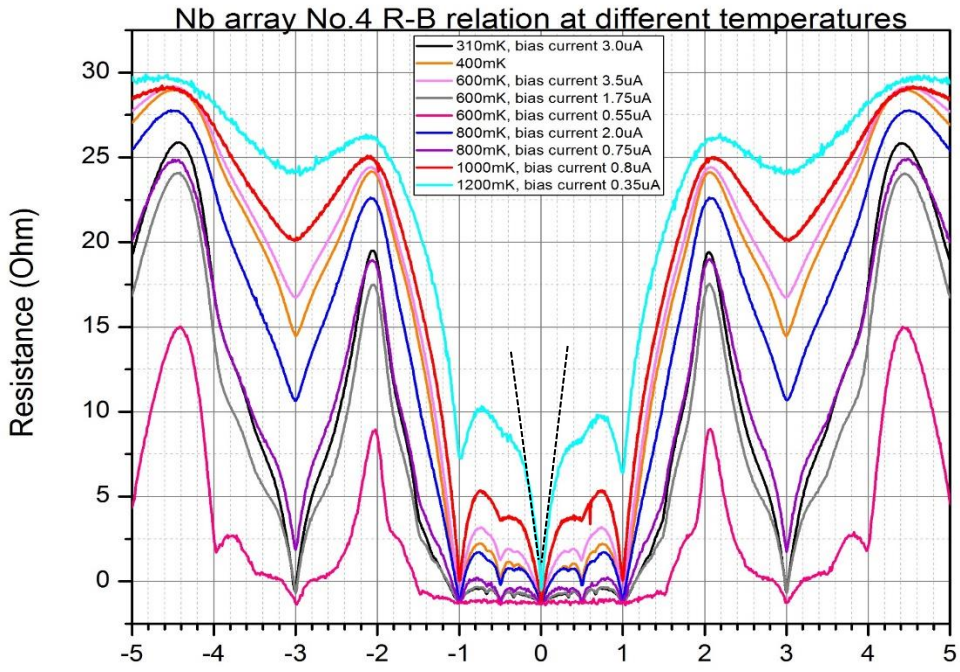


Figure 3.21 B. MR of #3 and #4 arrays. Temperatures re not high enough for #3 to reveal its low field MR. Again, black dashed lines indicate Bardeen-Stephen like MR and 2nd dips are missing.

## 3.5 Conclusion

We have fabricated and tested square JJAs made of niobium islands on $Bi_2Se_3$ with various spacings and pitch sizes. It is found that ab-plane conductance is higher than it of c-plane of $Bi_2Se_3$, therefore surface morphology has important effect on contact conductance between superconducting islands and $Bi_2Se_3$. Bumper surface may assist proximity effect because it provides larger ab-plane contact area. BKT transitions have been observed both by R-T and V-I characteristics, finite size effect and possible bulk superconductivity may result a continuously varying power exponent of V-I data. Anomalously missing $f=2$ dips have been observed, its possible origin was also discussed.

# CHAPTER 4: PROXIMITY INDUCED SUPERCONDUCTIVITY IN NIOBIUM-$BI_XSB_{(2-X)}TE_3$ ARRAYS

## 4.1 Introduction

One of the most exciting recent developments in condensed matter physics has been the proposal that the coherence of quantum computing can be enhanced by using topologically protected qubits. While there are a number of ways to do this that have been discussed, one of the simplest makes use of topological superconductors (TS) to host MZMs[95]. These are fractionalized electronic states that arise in the cores of vortices threading a TS. One dimension in the electronic state space fractionalizes into two MZMs. In a TS island, the charge parity of a pair of MZMs is changed by tunneling an electron into the pair, and the TS island goes from having an even number of electrons fully paired up into a bosonic condensate to having one more electron. Since the MZM exists at the chemical potential (zero energy), the even and odd electron configurations are degenerate. In a conventional superconductor, adding an electron to the system costs the gap energy.

The quantum degree of freedom that is used in a topological qubit is the charge parity of pairs of MZM. Since the MZM does not exhibit Fermi or Bose statistics, braiding or exchanging two MZMs in a system with more than two MZMs introduces complicated parity entanglement within the MZM subspace. The parity quantum number is quenched if free electrons are present in the sample such as in a gapless superconductor. Thus, it is important to ensure that TSs that are used to host MZMs are fully gapped.

A way to obtain a fully gapped TS capable of supporting MZMs was proposed by Fu and Kane in 2008. Their theoretical calculations showed that a TS would result if the superconductivity was introduced into spin-momentum locked topological surface states by a proximity coupled s-wave superconductor. This has been studied by many groups, including our own. In an experiment collaborating with Prof Tai-Chang Chiang's group we prepared thin samples of the n-type doped TI $Bi_2Se_3$ on superconducting niobium substrates. Using ARPES we measured the density of states on the surface opposite the substrate and observed a gap opening in the density of states as the temperature was lowered below the niobium critical temperature. The gap was not complete, however, and it was rapidly attenuated in as layers of $Bi_2Se_3$ were added to the samples.

Apparently, a sample with electrons deeper than the surface state will not be fully gapped. Furthermore, TI samples must be thick enough that the surface states on opposite sides do not quantum mechanically hybridize, so it seems that proximity coupled n-type $Bi_2Se_3$ will not provide MZMs with long parity lifetime.

Another problem with using a material having bulk carriers is that TS with quasiparticles emerges on the back side as we found in the ARPES experiment described above. This means that two MZMs on opposite sides of the film would be linked. If they become hybridized, the MZM will disappear. If they are more remote, they may exist as separate fractionalized excitations, but changes to the parity of one will almost certainly be paired with the one on the other side of the sample. Two MZMs on opposite sides of a sample could not be used as separate parts of a topological qubit.

What is needed for topological qubits is a TS consisting of only one side of a truly insulating TI. This is a single electronic layer, and it can be obtained by growing such a material and then introducing superconductivity via the proximity effect. In order to be useful, the TS should control the vortex electrodynamics. In particular, the proximity effect inducing superconductor should not control the vortex electrodynamics. This can be accomplished using arrays of superconducting islands deposited in good contact with the bulk-insulating TI. Moreover, if we want the topological superconductivity to be not influenced by the artificial spatial structure of an island array, we should have the island size and spacing be small compared to all of the important length scales that are operative. The material itself has a length scale given by the mean free path. If the spacing can be less than this, the connection of the superconductivity introduced by each island would couple to its nearest neighbor ballistically. In our experiments reported in this chapter, we are close to this case. Two other length scales are introduced by the emergent superconductivity itself. One is the coherence length which is related to the gap that develops in the density of states. The larger the gap the smaller is the coherence length, so this condition will always be satisfied for small nanodot-island arrays as long as superconductivity is induced. Likewise, the superconducting penetration depth will be large. It is only determined by the normal state electron density which is very small in these topological layers.

In this chapter, firstly I will show the bulk-insulating TI has been achieved by engineering compositions of $Bi_xSb_{(2-x)}Te_3$ films. With assistance of an ARPES study, we know that the $Bi_{0.7}Sb_{1.3}Te_3$ film used in the array study has an insulating bulk state, and the superconductivity is only induced on top surface 2D topological state. Then R-T, V-I, and dV/dI-I results of nanodot-island arrays made on the $Bi_{0.7}Sb_{1.3}Te_3$ film are presented. As a comparison, data taken on nanodot-island arrays made on a $Bi_2Se_3$ film which has bulk carriers will also be analyzed to highlight the difference in the proximity induced superconductivity. Temperature dependent transitions and Josephson coupling strength of nanodot-island arrays are discussed.

## 4.2 TSC only in one surface state of $Bi_xSb_{(2-x)}Te_3$ films

### 4.2.1 Bulk-insulating $Bi_xSb_{(2-x)}Te_3$ films

MBE grown $Bi_2Se_3$ are always n-type doped, although proximity-induced superconductivity has been successfully realized on $Bi_2Se_3$ based devices, such as described in chapter 3, it is very hard to distinguish and separate out surface and bulk superconductivity. Indeed, our ARPES base study of the Proximity Effect in $Bi_2Se_3$ in reference [reference 86, by Flötotto, David, et al] showed that the gap induced on the $Bi_2Se_3$ density of states was the same for the bulk

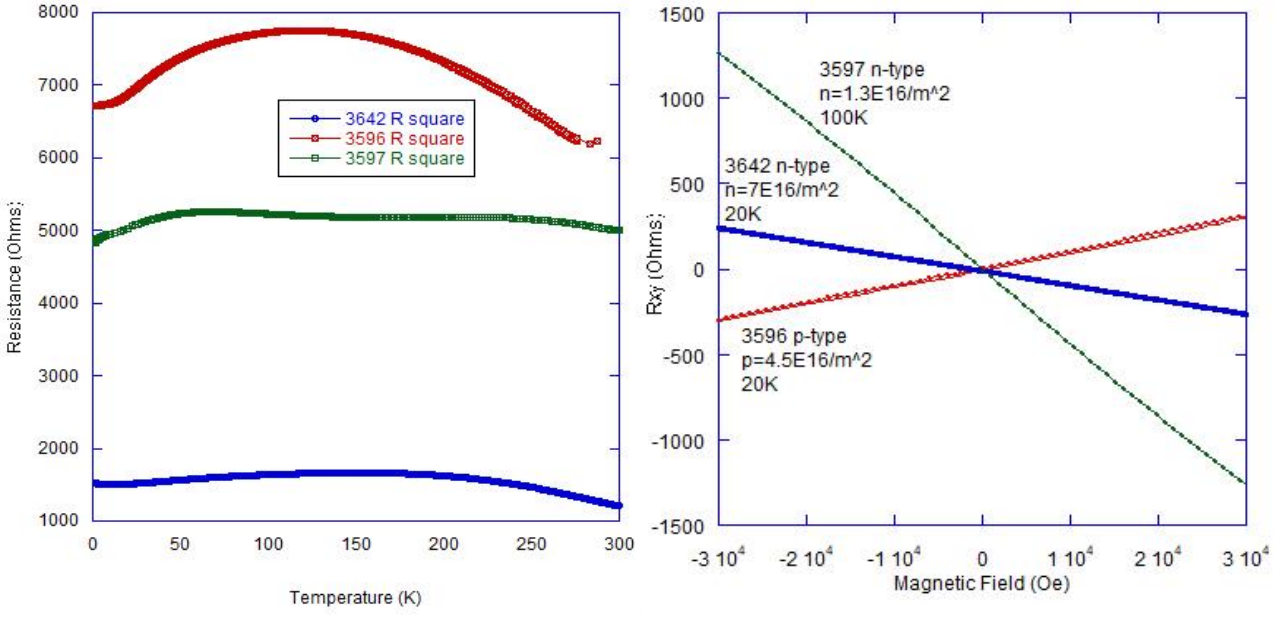


Figure 4.1 Two-dimensional resistivity and hall resistance data of three $Bi_xSb_{(2-x)}Te_3$ films with different carrier densities. Sb/Bi is about 1 for 3597 and 3596, for 3642 is 1.857 according to supplied flux ratio.

and surface states. See figure 4.3**C**, sub panel (c) which shows a gap opening in the bulk and surface states of a 4QL thick film of $Bi_2Se_3$ on a Nb substrate.

Surface and bulk proximity effect mixing causes difficulties for the investigation of Majorana physics in hybrid systems of TIs and s-wave superconductors as discussed above. Thus, TIs with intrinsic insulating bulk states are of urgent need in such experiments.

As previously mentioned in chapter 1, carrier type and carrier density of $Bi_xSb_{(2-x)}Te_3$ can be engineered by changing *x*. During MBE growth, by carefully controlling material flux ratio of Sb/Bi, both n-type and p-type films can be grown, see figure 4.1. for Hall resistance measurements of three films. Films 3596 and 3597 have the same intended Sb/Bi ratio but actually have different carrier types. Since the density of states is very small between the bulk band edges of $Bi_xSb_{(2-x)}Te_3$, small variations in composition can change carrier type and concentration. The fact that similar composition gives different types of carriers may indicate the composition is very close to the crossing point where chemical potential is near to the Dirac point.

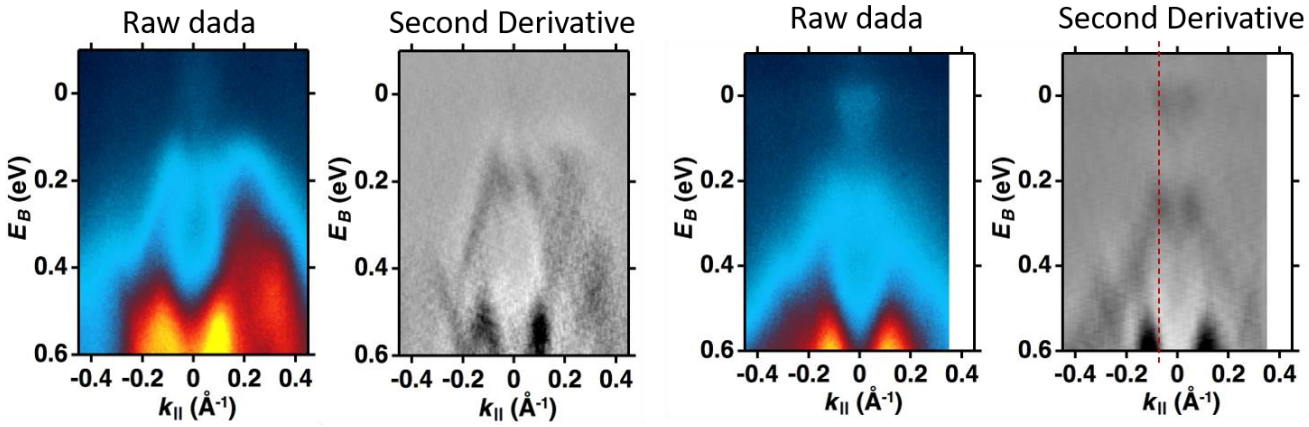


Sample 3596, 10Ql, carrier density is 4.5E+16/m$^2$, p-type from Hall measurement, Fermi vector is 0.053/Å based on carrier density. The Dirac point is hard to identify but should be very close to the Fermi energy.

Sample 3612, 14Ql, carrier density is 9.7E+16/m$^2$, n-type, no conduction band carriers according to ARPES. From ARPES, the Fermi vector is about 0.07/Å, smaller than the Fermi vector estimated from Hall effect which is 0.078/Å.

Figure 4.2 ARPES result of film 3596 and 3612. No conduction bands for both films. The carrier density of film 3642 measured by Hall effect lies between 3596 and 3612, it should not have any bulk carriers.

To further explore the Fermi surface of film 3642, we can use Hall and ARPES measurement on film 3596 and 3612. ARPES of film 3596 and 3612 are shown in figure 4.2. They were taken in Professor Tai-Chang Chiang's lab by his student, Joseph Hlevyack. Film 3596 is p-type and the Fermi circle lies below the Dirac point. Film 3612 is n-type and the Fermi circle lies

above the Dirac point. From ARPES, the Fermi vector of film 3596, although very hard to quantify, is very small, and the Fermi vector of film 3612 is about 0.07/Å. From Hall effect, we can infer their Fermi vectors are : $k_F^{3596} = 0.053/\text{Å}$, $k_F^{3612} = 0.078/\text{Å}$. Although ARPES was not performed on the film 3642, the value of $k_F^{3642}$ can be determined from carrier concentration obtained from Hall measurement using the relation :$k_F = \sqrt{2\pi n}$, $n$ is the total (sum of top and bottom surfaces) 2D carrier density of the film. Since $n_{2D}^{3642} = 7E + 16/m^2$, we obtain $k_F^{3642} = 0.066/\text{Å}$, which is between values for film 3596 and film 3612. Thus, we conclude that there should be no bulk carriers for film 3642.

### 4.2.2 TSC confined in top surface state

To fabricate topological qubits, TS of only one side proximity-coupled surface is required. In our recent collaboration work[96] with Prof Tai-Chang Chiang's group, it is found that proximity induced superconducting gap is massively suppressed in bulk insulating $Bi_xSb_{(2-x)}Te_3$ films compared to the gap opened in $Bi_2Se_3$ introduced by the same manner. In this study, the measured spectrum is of the density of states of the surface opposite to the surface directly touches the superconductor layer. In the proximity-coupled $Bi_xSb_{(2-x)}Te_3$ film, superconductivity attenuates rapidly, and the gap is complete closed when the distance between superconductor layer and the surface probed by ARPES reaches 4QL.

To probe the density of states of the surface opposite to the superconductor layer, a flip-chip technique was developed. Figure 4.3**A** explains how $Bi_xSb_{(2-x)}Te_3$/Nb bilayer is prepared using the flip-chip technique. Before introducing into the vacuum chamber, a cleave pin is glued onto a piece of sample consisting of the substrate, $Bi_xSb_{(2-x)}Te_3$ thin film and niobium layer at the bottom, this whole piece is fixed on a copper plate. Inside the vacuum chamber, the cleave pin is knocked off. Because the van der Waals bonding between substrate and $Bi_xSb_{(2-x)}Te_3$ thin film is the weakest bond in this structure, substrate will be knocked off with the cleave pin together, exposing the opposite surface of film. This enables ARPES measurement on a vacuum clean level surface and provide the ability to probe the proximity effect from the opposite direction.

To determine how proximity effect attenuates with thickness of the film, 2-10QL films have been used. In figure 4.3**B**, symmetrized density of states of $Bi_xSb_{(2-x)}Te_3$/Nb and $Bi_2Se_3$/Nb bilayers are summarized. The gap size of 2QL $Bi_xSb_{(2-x)}Te_3$/Nb is significantly smaller than the

gap of a 4QL $Bi_2Se_3$/Nb. Gap still presents for $Bi_2Se_3$ up to 10QL while for $Bi_xSb_{(2-x)}Te_3$ gap vanishes for 2QL thickness.

Compare spectra of density of states of Nb/$Bi_2Se_3$ and $Bi_xSb_{(2-x)}Te_3$/Nb bilayers, see figure 4.3**C**, proximity induced superconductivity is completely suppressed for the latter one. In $Bi_2Se_3$/Nb bilayer system, a clear gap opens at the opposite surface. This is not desired as the superconductivity would connect two surface states and the MZMs that appear on both surfaces either hybridize or coupled and cannot be manipulated separately. While in the $Bi_xSb_{(2-x)}Te_3$/Nb bilayer system, a 4QL film is thick enough to suppress superconductivity and the surface separated by it remains gapless.

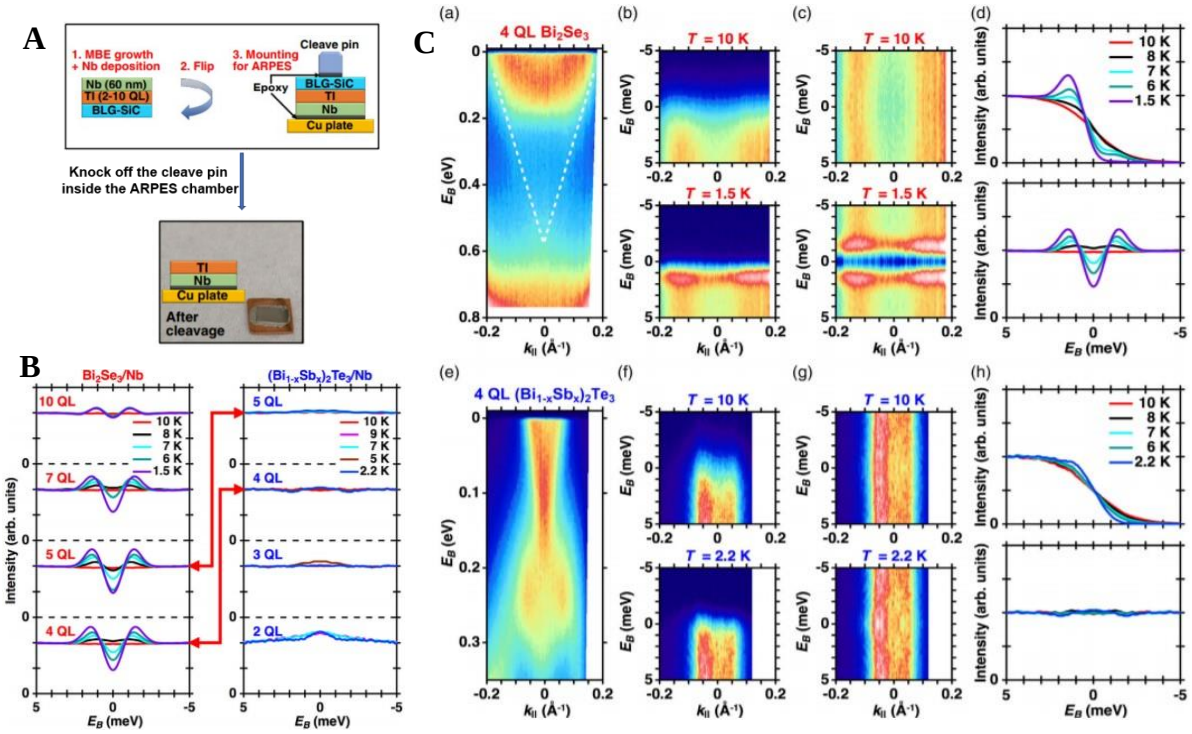


Figure 4.3 ARPES study of $Bi_xSb_{(2-x)}Te_3$/Nb bilayer. (A)illustration of how samples are prepared using the flip-chip technique. (B)Proximity effect penetrates up to10QL for $Bi_2Se_3$, 4QL for $Bi_xSb_{(2-x)}Te_3$. (C) Comparison of superconducting gap induced on the opposite surface of 4QL $Bi_2Se_3$ and $Bi_xSb_{(2-x)}Te$. Bulk-insulating $Bi_xSb_{(2-x)}Te_3$ films does not have a superconducting gap open in the surface state on the opposite side. All graphs are from the paper by Hlevyack, Joseph A., et al: "Massive Suppression of Proximity Pairing in Topological $(Bi_{1-x}Sb_x)_2Te_3$ Films on Niobium." *Physical Review Letters* 124.23 (2020): 236402.

The $Bi_xSb_{(2-x)}Te_3$ films tested in this ARPES study have similar composition ($Bi_{0.76}Sb_{1.24}Te_3$) of the film 3642 ($Bi_{0.7}Sb_{1.3}Te_3$). The fact that the gap vanishes at the other surface of tested films suggests that the proximity-induced SC in arrays fabricated on the film 3642 resides only in the electronic states of top surface. MZMs only exist on the surface that touches superconducting islands.

## 4.3 Low Temperature Resistive Transition Results

*Summary of device geometrical information and R-T results:*

Arrays on film 3642 ($Bi_{0.7}Sb_{1.3}Te_3$, BST) and film 3678 ($Bi_2Se_3$, BS) consist of nanodot niobium islands. Array pitch size varies from 200nm to 290nm. Dot size varies from 78.8nm to 100nm.

To determine contacting area size of dots, we can use AFM images of arrays taken before niobium is sputtered. The ZEP 520 E-beam resist leaves uniform exposed profile( see figure 4.4), dot-shape holes exposed on ZEP 520 should have the same area size for both top and bottom. From AFM images taken before niobium deposition, top area size of holes can be measured which can be used as the bottom area size. This area serves as the contacting area that directly connects niobium dots and film. Contacting area sizes of tested arrays have been calculated using AFM images shown in two lower panels of figure 4.5, and their sizes are summarized in table 4.1 along with pitch sizes, spacings, normal state resistances, and two-dimensional resistivity of BS and BST films.

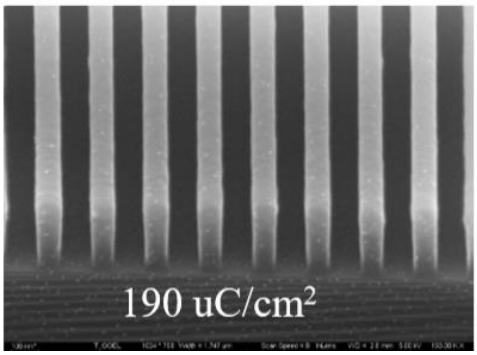


Figure 4.4 An SEM of 100nm line features showing high z-direction profile uniformity written by E-beam using ZEP-520 resist. Along z-direction, variation of line width is small, size of top and bottom openings can be considered the same. This image is taken from the website of Georgia Tech Nanotechnology Research Center.

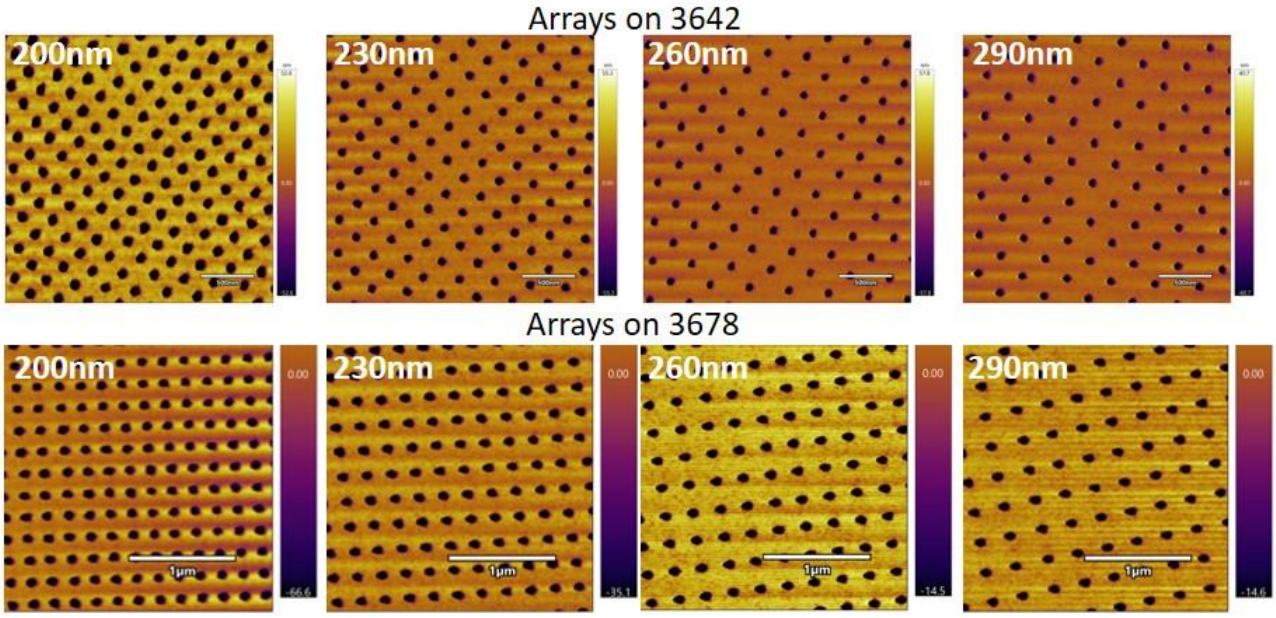


Figure 4.5 AFM images of arrays. The upper and lower panel are images of arrays before niobium deposition on BST and BS films, respectively.

| Array index | Pitch size (nm) | Spacing (nm) | Dot diameter(nm) | Normal resistance (9K) | Square Resistance (9K) |
|---|---|---|---|---|---|
| 3642 #1 | 200 | 100 | 100 | 1417 | 1505 |
| 3642 #2 | 230 | 141.5 | 88.5 | 1482 | |
| 3642 #3 | 260 | 181.2 | 78.8 | 1524 | |
| 3678 #1 | 200 | 107.8 | 92.2 | 81 | 90.3 |
| 3678 #2 | 230 | 133.9 | 96.1 | 84 | |
| 3678 #3 | 260 | 163.8 | 96.2 | 70 | |
| 3678 #4 | 290 | 201.8 | 88.2 | 74 | |

Table 4.1 Summary of array parameters, resistance, and 2D film resistivity. Notice that normal state R of array 3642#3 is slightly higher than film sheet resistance, this could be due to inhomogeneity of the film which causes its sheet resistance varies slightly at different location. All data were taken in PPMS.

Temperature dependent resistance results of all measured arrays are summarized in figure 4.6. Nanodot-island arrays on BS film show the same two-step transitions as big square arrays made on $Bi_2Se_3$ have shown, but the first step transition is rounded, and this rounding effect is

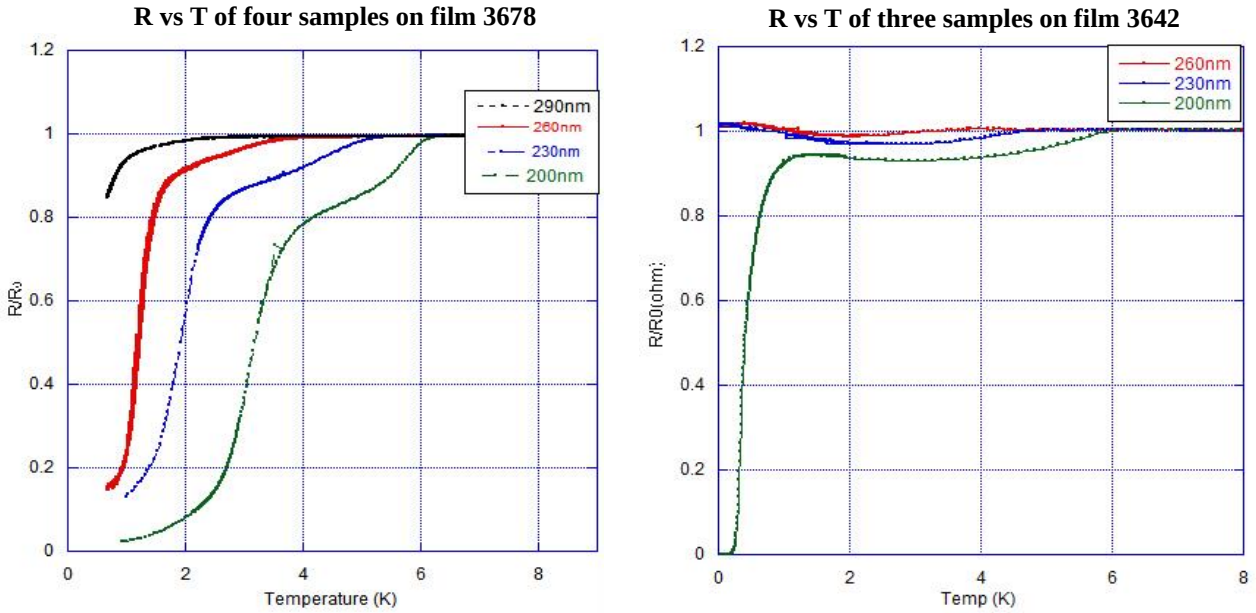


Figure 4.6 Left panel is R-T results of dot-arrays on the BS film, right one is R-T results of dot-arrays on the BST film. Resistances are normalized to arrays' normal resistance at 9K.

more pronouncing for larger spacing arrays. Despite of its long mean free path, 160nm, which is longer than the 100nm spacing of 200nm pitch array, the array does not reach a zero-resistance or a finite-resistance stage at around 0.7K. For mean free path and carrier information of two films, refer to table 4.2. Due to the small size of superconducting niobium islands, superconductivity strength is weaker than bulk niobium[97]. The weaker superconductivity may have suppressed the proximity effect at interface of islands and film. Data taken at lower temperature (50mK) of 200nm array fabricated the BS film shows supercurrent, these results will be presented in V-I results section. As pitch size increases, spacing increases, and the first transition shows a broadening trend. For array of 260nm pitch, the first resistance drop is nearly invisible. This broadening behavior is due to the weakened proximity effect between islands and film area of their

| Film Index | Thickness (QL) | Carrier type | Carrier density (/m²) | Mobility (cm²/Vs) | Square Resistance/Ohms | Mean Free Path (nm) |
|---|---|---|---|---|---|---|
| 3642 $Bi_{0.7}Sb_{1.3}Te_3$ | 60 | n-type | 7E+16 | 587 | 1505 | 25.6 |
| 3678 $Bi_2Se_3$ | 30 | n-type | 4.2E+17 | 1579 | 90.3 | 160 |

Table 4.2 Carrier density, square resistance, mobility, and mean free path of film 3642 and 3678. Carrier density and mean free path of 3642 are about 17% and 16% of 3678, respectively.

vicinity. The same behavior also appeared on nanodot-island arrays on the 3642 BST film. To understand this behavior, first we need to understand the significant role that the contact resistance plays in nanodot-island arrays devices.

### 4.3.1 Transport model of nanodot-island arrays

#### *4.3.1.1 Contact resistance*

Before discussing R-T results of array devices, firstly we need to construct a transport model for nanodot-island arrays. For nanodot-island arrays, contact resistance plays an important role as it is responsible for several anomalous features in R-T behavior as will be explained later. In chapter 3, the contact resistance is explained by a concept of transfer length. Transfer length of square-island arrays is of order of 50nm which is much smaller than dimensions of square islands, the resistance caused by contact resistance is of small portion of total resistance. For nanodot-island arrays, contact resistance is a major component of total resistance. To see how contact resistance contributes to total resistance, the following circuit model is developed. As depicted in figure 4.7, resistance of a unit cell of an array can be calculated based on the circuit model shown in the lower right-side corner of the figure. Contact resistance is represented by $R_\eta$. From this circuit model, at 9K when niobium islands are in normal state, resistance of a unit cell is :

$$R_{\square}(9K) = \frac{1}{\frac{1}{2R_\eta + R_{Nb}} + \frac{1}{R_1}} + R_2 \qquad (4\text{-}1)$$

Because array lattice is of square shape, resistance of a unit cell equals to array resistance. Use parameters listed in table 4.2.1, for the 200nm pitch array on BST and BS films, at 9K one can obtain:

$$2R_\eta + R_{Nb} = 5990\Omega \quad \text{(BST film)}$$

$$2R_\eta + R_{Nb} = 174\Omega \quad \text{(BS film)}$$

These numbers are much bigger than $R_{Nb}$, which is of the order of 1Ω. When niobium islands become superconducting, $R_{Nb}$ becomes zero. This change of resistance barely affects the total resistance of the array since it is obscured by huge contact resistance. Big contact resistance is also why normal resistance at 9K of nanodot-island arrays on BS and BST are comparable to square resistance of bare films and do not vary significantly with various array spacings.

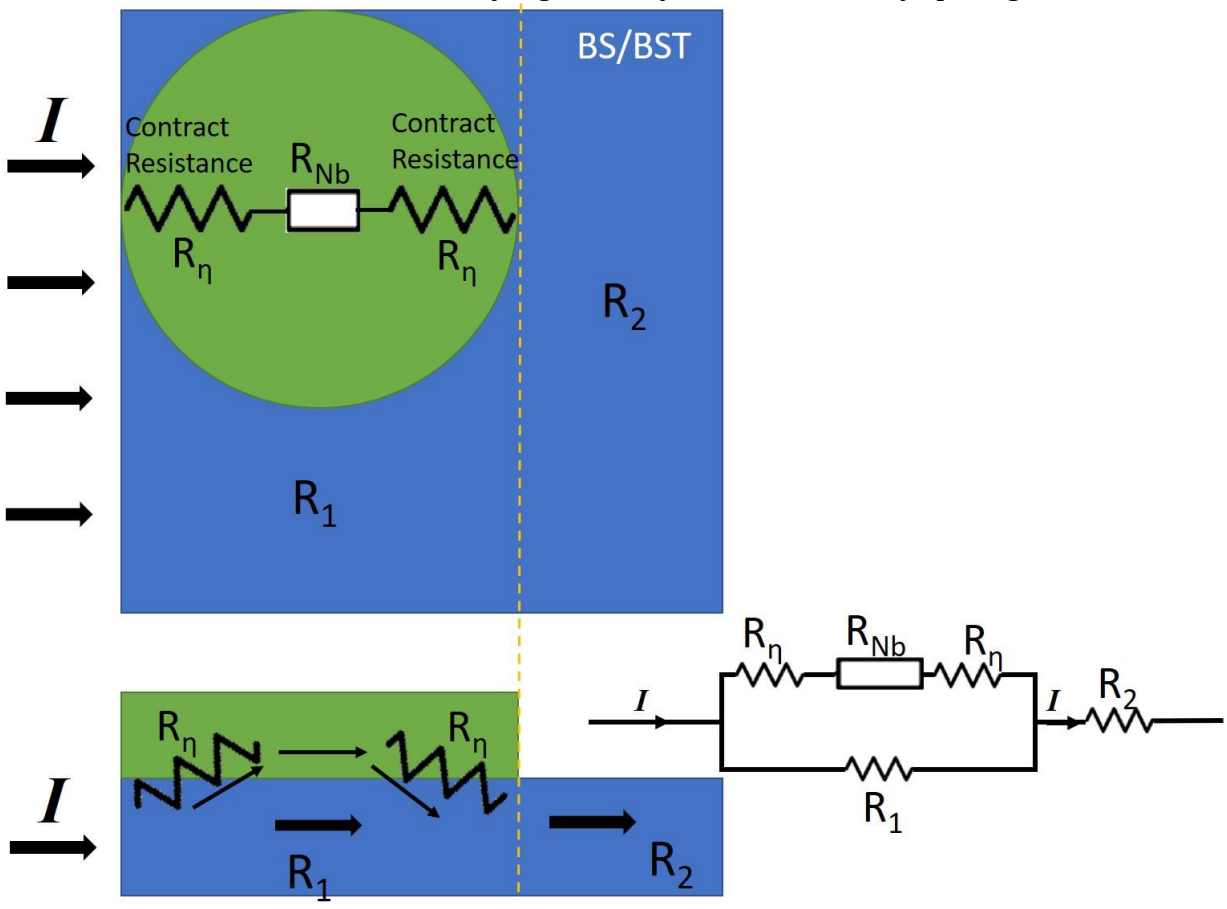


Figure 4.7 Circuit model of nanodot-island arrays. The upper blue square with a green circle is on unit cell of an array. Blue area is film, either $Bi_2Se_3$ or $Bi_xSb_{(2-x)}Te_3$, green circle is a niobium dot, black arrows are current indicators, thickness of arrows represent current density. $R_1$ is resistance of film area at left side of the yellow dashed line, it is parallel to resistance of the dot island. $R_2$ is resistance of film area at right side of the yellow line. $R_\eta$ is the contact resistance, one at each side of the island. Note that for square-island arrays, contact resistance is small and was modeled using transfer length, here transfer length is no longer a good estimate for it since dot size is short than transfer length and contact resistance is bigger than sheet resistance of films.

#### *4.3.1.2 Specific contact conductance*

We use the contact resistance obtained above to calculate the specific contact conductance, $G_C$((SI units Siemens/m$^2$), for dot-shape contacts. To calculate $G_C$, firstly we need to estimate the area ($A$) that current takes to flow in (or out) a dot. To make algebra simple, we model this area as a rectangular box of length 100nm ( this is the value of the diameter of the dot of 200nm pitch array, perpendicular to the current flow direction), width 30nm (along the direction of current, about 1/3 of the diameter of the dot). $G_C$ of 200nm pitch arrays for BS and BST films are obtained as following:

$$G_C = \frac{1}{R_\eta A} = 4.3E + 12 \text{ (S/m}^2\text{)} \quad \text{(BS film)}$$

$$G_C = \frac{1}{R_\eta A} = 1.1E + 11 \text{ (S/m}^2\text{)} \quad \text{(BST film)}$$

Here we assume resistance of a niobium dot is 10Ω. $G_C$ obtained here for the BS film is comparable to the $G_C$ of square-island arrays obtained in chapter 3, section 3.2.1. The exact value of $G_C$ may vary with the selection of the area of the current flow, what is important here is the $G_C$ of dot contact on BS is an order of magnitude bigger than $G_C$ is on BST film.

Smaller $G_C$ of contacts made on BST film may be a natural result of the 2D nature of BST surface electrons. As discussed in section 4.1, carriers that participate into electronic transport of the 3642 BST film are strictly 2D because the BST film is bulk carrier free and its top surface is completely decoupled from its bottom surface.

Transfer length can also be calculated using $\eta = 1/\sqrt{R_\square G_C}$ . We get η of 51nm for BS film, 78nm for BST film. The calculated values of η are over half of the diameter of the dot, this means we can simply take the transfer length to be half of the diameter which is 50nm. The ratio of η divided by island size, we name it as γ, is therefore 0.5 for nanodot-island arrays. This is a huge number comparing to value of γ for suqare-island arrays made on the BS discussed in chapter 3, which ranges from 0.03 to 0.04 dependeing on surface morphology. In chapter 3, supercondcutig transition of niobium islands is reflected in R-T cureves as a sharp resistance drop, while in this chapter as will be discussed in the resistive transtion section, superconducting transition of dot niobium islands is not detectable in R-T results. This can be explained by the difference of γ. A big γ means the contribution from niobium to the total normal state resistance of the array is small

and vice versa. Thus, for large square-island arrays, the change caused by nobium resistance becoming zero is obervable while for nano nanodot-islands, that change is covered by contact resistance.

#### *4.3.1.3 Contact conductance of 3D/2D contacts*

Nanodot-island contacts made on the BS film are formed between 3D electronic material (niobium) and mixture of 2D and 3D electronic material (BS film). Contacts made on the BST film are formed between 3D (niobium) and pure 2D (top surface carriers of the BST film)electronic materials. The proximity effect in the former scenario happens in a 3D/(2D+3D) system while in the latter one, it happens in a 3D/2D system. We want to quantitively analyze how proximity effect in a 3D/2D system differs from a conventional 3D/3D system. We can do this by separating out the contact conductance ($G_C$) of a 3D/2D system from the $G_C$ of a 3D/(2D+3D) system by comparing the $G_C$ difference of 3D/(2D+3D) and 3D/2D systems, that is, by comparing $G_C$ of nanodot-islands/BS and nanodot-island/BST arrays.

The $G_C$ we calculated in the last section is the effective conductance we directly got from experimental values of contact resistance. To consider of impact of 2D carriers to the contact conductance, we must construct a more accurate expression of $G_C$.

Carriers of the BS film consist of 2D and 3D carriers, the contact conductance therefore consists of two parts:

$$G_C^{BS} = G_C^{2D} + G_C^{3D} = g_{2D} \cdot n_{2D} + g_{3D} \cdot n_{3D} \quad (4\text{-}2.1)$$

Here we introduced new parameters of $g_{2D}$ and $g_{3D}$, they denote 2D and 3D specific contact resistance per carrier, respectively. $n_{2D}$ and $n_{3D}$ are carrier density (per area) of 2D and 3D carriers. For the BS film used in this thesis research, we assume that $n_{2D}$ is 1/3 of the total carrier density. Total carrier density is 4.2E+17/m$^2$, $n_{2D}$ is 1.4E+17/m$^2$, $n_{3D}$ is 2.8E+17/m$^2$. The corresponding $k_F^{2D}$=0.094/ Å. $k_F^{3D}$ should be close to but smaller than $k_F^{2D}$, we assume it is 0.09/ Å. $k_F$ will later be used to calculate transmission coefficient.

Carriers of the BST film are purely 2D, and only top half contribute to contact conductance, thus the contact conductance is simply:

$$G_C^{BST} = G_C^{2D} = \frac{1}{2} g_{2D\cdot} \cdot n_{2D}$$

$n_{2D}$ is 7E+16/$m^2$ for the BST film. We assume that $G_C^{2D}$ is proportional to its 3D counterpart

$$G_C^{2D} = \alpha G_C^{3D}, \text{ so}$$

$$G_C^{BST} = G_C^{2D} = \frac{1}{2} g_{2D\cdot} \cdot n_{2D} = \alpha G_C^{3D} \quad (4\text{-}2.2)$$

We can use $G_C$ of the BS film to get the factor of α.

Plug $G_C$ values obtained in the last section into equation (4-2.1) and (4-2.2), we get:

$$g_{2D} = 3.14E-6\ (S/m^2/carrier)$$

$$g_{3D} = 1.38E-5 (S/m^2/carrier)$$

Recall that in chapter 3, we used

$$G_C = \frac{2e^2}{h} N|T|^2 \quad (4\text{-}2.3)$$

to calculate transmission coefficient $|T|^2$, $N = (\frac{2}{\lambda_F})^2 = (\frac{k_F}{\pi})^2$ is the number of conductance channels. This formula is for contacts between 3D carrier materials, it naturally follows that:

$$G_C^{3D} = g_{3D} \cdot n_{3D} = \frac{2e^2}{h} (\frac{k_F^{3D}}{\pi})^2 |T|^2$$

Rewrite equation (3) for contacts on the BS film:

$$G_C^{BS} = g_{2D} \cdot n_{2D} + \frac{2e^2}{h} (\frac{k_F^{3D}}{\pi})^2 |T|^2 \quad (4\text{-}2.4)$$

Using $k_F^{3D} = 0.09/\text{Å}$, we get

$$|T|^2 = 0.602$$

To get the value of α, we need to assume that $|T|^2$is the same for arrays on the BS and the BST films. This assumption is justified that here we attribute difference of contacts to the contact conductance and keep the barrier strength the same.

Plug values of $|T|^2$, $g_{2D}$, $k_F^{2D}$= 0.07/ Å into

$$G_C^{BST} = G_C^{2D} = \alpha G_C^{3D} = \alpha \frac{2e^2}{h} (\frac{k_F^{2D}}{\pi})^2 |T|^2 \quad (4\text{-}2.5)$$

We get α=0.049.

We can also use

$$G_C^{BS} = g_{2D} \cdot n_{2D} + \frac{2e^2}{h} \left(\frac{k_F^{3D}}{\pi}\right)^2 |T|^2 = 2\alpha \frac{2e^2}{h} (\frac{k_F^{2D}}{\pi})^2 |T|^2 + \frac{2e^2}{h} \left(\frac{k_F^{3D}}{\pi}\right)^2 |T|^2 \quad (4\text{-}2.6)$$

To calculate α, notice the factor of 2 presents because both top and bottom surfaces of the BS film contribute to the contact conductance. This yields α=0.053, agrees with the α obtained from data of the contacts on the BST film. Average over 2 values of α, we get α=0.051.

Thus, the contact conductance formula for 3D/2D contact system is:

$$G_C = 0.051 \cdot \frac{2e^2}{h}\left(\frac{k_F^{2D}}{\pi}\right)^2 |T|^2 \quad (4\text{-}2.7)$$

Equation (4-2.7) is of great importance as it illuminates a way of quantifying the quality of a contact of 3D electronic system on 2D electronic system. The value of α may not be accurate but this demonstrated a way of obtaining $G_C^{2D}$ out of $G_C^{3D}$ .d This also allows us to evaluate proximity effect occurring at the interface of a 3D/2D system. It also points out as an experimental finding that contact to a strictly 2D system is different and more difficult than contact to a 3D material.

#### *4.3.1.4 S-INI-S junction model*

In the contact resistance part, we have demonstrated that island contacts made on the BST film exhibit high resistance. The value of contact resistance is two times of the sheet resistance of film itself. To incorporate the big contact resistance and small contact resistance of arrays on the BST film, we use an insulating layer between nanodot-islands and the BST film to model the big contact resistance, so Josephson junctions in nanodot-island arrays on the BST film are effectively SINIS junctions, see figure 4.8. The origin of insulating layer that there are no bulk carriers and conduct to a strictly 2D electronic system is more difficult than to a 3D electronic system as demonstrated in the last section. The consequence of the additional insulating layer is a superconducting gap smaller than it of niobium islands which results weaker Josephson coupling and lower critical current as will be shown in V-I results chapter.


Figure 4.8 Side view of two islands on a TI film, black layer indicates the insulating layer, the Josephson junction connecting two adjacent islands consists of an insulating layer, TI layer, and insulating layer, therefore is a SINIS junction.

### 4.3.2 Proximity affected $T_1$ and its spacing dependence

The niobium superconducting transition is hard to be reflected in R-T curves of nanodot-island arrays because the resistance change caused by superconducting transition of niobium islands is too small compare to the contact resistance. The temperature ($T_1$) of first resistance drop should not be taken as the superconducting transition temperature of niobium dots. The actual superconducting transition of niobium dots happen at higher temperature, it may be lower than bulk niobium critical temperature due to size effect. For square-island arrays discussed in chapter 3, contact resistance is small, so the temperature of first resistance drop can be taken as the transition temperature of niobium islands.

The next question is what happens at transition temperature ($T_1$) of first resistance drop if it is not the critical temperature of individual niobium island. In the following paragraphs, we will focus on R-T results of arrays on the BS film to further discuss the spacing dependence of $T_1$. R-T results of arrays on the BST film will be discussed in section 4.2.3.

We use 200nm pitch array of the BS film to explain. As shown in figure 4.9, $T_1$ indicates temperature of first observed resistance drop, at $T_2$ R-T slope becomes smaller, $T_3$ is the second transition temperature below which the inter-island proximity effect dominates. At onset temperature of niobium, resistance is expected to take a very sharp drop. However, at $T_1$ shown in figure 4.9, resistance takes a gradual rate to lower, and the lowering rate decreases with increasing spacing. This agrees with the previous judgement that $T_1$ is not the critical temperature of an intrinsic superconductor. The next candidate for $T_1$ is the proximity effect, resistance starts to decrease because of proximity effect. One explanation is that the resistance at $T_1$, proximity effect of an island senses the proximity effect of the island next to it, in other words, proximity effect of individual island meets at the middle point of two neighbored islands. Above $T_1$, proximity effect of one island is so weak that it does not cause measurable resistance decrease, while after $T_1$, it is enhanced by neighborhood islands and sets the beginning of a steep resistance drop. At $T_2$, proximity effect of each island expands further and touches the neighbored islands. Between $T_2$ and $T_3$, contact resistance is lowered. Below $T_3$,

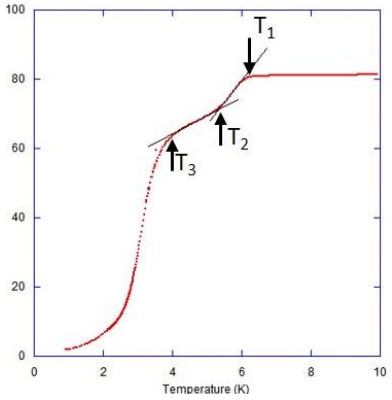

Figure 4.9 R vs T of 200nm array on the BS film.

since the radius of proximity effect covers more than one unit cell, multiple islands work together to lower the resistance between islands which gives resistance a much steeper slope. It is also helpful to understand resistive behavior below $T_3$ by imagining that as temperature lowers, effective length of weak links made of normal material between two islands is decreased. As temperature is lowered further, eventually Josephson effect takes place.

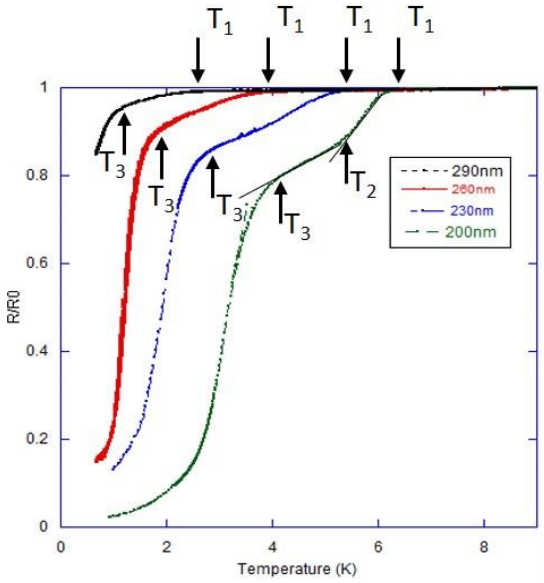

Figure 4.10 R vs T of four samples on BS film.

It is also noticed that as spacing increases, temperature interval between $T_1$ and $T_2$ decreases, and for 290nm spacing $T_2$ is hard to identify and it almost looks like a one-step resistive transition, see figure 4.10. This can be viewed as a transition from ballistic weak links to diffusive ones. The BS film has a mean free path of 160nm. This number is larger than spacings of 200nm and 230nm arrays which are 107.8nm and 133.9 nm, respectively, comparable to spacing of 260nm array which is 163.8nm , and smaller than spacing of 290nm array which is 201.8nm. This means as soon as superconductivity in islands is established, despite of the high contact resistance, proximity effect can easily travel to next island without much scattering for 200nm and 230nm pitch arrays. For 290nm array, on the other hand, electron transport behavior is diffusive. Although superconducting proximity effect is still present, electrons experience a lot of scattering and their trajectories are not well defined, therefore resistance of array drops slower and $T_3$ is pushed towards lower values.

Temperature dependence of $T_1$ may also relate to the volume of superconducting electrodes of a Josephson junction. Reduction of $T_1$ is not unique for Josephson junction array systems. It has also been reported in devices of copper loop connected by two superconducting electrodes[98], planar Josephson weak links[99] and 1D array-like Josephson links[100]. However, in these studies, they either did not pay attention to spacing-dependent proximity effect or they simply ignored the reduction of $T_1$ since it was very small. In the study of 1D array-like Josephson links, $T_1$ of a shorter link is lower than $T_1$ of a longer one as shown in figure 4.11. Metallic wire lengths of sample *15* and *18* are 0.8um,1.5um, respectively, but sample *18* exhibits a higher $T_1$. This indicates length of normal metal link is not a good parameter to study $T_1$. In their paper, authors also gave

other characteristic lengths of samples. For sample *15*, Cu wire width and thickness are 220nm and 155nm, width of Al electrodes is 120nm, for *18*, they are 50nm, 30nm and 175nm. Although Cu wire of sample *18* is longer than sample, the ratio of Cu wire volume to volume of overlapping Al electrode of sample *18* to sample *15* is about 0.26. If $T_1$ is not regulated solely by lengths of normal metal wires but by volume ratio between normal metal and superconducting electrodes,

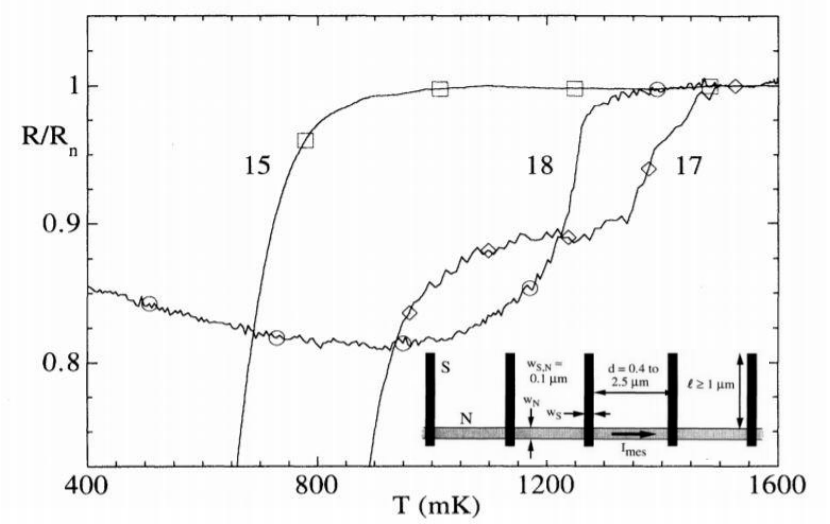


Figure 4.11 Temperature-dependent resistive transition of three samples from reference [Courtois, H., Gandit, P. and Pannetier, B. *Physical Review B*, *52*(2), p.1162], the inset is a sketch of geometry of part of a sample. Curves of sample *15* and *18* are measured on devices of Al electrodes connected by a Cu wire, the metallic wire of sample *17* is Ag. Length of Cu wire of sample 18, which set the spacing between Al electrodes, is longer than sample 15, but sample 18 has higher transition temperature. That may be due to the volume ratio of Al/Cu of sample 18 is bigger.

then this anomalous $T_1$ behavior can be easily understood. Of course, there may be other explanations to this anomalous $T_1$ behavior, but it is worthy noticing that the ratio of volumes of normal metal to superconducting electrodes is a reasonable starting point.

### 4.3.3 Resistive transition results of nanodot-island arrays on film 3642 $Bi_{0.7}Sb_{1.3}Te_3$ (BST)

In previous section, R-T results of arrays fabricated on the BS film have been discussed. In this section we will focus on arrays on the BST film. The $Bi_{0.7}Sb_{1.3}Te_3$ film used in this study has insulating bulk states, therefore, proximity induced superconductivity only exists in surface states. ARPES study of bilayer system of niobium/ $Bi_xSb_{(2-x)}Te_3$ has revealed that except for ultra-

thin films, for bulk-insulating film substrates, there is no coupling between top and bottom surface states which means proximity effect can only introduce superconductivity into the surface that directly touches niobium films[101]. To conclude, nanodot-island arrays fabricated on the 3642 BST films are ideal 2D platforms to study superconductivity of topological surface states, with information of c-axis superconductivity in bulking insulating $Bi_xSb_{(2-x)}Te_3$ from the ARPES study, this transport study on arrays provides findings of superconductivity in lateral direction.

### *4.3.3.1 R-T results*

Resistive transition results of three arrays fabricated on the BST film are displaced in figure 4.12. Reduction of $T_1$ with increasing spacing is also observed due to the same reason explained in last section. At 9K when niobium islands are in normal state, resistance of three arrays are close to each other due to the huge contact resistance, 6kΩ, compare to film resistance, 1.5kΩ, as discussed in before.

These arrays were firstly measured in a PPMS instrument with a base temperature of 0.7K. This base temperature is too high for critical transition of arrays, so arrays were then measured again in a dilution fridge with a 50mK base temperature. Plot A of figure 4.12 summarizes results obtained in the PPMS by DC current source and voltage meter, plot B shows results obtained in

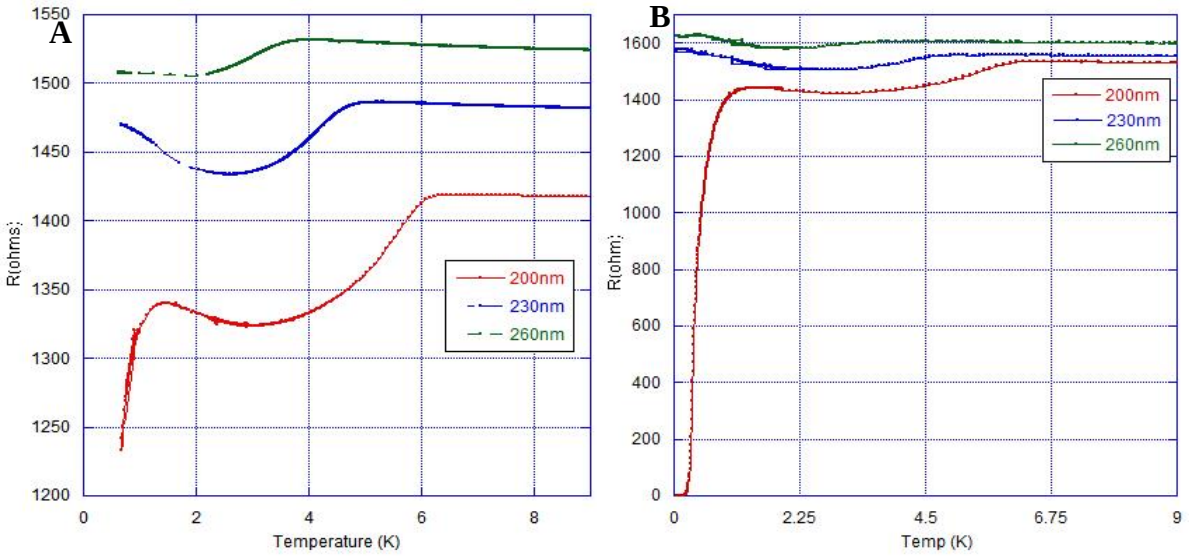


Figure 4.12 R-T results of arrays made on the BST. **(A)** High temperature part of R-T results measured using large current in PPMS, base temperature is 0.7K. **(B)** R-T results measured using two lock-in amplifiers in a dilution fridge with 50mK base temperature, AC voltage of 0.03 V, 30Hz was used. Load resistor is 1MΩ, current is about 25nA. 200nm pitch array reaches zero-resistance state.

the dilution fridge measured by two lock-in amplifiers. It has been noticed that resistances of arrays taken in the dilfridge are slightly higher than measured in PPMS. The exact reason for this difference is unclear. In previous section the parameters calculated from the transport model are based on results taken by the PPMS. This is to be consistent with the sheet resistance which was taken inside the PPMS equipment.

In the following parts, we will use the results obtained by lock-in amplifiers because lock-in amplifiers are more reliable for measurements requiring low current in the dilution fridge because it filters out unwanted signals by selectively measure the signal of frequency that matches the driving signal even at a driving current as low as 25nA.

#### *4.3.3.2 Compare R-T results of arrays on BST and BS films*

Next, we will discuss the major differences between arrays made of BS and BST films which are disappearance of $T_2$, resistance increase at $T_3$, reduction of $T_3$, and possible superconducting-insulating transition (SIT) as spacing increases. R-T results are shown in figure 4.13 including low temperature sheet resistance data of the BST film for convenience.

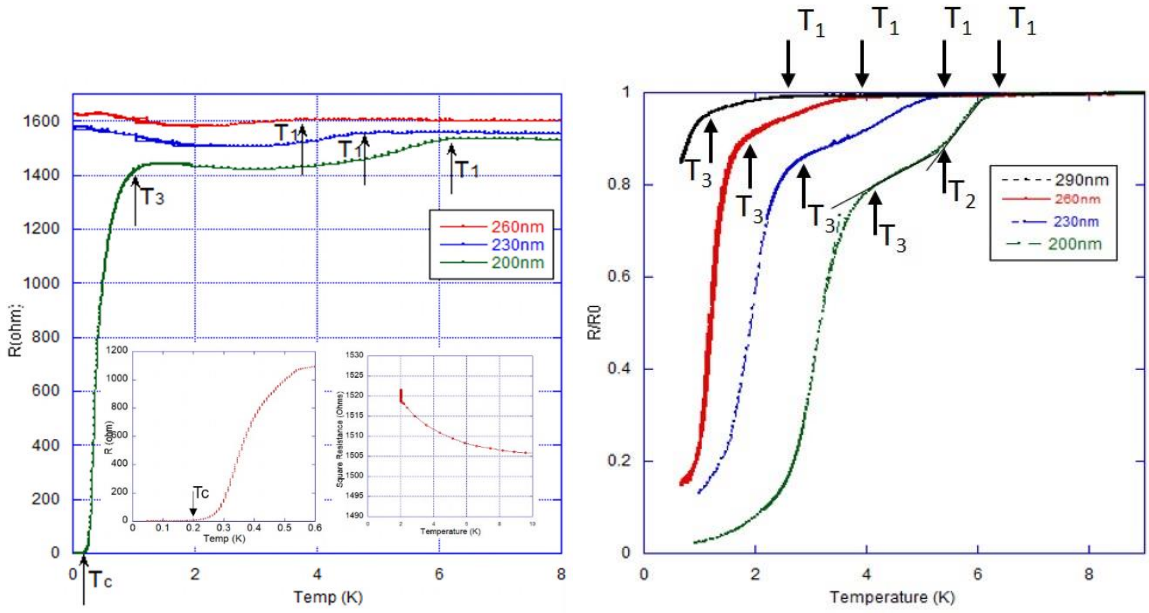


Figure 4.13 Comparison of R-T results of arrays made on the BS and BST films. Left one shows results for arrays on BST film, the left-side inset is a zoom-in view R-T of 200nm pitch array at very low temperature, the right-side inset is the 2D resistance of the BST film. All resistance is of one square measured area. $T_1$ and $T_3$ are marked for 200nm array curve. Tc is the temperature when array resistance is zero. It is very hard to define $T_2$ as it has been done for arrays on 3678 since between $T_1$ and $T_3$, slope change is very gradual, so $T_2$ is missing. Results of arrays on the BS film are shown on the right side.

The disappearance of $T_2$ is due to the short mean free path of film 3642. Mean free path of 3642 film is 25.6nm, smaller than 100nm spacing for 200nm pitch array. This means that for the smallest spacing array Josephson junctions are in diffusive regime. Since arrays fabricated on the BST film are all within diffusive limit, one should not expect them to have the same R-T transitions as of 200nm, 230nm or 260nm arrays of the BS film which are in ballistic region. The resistive transitions of arrays on the BST film are therefore similar to it of 290nm array on the BS film of which the spacing is 201.8nm. The inset of figure 4.13 shows that the resistance of the bare BST film increases at low temperature as temperature is lowered. This can explain the rocking shape of R-T curve around $T_3$. Although proximity effect makes resistance decrease, film intrinsic resistance increases at the same time. This competition between film resistance and proximity effect results the upwards bending shape of R-T curve after the initial drop starting from $T_1$. $T_3$ of 200nm pitch array on the BST film is below 1.4K while $T_3$ of 200nm array on the BS film is around 4K. Since they have the same structure in terms of pitch, spacing and island properties, this difference should be attributed to film property difference. As mentioned before, it has been revealed by ARPES that for bulk-insulating $Bi_xSb_{(2-x)}Te_3$ films, proximity effect is depressed due to lack of bulk carrier assistance and only top surface carriers contribute to transport. The BST film used for this study is free of bulk carriers, while the BS film has a lot of bulk carriers, therefore, $T_3$ of the arrays on the BST film is reduced.

#### *4.3.3.3 Superconducting-insulating (SI) transitions and BKT transitions of arrays on the BST film*

As spacing increases, R-T of arrays below $T_3$ changes from decreasing (200nm) to flat (230nm) and to increasing (260nm), showing a trend of SI transition. It is not clear why R-T curve of the 260 nm pitch array at low temperature firstly decreases then bend up, leaves a short tail of increasing resistance. Here we just discuss the possible SI transitions exhibited at the very low temperature. SI transitions have been observed on granular superconducting films made of small superconducting grains connected by

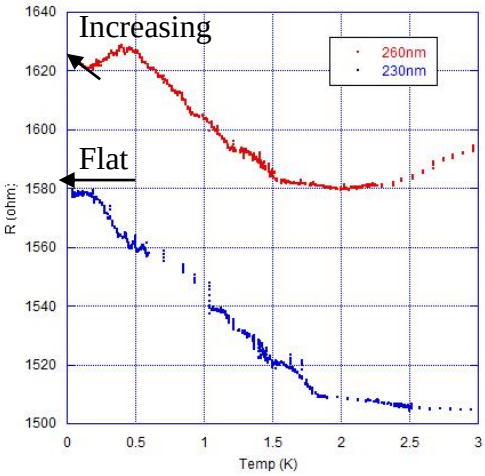

Figure 4.14 SIT behavior of arrays of 230nm and 260nm pitch sizes.

Josephson junctions, and on JJAs. It has been found that SI transitions are related to two factors, $R_N/R_Q$ and $x \equiv E_C/E_J$, here $R_N$ is normal state resistance of superconducting films or JJAs, $R_Q$ is resistance quantum, $R_Q = h/4e^2 \approx 6.45k\Omega$, and $E_J = \frac{\hbar I_C}{2e}$ is the Josephson coupling energy, $E_C = \frac{e^2}{2C}$ is the charging energy, *C* is the capacitance of the junction. SI transitions happen when $R_N/R_Q$ is greater than[102] 1 and when *x* is bigger than a certain value[103,104,105,106,107] (this value is not a definite number but should be less than 1). For nanodot-island arrays on the BST film, $R_N/R_Q$ ~ 0.25 which is less than 1, so SI transitions are not caused by $R_N/R_Q$. *x* is bigger than 1. The estimated *C* of each island is less than 2fF, here the capacitance between islands is ignored since it is much smaller than single island capacitance, relative permittivity of 10 is used, distance between capacitor plates is assumed to be 1nm for the maximum value of *C*. Critical current of a single junction of 200nm pitch array is 1.38nA. The estimated *x* of 200nm pitch array is 17. Since *x* is a magnitude bigger than 1, the nanodot-island JJAs should be categorized into quantum JJAs, quantum phase transition should be considered[108]. In classical theory of JJAs, for arrays with *x*>1, there should not be a superconducting phase, while the 200nm pitch array has a finite critical current. Theories have suggested that dissipation can assist superconducting phase transition[109] even for *x*>1 if normal state array resistance does not exceed the critical value of $h/4e^2$. However, for arrays of pitch size of 230nm and 260nm, although their normal state resistances are smaller than $h/4e^2$, they do not show any indication of superconducting phase. This indicates that inn quantum region, the superconducting phase requires not only the normal state resistance to be small, but also the distance between islands is very short[110]. Thus, for spacing bigger than 100nm, no superconducting phase exists, instead arrays show insulating behavior.

BKT fitting was also performed for the R-T data of 200nm array of the BST film, see figure 4.15. $T_{BKT}$ extracted from fitting is about 0.178K, $T_C$ obtained directly from R-T result is 0.18K. For JJAs with $x \equiv E_C/E_J$ >>1, BKT transition is expected to happen at temperature around $T \sim E_C/4k_B$[111,112,113], if assuming *C*=1fF, then $E_C/4k_B$ is 0.232K. We can also calculate $T_{BKT}$ using the $T_{BKT}=\pi E_J/2k_B$ for JJAs in classical limit, this gives $T_{BKT}$=0.324K which does not agree with the experimental value which is around 0.2K. Thus, it is more appropriate to treat the JJAs made on BST as quantum JJAs.

For $E_C/E_J$ of arrays on the BS film, although *C* should be smaller than 10fF since the island area is the same while the distance between capacitor plates should be longer than 1nm as bulk part of $Bi_2Se_3$ participates in transport as well, the $E_J$ increases as critical current is bigger ( for 200nm pitch array, critical current is about 25nA per junction) and normal array resistance is smaller, therefore, $E_C/E_J$ is <1 for 200nm pitch array . As array spacing increases, $E_C/E_J$ also increases but does not cross the critical value, all arrays exhibit trend of decreasing resistance as temperature lowers, transition temperature is pushed to lower value.

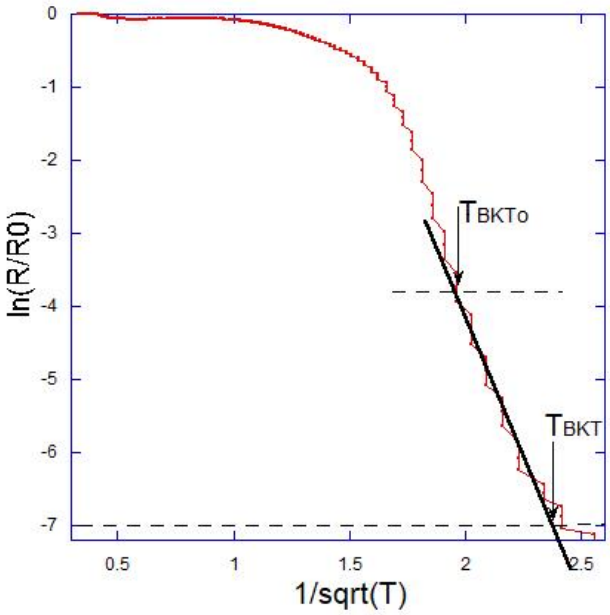


Figure 4.15 BKT fitting for R-T data of 200nm pitch array on film 3642. The $T_{BKTo}$ is defined as the onset temperature where the linearity relation starts to show up according to the fitting. $T_{BKT}$ is the temperature where $\ln(R/R_0)=-7$.

## 4.4 V-I and dV/dI-I Results

V-I and differential resistance (dV/dI) -I characteristics of 200nm array of the BST film have been measured by two-lockin set-up. The drive current comes from an ac voltage source in series with a 1MΩ resistor. The amplitude and phase of the current is measured in one lock-in by sensing the voltage across a 1kΩ resistor, while that the array voltage is measured by another lock-in. V-I curves of 200nm array of the BS film was also taken. All results are summarized in figure

4.16. Although affected by thermal rounding at high current and temperature which results earlier disappearance of critical current, both arrays show zero resistance state for current range up to 0.205uA(BST film) and 3.58uA (BS film) at 50mK. A BKT resistance transition has been observed in the V-I data at temperature of 200mK which is close to the value of $T_{BKT}$ obtained from R-T result fitting (178mK), the corresponding V-I curve is indicated by the green dashed line in the plot placed on the left side of the middle panel in figure 4.16.

### 4.4.1 $I_CR_N$ product

Regardless of the big difference of critical current of these two arrays, their $I_CR_N$ voltages are comparable. The measured $I_CR_N$ products of single junction are 2.08uV and 1.93uV for the 200nm pitch array of the BS and the BST film, respectively. $R_N$ refers to array resistance at 9K. This number is small compare to the superconducting gap of bulk niobium which is 1525uV. $I_CR_N$ is a characteristic factor of the quality of a Josephson junction, it should not depend on specific junction geometry but strongly depends on the quality of junction contact. The small $I_CR_N$ product suggests that junction contacts have smaller superconducting gap. Superconducting gap is reduced because of the effective insulating layer between niobium islands and TI films which is manifested as large contact resistance. In section 4.2.1, the SINIS model was proposed for arrays made on the BST film to explain the huge contact resistance, this SINIS model may be also applicable to arrays on the BS film because their gap size is similar to the size of gap in the array made on the BST film. The fact that these two arrays have almost the same $I_CR_N$ product suggests that for a Josephson junction of SINIS structure, the $I_CR_N$ product does not strongly dependent on carrier density of TI films under superconducting electrodes.

Depressed $I_C$ of array on the BST film should be attributed to the high normal state resistance which ultimately relates to the 2D nature of the surface state. As discussed earlier in section 4.1, the $Bi_xSb_{(2-x)}Te_3$ used in this study does not have bulk state, two surface states are completely decoupled, and only top surface state participates in Josephson coupling.

As for ratio of charging energy and Josephson coupling energy, $x \equiv E_C/E_J$, if assumed capacitances of both arrays are the same, then the ratio of $x$ of the array on the BST film to that the array on the BS film is about 17 due to difference of critical current. However, there has been a study showing that relative permittivity of $Bi_2Se_3$ film is thickness dependent[114], it is reasonable to suspect that the dielectric constant of a 30QL $Bi_2Se_3$ is different from that of a 60QL $Bi_xSb_{(2-x)}Te_3$ film. But this should not alter the conclusion that the JJAs made on the BS film is within

classical region since the resistance of all arrays shows a monotonic decreasing behavior below a certain temperature.

### 4.4.2 dV/dI-I results

Current-biased differential resistance (dV/dI-I) results taken at various temperatures of the 200nm pitch array on the BST film are shown in figure 4.16, the graph on the upper right corner.

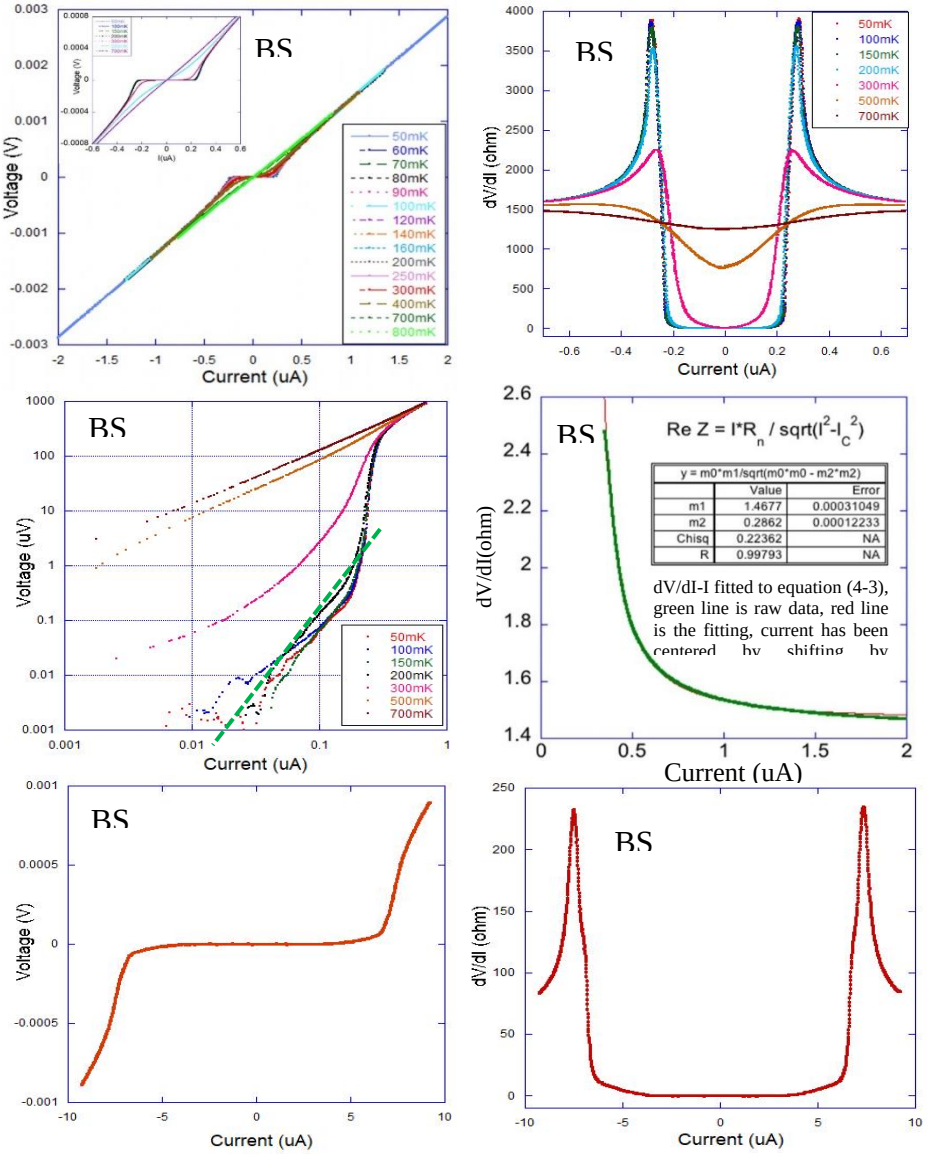


Figure 4.16V-I and dV/dI-I characteristics of 200nm array on the BST and the BS film. In the upper panel, the left on is V-I of the array of the BST film, data of temperature range from 50mK to 800mK are displayed, the inset shows V-I of smaller current range of selected temperatures, the right one is the differential resistance plotted as function of current. In the middle level, the left plot is the V-I of the 200nm pitch array on the BST film plotted in log-log scale; green dashed line indicates $V \sim I^3$ curve, the right one is dV/dI-I of $I_{bias} > I_C$ part fitted to the second part of equation (4-3), red line is the fitting curve, $R_n$ and $I_C$ obtained from the fitting are 1467 Ω and 286 nA.In the lower panel, V-I and dV/dI-I results of 200nm pitch array on the BS film.

Having small capacitance and small critical current, the condition of dimensionless parameter $\beta_C = \frac{2eI_cC}{\hbar\sigma^2} \ll 1$ is valid so Josephson junctions in the array are overdamped. Overdamped Josephson junction can be modeled by the RSJ circuit and its V-I characteristics can be described using relation (4-3). Indeed the (dV/dI-I) results show typical behavior of overdamped Josephson junctions, the curve taken at the lowest temperature shows sharp explosion peak when $I_{bias}=I_C$ and fits the theoretical calculation (4-3) for RSJ model very well, see plot on the right side of the middle panel of figure 4.16.

$$< V >= \begin{cases} 0\,, & (when\ \ I_{bias} < I_c) \\ R_n\sqrt{I_{bias}^2 - I_c^2}, & (when\ I_{bias} > I_c) \end{cases} \qquad (4\text{-}3)$$

The broadening effect at high current limit which becomes more prominent at higher temperatures could be due to the thermal noise according to the theory of Ambegaokar and Halperin[89] that has been seen in current-voltage characteristics of Josephson junctions[115] , see figure 4.17 for reference. As shown in figure 4.17, the factor $\gamma \equiv \frac{\hbar I_C}{ekT}$, denotes thermal noise effect level, higher γ means less effect. The dV/dI-I curves were taken at 50mK, leads to $\gamma$ =1.32. For such a small γ, obvious thermal noise effect is not surprising.

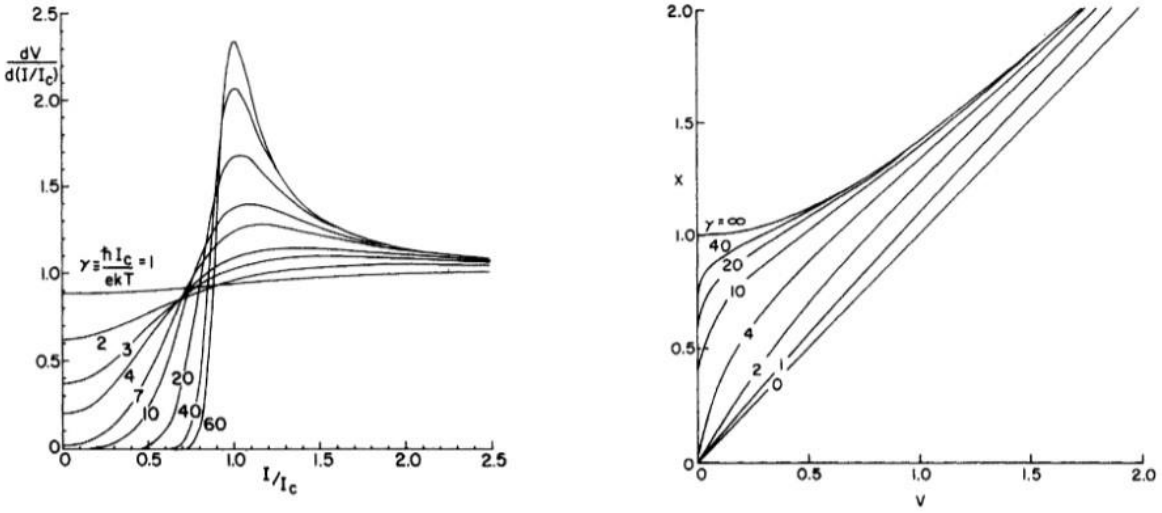


Figure 4.17 Theoretical dV/dI-I and V-I characteristics of a Josephson junction with different level of effect of thermal noise. The factor γ denotes thermal noise level, higher γ means less effect. This figure is from reference [115].

### 4.4.3 Temperature dependent critical current

Temperature dependence of critical current for the 200nm pitch array on the BST film is plotted in figure 4.18. The critical current per junction is obtained from the measured critical current for the array as shown in figure 4.16 by dividing the total current by 150 ( the number of islands in each row, recall the array is 30um by 30um and the pitch size is 200nm in both directions for this array), this takes the low temperature limit for the array critical current of 205nA to 1.38nA per junction. The temperature dependence of critical current of a Josephson junction is given by the Ambegaokar-Baratoff[116] formula:

$$I_C = \frac{\pi \Delta(T)}{2eR_N} \tanh\left(\frac{\Delta(T)}{2kT}\right) \qquad (4\text{-}4)$$

$\Delta(T)$ is the energy gap of superconductor electrodes, $k$ is Boltzmann constant, $e$ is one electron charge. This formula can be used to obtain $\Delta(T)$. We have a more complicated structure than that analyzed in ref[116]. We have strong superconductor, niobium, coupled to the electrons of the TI directly below the island. The Josephson weak link is between the proximity induced 2D topological superconducting electrons in the region below adjacent islands, and the value of $\Delta(T)$

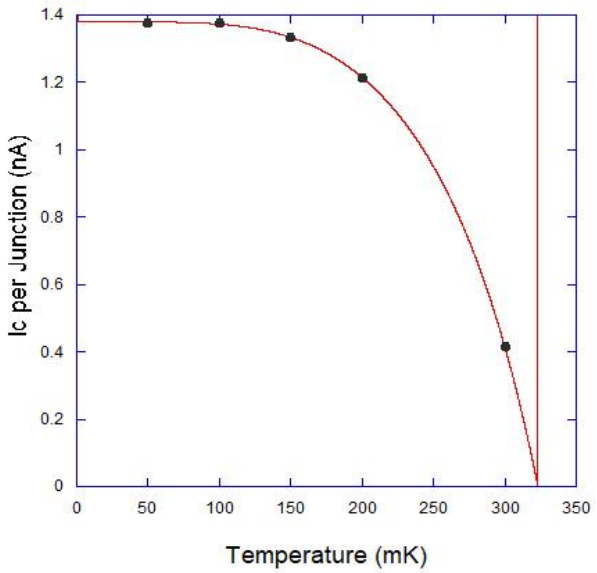


Figure 4.18 Temperature dependence of critical current. Black dots are experimental values of critical current extracted from V-I curves presented in figure 4.16, red line is the $I_C(T)$ fitted to Ambegaokar-Baratoff theory. The temperature dependence of superconducting gap used in the fitting is $\Delta(T) = \Delta(0)\sqrt{1 - (\frac{T}{T_C})^4}$. $T_C$ obtained from fitting is 323mK.

obtained here is the value in the proximity induced topological superconductor. For temperature close to zero, Ambegaokar-Baratoff relation reduces to :

$$I_C(0) = \frac{\pi\Delta(0)}{2eR_N} \qquad (4\text{-}5)$$

This yields $\Delta(0)$=1.34ueV, assuming this formula still hold, and critical current is the same as the value at 50mK.

### 4.4.4 Theory of the Critical Current and Gap value.

We have two quantities, IcRn and critical current value, that we can obtain directly from the experiment. From these two numbers we can calculate the gap value using Ambegaokar-Baratoff formula and find out what the kinetic energy of the pairs is at the critical current value, we find those are close to be the same number, this rules out that flux flow for the critical current. Here we are going to show how we get the kinetic energy.

Looking at figure 4.16 we see that the V-I curves exhibit agreement with the shape predicted by the RCSJ model. In particular, formula 4.3 describes how the finite voltage appears

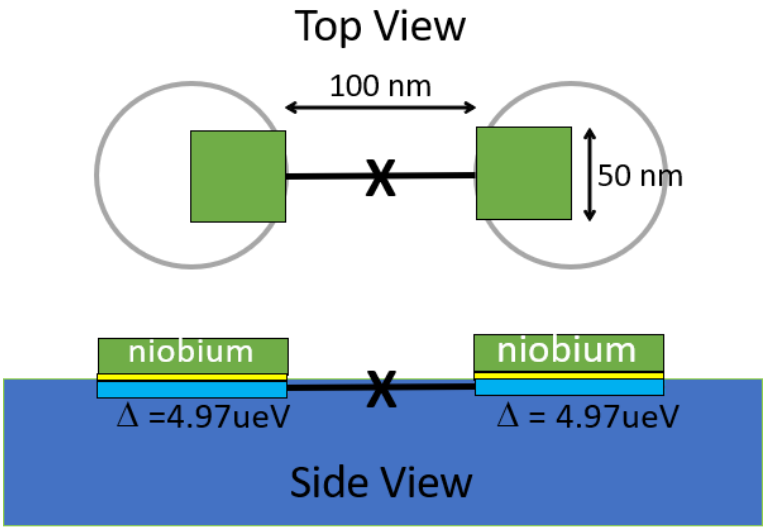


Figure 4.19 Josephson junction model which allows parameters to be identified. Two adjacent islands are shown as gray circles. We approximate the dimensions of the Josephson connection to be 50 nm wide and 100 nm long and figure that this will be a good approximation to the actual island coupling. Superconductivity below the island has a smaller gap than the inducing niobium because of the tunnel junction that separates the island from the TI surface state. The weak link is between induced puddles of superconductivity.

above $I_C$ and the right middle panel of the figure shows that the measured data agrees well with the model. It is also interesting to note that the measured critical current at low temperatures of approximately 1.4 nA per junction provides an estimate of the velocity the pairs have when they reach the critical current. At this point it is necessary to account for the geometry of the device in a more accurate manner. Figure 4.19 shows a functional schematic view of our model for a junction between two adjacent islands along with the model feature sizes in the 200 nm pitch array. In this model the resistance of the junction is two times the 2D resistivity of the film or 3000 Ohms. The measured resistance of the device is half of that, but in order to use formula (4-4) to get the superconducting gap energy, we should only use the channel carrying the supercurrent and we expect that spans the point of closest approach of the islands, hence the light blue region in figure 4.19. The measured Ic per junction at 50 mK is 205 nA /150 or 1.33 nA, since there are 150 junctions in parallel. This gives $I_C R_N$ per junction equal to 4.2uV. Using this number in equation (4-4)we obtain a value of 4.97 ueV for the gap energy, Δ.

If the measured critical current density at 50 mK is $I_C$, then the sheet critical current density is $K = I_C/w$, where Ic is of per junction, where $w$ is the width of each junction perpendicular to the current flow direction. The area density of pairs is not the total number of electrons but rather the number of electrons with energy within the gap. To see this, it is useful to separate out the current carried by composite bosons and the current carried by fermions. The fermion current is zero if the voltage is zero. Ultimately this is because of the energy gap in the fermionic spectrum. The boson condensate exists at the chemical potential and has a number density driven by the pairing potential,$n_{pair} = D(0)\Delta/2$, where D(0) is the fermionic density of states at the chemical potential. In terms of the Dirac band structure of the 2D surface topological band, this is given by $n_{pair} = \frac{1}{2} 2\pi k_F \frac{\partial k}{\partial E} \Delta$, where $\mathrm{E(k)} = \hbar k \mathrm{v_F}$. This results in $n_{pair} = \frac{1}{2} \frac{2\pi k_F \Delta}{\hbar \mathrm{v_F}}$ pairs of charge $2e$ per square meter. Since the sheet current density can also be given by $K = 2e v_{pair} n_{pair}$, we can solve for $v_{pair}$ to find out how fast each pair moves at the critical current. Working out the algebra we find that $v_{pair} = I_C \hbar v_F / 2\pi e w k_F \Delta$. Numerically this is $v_{pair} = 1712$ m/s.

Now the question remains, how much kinetic energy does a pair have when the current reaches the critical value. There is a problem here. If the quasiparticles are massless, it would seem that the kinetic energy change should be zero. However, it is easy to see that this is not the case. Other massless particles such as photons are changed in energy when viewed from different

inertial reference frames. We adopt another approach to find the kinetic energy difference a moving pair has. Since the change in electron state occupancy is not large and occurs only very near the Fermi energy, we can find an alternate massive band having the same Fermi momentum and Fermi velocity, use the effective mass value that this band has and calculate the pair kinetic energy from $E_{PK} = 2m^* v_{pair}^2/2$, where m* is the effective mass and $E_{PK}$ is the extra pair kinetic energy and the factor of 2 comes from the number of electrons in a pair. To carry this out we note that for any band, the Fermi velocity is $v_F = \frac{\partial E}{\partial k\hbar}$ . For a Dirac band with dispersion $E_D(k) = \hbar k \mathrm{v_F}$ this is just $v_F$. For a parabolic massive band with dispersion $E_P(k) = \hbar^2 k^2/2m^*$, this is $v_F = \hbar \mathrm{k_F}/\mathrm{m}^*$ . Given that $k_F = 7 \times 10^8/m$ and $v_F = 3.5 \times 10^5 m/s$, this gives equivalent dispersion at $E_F$ in a massive system with $m^* = \frac{\hbar \mathrm{k_F}}{\mathrm{v_F}} = 0.232\mathrm{m_e}$, where both the Fermi wave number and Fermi velocity are experimentally measured quantities. Note that for the parabolic band the Fermi energy is $E_P(k_F) = \hbar \mathrm{k_F v_F}/2$, while for the Dirac band the Fermi energy is twice as large, $E_D(k_F) = \hbar k_F \mathrm{v_F}$. The situation is as depicted in figure 4.20.

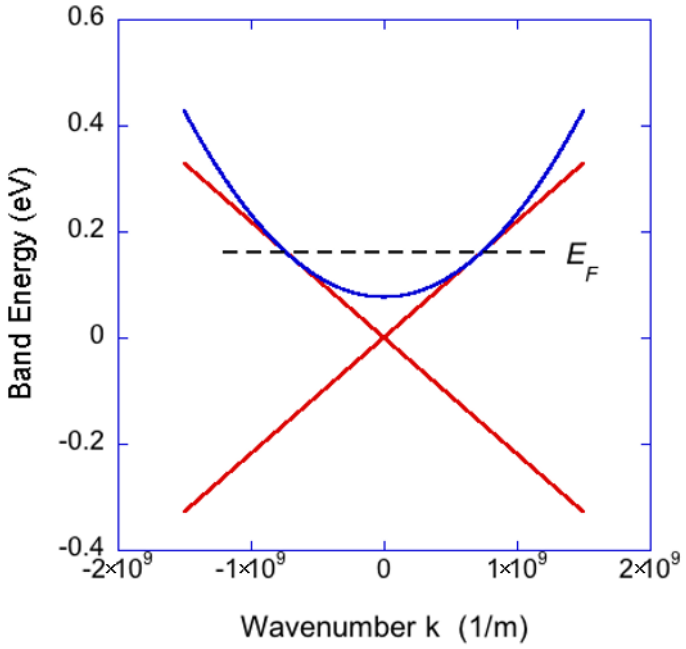


Figure 4.20 Equivalent dispersion of a Dirac band and a parabolic band at the Fermi energy. Note that the Fermi energy measured from the bottom of the bands is different, but the Fermi momentum and the Fermi velocity for these two types of dispersion are identical.

Using this we find that the kinetic energy of the pair at the critical current value is $E_{PK} = 3.87\mu eV$. This value is comparable to the gap value we derived from the V-I curves. Apparently, we can account for the size of the critical current by kinetic pair breaking and not vortex motion through the junction.

## 4.5 Magnetoresistance Results

The magnetoresistance (MR) of 200nm pitch array on the BS film and the BST film are shown in figure 4.21. MR of the array on the BS film was taken in a PPMS at 0.8K by measuring resistance while sweeping the field, MR of the array on the BST film was converted from dV/dI-I results taken at different field values in a dilution fridge at 50mK, original dV/dI-I data is shown in the inset .

Unlike square-island arrays, here the MR dip at *f*=2 is not missing. Since only one MR data

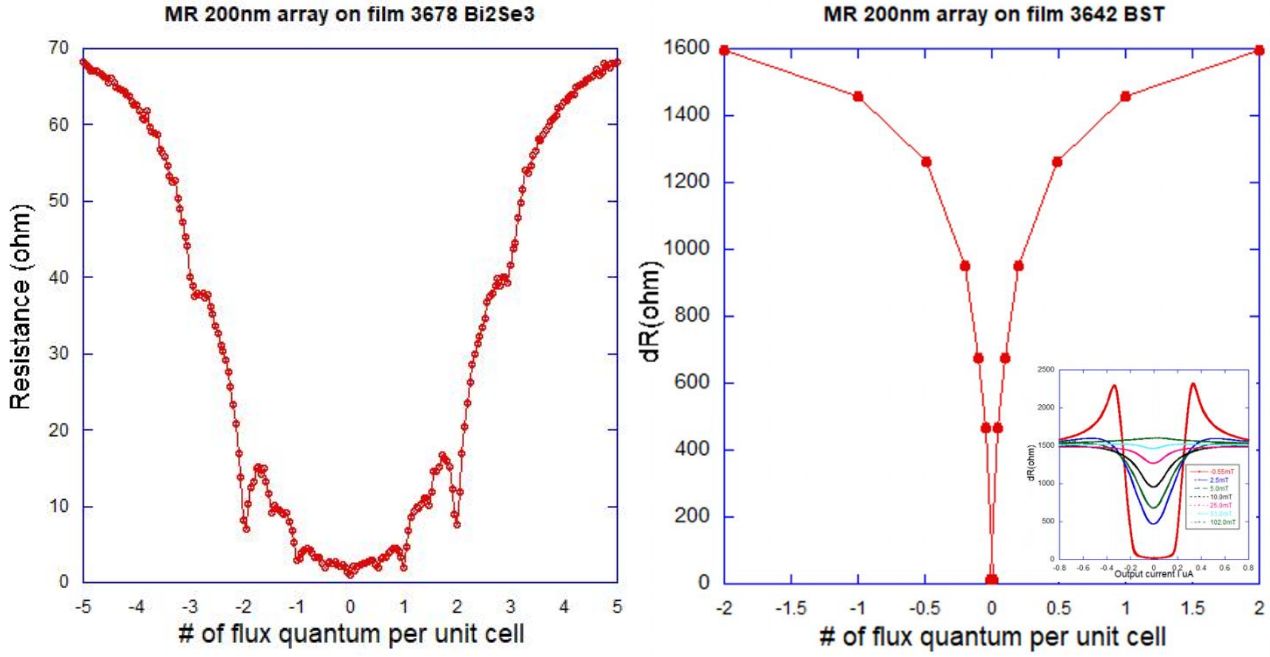


Figure 4.21 Magnetoresistance-number of fluxes results of the array on the BS film taken at 0.8K and the array on the BST film taken at 50mK, current is 1uA and 50nA, respectively. Pitch size is 200nm, area of each unit cell is 0.04um$^2$.

is taken, it is impossible to give a conclusive reason for the appearance of *f*=2 dip, it is possible the presence of it is due to the absence of eggcrate shape pinning potential of square-island arrays,

therefore all vortex pining sites are equivalent. More experiments are required to answer why the dip of $f$=2 presents in MR of nanodot-island arrays but not square-island arrays.

MR of the array on the BST film does not show any indications of dips. Dips in MR are due to vortex pining, the fact that there is no dip may suggest that the TSC induced in this array is not a collection of TSC induced in film area under many nano niobium dots, but a coarse-grained TSC that expands across the entire array.

## 4.6 Conclusion

With the composition carefully tuned, $Bi_xSb_{(2-x)}Te_3$ films of ultra-low carrier density have been grown. Combined with ARPES taken at films with similar composition, the $Bi_xSb_{(2-x)}Te_3$ film used in this study should not have any bulk carriers and top and bottom surface states are not coupled.

Nanodot-island niobium arrays have been fabricated on a bulk-insulating BST film. To make sure the electrodynamic properties of arrays are controlled mostly by the BST film, spacings between islands are made longer than coherence length of niobium (38nm) and island size are restricted to small values with best effort (diameters is around 100nm). From R-T and V-I results, zero-resistance and critical current have been observed which indicates that the proximity effect induced superconductivity of surface state has been achieved. It is found that the spacing dependent first resistance drop temperature is strongly affected by contact quality (transfer length and tunneling coefficient) which directly affects the strength of proximity coupling. Dot-shape contact results long transfer length and low tunneling coefficient. Absence of bulk carriers in the BST film further lowered the contact conductance and tunneling coefficient, resulting smaller critical current and temperature.

BKT transition has also been observed in the array made on the BST film, transition temperature has been extracted from theoretical fitting. Using Ambegaokar-Baratoff relation, from temperature dependence of critical current of 200nm pitch array on the BST film, the energy gap of the proximity induced topological superconductivity is extracted.

As a comparison, nanodot-island arrays have also been fabricated on a $Bi_2Se_3$ film which has bulk carriers. With bulk carriers, arrays have higher critical current and superconducting transition temperature. $I_CR_N$ products of arrays on both films are comparable and smaller than the gap size of bulk niobium. With the information of high contact resistance, we conclude that $I_CR_N$

products of arrays are not regulated by niobium superconducting gap, but the gap induced by proximity effect in the surface state of the film area under islands.

# CHAPTER 5: CONCLUSION

## 5.1 Summary of Thesis work

In this thesis study, we have successfully realized topological superconductivity (TSC) that is free of bulk superconductivity contamination. This is achieved by making use of the superconducting proximity effect to induce superconductivity (SC) into the top surface of a topological insulator (TI) thin film. This TI film is bulk insulating and its two surface states are decoupled. We placed niobium islands on the TI film as the donor of SC. To make sure the induced TSC is dominated by the electrodynamics of TI carriers, we limited the size of niobium islands to be less than 100nm. Zero-resistance stage observed from R-T results and critical current from V-I results confirmed the TSC. This kind of TSC is ideal to study Majorana Zero Modes (MZMs) that have been predicted to appear in cores of vortices of a topological superconductor.

We have studied the properties of proximity induced superconductivity in big square-island arrays and nanodot-island arrays. In big square-island arrays, we compared results of arrays made on films of different morphologies and found that the proximity effect is stronger in arrays made on bumper films. This is due to the bumper films provide more ab-plane conducting channels which have higher conductance than c-direction channels d. In nanodot-island arrays, it was found that arrays made on the BST film which only has 2D carriers have significant low contact conductance compared to arrays made on the BS film which has 3D carriers. We quantified the 2D carrier conductance by multiplying a factor of $\alpha$ to the conventional 3D contact conductance, the value of $\alpha$ was derived from experimental data.

We have also studied physics of Josephson junction arrays. Spacing-dependent proximity effect and superconducting transition temperature have been discussed in detail for both square and dot arrays. Shapiro steps measurements were performed for big square-island arrays, results suggest the array can persist superconducting coherence across the entire array. Evidence for BKT transition have been observed, transition temperature has been extracted from R-T and V-I results. Magnetoresistance (MR) of arrays made on BS films were measured, vortex dynamics coded in the MR results have been discussed.

## 5.2 Future work

More experiments are needed to complete the picture of spacing-dependent transition temperature of the first resistance drop observed in R-T results in nanodot-island arrays. From the thesis work, we know it is due to the proximity effect and it is more obvious in arrays of smaller islands. But a quantitative relation among the temperature, the spacing, the island size is not obtained yet. A systematic study can be conducted with carefully designed and characterized film carrier density, morphology, island shape and size, and spacings.

The SI transitions observed in the R-T results for arrays fabricated on the BST film is worth investigating. From presented results, we know that this SI transition is spacing dependent and maybe also carrier dependent. The spacing-dependence is self-explanatory since longer spacing gives higher shutting resistance. The SI transition only showed up in arrays on the BST film not in arrays on the BS film, it is natural to suspect that the SI transition is related to the difference between 2D and 3D carriers. This can be investigated by measuring the R-T of nanodot-island arrays made on BS film with different fraction of 2D carriers ( can be easily achieved by varying thickness of the film), from low fraction (thick film ) to high fraction (ultrathin film), and observing arrays of the same spacing exhibit different behaviors and maybe even show SI translations. Alternatively, BS films can be substituted by BST films of different carrier densities by varying Sb/Bi ratio while keeping the thickness constant.

Now that the TSC desired for MZMs is handy, next we can perform measurements that are sensitive to vortex dynamics such as STS to further study the property the TSC and try to capture signatures of MZMs such as the zero-bias conductance peak. We can also probe the superconducting paring symmetry of the induced TSC by testing dc SQUIDs consisting of nanodot-island arrays. Based on the theoretical calculation, the paring symmetry should be $p_x+ip_y$.

# APPENDIX LITHOGRAPHY PROCESS OF ARRAYS

Different E-beam resists are used for fabrication of square-island and nanodot-island arrays. For square-island arrays, regular PMMA works well. While for nanodot-island arrays, to achieve well defined dots within small pitch limit (20nm), ZEP-520A7 E-beam resist was used. ZEP-520A7 is very resistive to overdevelopment.

The following process is a good guide to start with, adjustments to parameters are needed to achieve best results.

## Lithography process of square-island arrays

1. Clean films using IPA, avoid sonication because it introduces cracks and film pilling off . Dry with compressed $N_2$ gas.
2. Spin two layers of PMMA and one layer of AquaSave.
   1st layer: 3000 rpm, 60 seconds. Bake at 105◦C for 2mins.
   2nd layer: 3000 rpm, 60 seconds. Bake at 180◦C for 5mins.
   Spin AquaSave as a conductive layer at 3000 rpm for 60 seconds, bake at 105◦C for 1min.
3. Write alignment marks and niobium islands using Raith E-line.
   20um aperture, 20kV, WD=10m, dosage: 240-300 uC/$cm^2$.
4. Write trenches that define contact pads and a long hall bar.
   120um aperture, 10kV, WD=10mm, dosage: 260 uC/$cm^2$.
5. Niobium pads and strips (optional). This step can be added to deposit niobium layer on contact pads and on film area between arrays of various spacings to minimize heat dissipation.
   120um aperture, 10kV, WD=10mm, dosage: 260 uC/$cm^2$.

## Lithography process of nanodot-island arrays

1. Clean films using IPA, avoid sonication because it introduces cracks and film pilling off . Dry with compressed $N_2$ gas.
2. Spin one layer of diluted ZEP-520A and one layer of AquaSave. The diluted ZEP520-A7 is a mixture of ZEP520-A7 and Anisole of 1:1 ratio. Diluted resist requires lower clear dose and saves E-beam writing time.

5000 rpm, 60 seconds. Bake at 180◦C for 3mins.

Spin AquaSave as a conductive layer at 3000 rpm for 60 seconds, bake at 105◦C for 1min.

3. Write alignment marks and niobium islands using Raith E-line.

   Alignment marks: 20um aperture, 10kV , dose: 120uC/$cm^2$

   Nanodot-island arrays: 10um aperture, 10kV, dot dose: 0.0055pC

4. Write trenches that define contact pads and a long hall bar.

   120um aperture, 10kV, WD=10mm, dosage: 120uC/$cm^2$.

5. Niobium pads and strips (optional). This step can be added to deposit niobium layer on contact pads and on film area between arrays of various spacings to minimize heat dissipation.

   120um aperture, 10kV, WD=10mm, dosage: 120 uC/$cm^2$.

## REFERENCES


[1] Wang, M.X., Liu, C., Xu, J.P., Yang, F., Miao, L., Yao, M.Y., Gao, C.L., Shen, C., Ma, X., Chen, X. and Xu, Z.A., 2012. The coexistence of superconductivity and topological order in the Bi2Se3 thin films. *Science*, *336*(6077), pp.52-55.

[2] Nash, C., 1999. Topology and physics—a historical essay. *History of topology*, pp.359-415.

[3] Thouless, D.J., Kohmoto, M., Nightingale, M.P. and den Nijs, M., 1982. Quantized Hall conductance in a two-dimensional periodic potential. *Physical review letters*, *49*(6), p.405.

[4] Kohmoto, M., 1985. Topological invariant and the quantization of the Hall conductance. *Annals of Physics*, *160*(2), pp.343-354.

[5] Kane, Charles L., and Eugene J. Mele. *Physical review letters* 95.14 (2005): 146802.

[6] Bernevig, B. Andrei, Taylor L. Hughes, and Shou-Cheng Zhang. *Science* 314.5806 (2006): 1757-1761.

[7] König, Markus, et al. *Science* 318.5851 (2007): 766-770.

[8] Kane, C.L., 2013. Topological Band Theory and the $\mathbb{Z}2$ Invariant. In *Contemporary Concepts of Condensed Matter Science* (Vol. 6, pp. 3-34). Elsevier.

[9] JE Moore and L. Balents, Phys. Rev. B 75, 121306(R) (2007)

[10] Fu, L. and Kane, C.L., 2007. Topological insulators with inversion symmetry. *Physical Review B*, *76*(4), p.045302.

[11] Hsieh, David, et al. *Nature* 452.7190 (2008): 970-974.

[12] Zhang, Haijun, et al. *Nature physics* 5.6 (2009): 438-442.

[13] Xia, Yuqi, et al. *Nature Physics* 5.6 (2009): 398-402.

[14] Chen, Y. L., et al. *science* 325.5937 (2009): 178-181.

[15] Hsieh, David, et al. *Physical review letters* 103.14 (2009): 146401.

[16] Jiang, Yeping, et al. *Physical review letters* 108.1 (2012): 016401.

[17] Chang, C.Z., et al. 2015. Band engineering of Dirac surface states in topological-insulator-based van der Waals heterostructures. *Physical review letters*, *115*(13), p.136801.

[18] Taskin, A. A., and Yoichi Ando. *Physical Review B* 80.8 (2009): 085303.

[19] Hsieh, David, et al. *Science* 323.5916 (2009): 919-922.

[20] Roushan, Pedram, et al. *Nature* 460.7259 (2009): 1106-1109.

[21] Fu, Liang, and Charles L. Kane. *Physical review letters* 100.9 (2008): 096407.

[22] Xia, Yuqi, et al. *Nature Physics* 5.6 (2009): 398-402.

[23] Bianchi, Marco, et al *arXiv preprint arXiv:1009.2879* (2010).

[24] P. Hosur, P. Ghaemi, R. S. K. Mong, and A. Vishwanath, Phys. Rev. Lett. 107, 097001 (2011).

[25] Lee, Kyungmin, et al. *Physical Review B* 90.21 (2014): 214510.

[26] Wang, Mei-Xiao, et al. *Science* 336.6077 (2012): 52-55.

[27] Xu, Jin-Peng, et al. *Physical review letters* 114.1 (2015): 017001.

[28] Abraham, David W., et al. *Physical Review B* 26.9 (1982): 5268.

[29] Lobb, C. J., David W. Abraham, and M. Tinkham. *Physical Review B* 27.1 (1983): 150.

[30] Eley, Serena, et al. *Nature Physics* 8.1 (2012): 59-62.

[31] Doctoral thesis of Charlotte Georgine Lang Bøttcher
http://qdev.nbi.ku.dk/student_theses/Thesis_CharlotteGLBoettcher (2016)

[32] Zhang, H., Liu, C., Qi, X. *et al.* Topological insulators in $Bi_2Se_3$, $Bi_2Te_3$ and $Sb_2Te_3$ with a single Dirac cone on the surface. *Nature Phys* **5,** 438–442 (2009).

[33] Kong, D., Chen, Y., Cha, J. *et al.* Ambipolar field effect in the ternary topological insulator $(Bi_xSb_{1-x})_2Te_3$ by composition tuning. *Nature Nanotech* **6,** 705–709 (2011).

[34] Tinkham, Michael. *Introduction to superconductivity*. Courier Corporation, 2004.

[35] Pannetier, B., Courtois, H. Andreev Reflection and Proximity effect. *Journal of Low Temperature Physics* **118,** 599–615 (2000)

[36] Josephson, Brian. "Possible new effect in superconducting tunneling." *Phys. Lett.* 1 (1962): 251-253.

[37] Anderson, Philip W., and John M. Rowell. "Probable observation of the Josephson superconducting tunneling effect." *Physical Review Letters* 10.6 (1963): 230.

[38] Shapiro, Sidney. "Josephson currents in superconducting tunneling: The effect of microwaves and other observations." *Physical Review Letters* 11.2 (1963): 80.

[39] Ambegaokar, V. and Baratoff, A., 1963. Tunneling between superconductors. *Physical Review Letters*, *10*(11), p.486.

[40] Williams, J.R., Bestwick, A.J., Gallagher, P., Hong, S.S., Cui, Y., Bleich, A.S., Analytis, J.G., Fisher, I.R. and Goldhaber-Gordon, D., 2012. Unconventional Josephson effect in hybrid superconductor-topological insulator devices. *Physical review letters*, *109*(5), p.056803.

[41] Majorana, E., 1937. Teoria simmetrica dell'elettrone e del positrone. *Il Nuovo Cimento (1924-1942)*, *14*(4), p.171.

[42] Kitaev, A.Y., 2003. Fault-tolerant quantum computation by anyons. *Annals of Physics*, *303*(1), pp.2-30.

[43] Fu, Liang, and Charles L. Kane. *Physical review letters* 100.9 (2008): 096407.

[44] Read, N. and Green, D., 2000. Paired states of fermions in two dimensions with breaking of parity and time-reversal symmetries and the fractional quantum Hall effect. *Physical Review B*, *61*(15), p.10267.

[45] Ivanov, D.A., 2001. Non-Abelian statistics of half-quantum vortices in p-wave superconductors. *Physical review letters*, *86*(2), p.268.

[46] Stern, A., von Oppen, F. and Mariani, E., 2004. Geometric phases and quantum entanglement as building blocks for non-Abelian quasiparticle statistics. *Physical Review B*, *70*(20), p.205338.

[47] Stone, M. and Chung, S.B., 2006. Fusion rules and vortices in p x+ i p y superconductors. *Physical Review B*, *73*(1), p.014505.

[48] Zhang, D., Wang, J., DaSilva, A.M., Lee, J.S., Gutierrez, H.R., Chan, M.H., Jain, J. and Samarth, N., 2011. Superconducting proximity effect and possible evidence for Pearl vortices in a candidate topological insulator. *Physical Review B*, *84*(16), p.165120

[49] Sacépé, B., Oostinga, J.B., Li, J., Ubaldini, A., Couto, N.J., Giannini, E. and Morpurgo, A.F., 2011. Gate-tuned normal and superconducting transport at the surface of a topological insulator. *Nature communications*, *2*(1), pp.1-7.

[50] 2012 Ti/Al-Bi2Se3-Ti/Al Williams, J.R., Bestwick, A.J., Gallagher, P., Hong, S.S., Cui, Y., Bleich, A.S., Analytis, J.G., Fisher, I.R. and Goldhaber-Gordon, D., 2012. Unconventional Josephson effect in hybrid superconductor-topological insulator devices. *Physical review letters*, *109*(5), p.056803.

[51] 2014 Al-Bi2Se3-Al Galletti, L., Charpentier, S., Iavarone, M., Lucignano, P., Massarotti, D., Arpaia, R., Suzuki, Y., Kadowaki, K., Bauch, T., Tagliacozzo, A. and Tafuri, F., 2014. Influence of topological edge states on the properties of Al/Bi 2 Se 3/Al hybrid Josephson devices. *Physical Review B*, *89*(13), p.134512.

[52] 2014 Nb-Bi2Se3-Nb Kurter, C., Finck, A.D.K., Ghaemi, P., Hor, Y.S. and Van Harlingen, D.J., 2014. Dynamical gate-tunable supercurrents in topological Josephson junctions. *Physical Review B*, *90*(1), p.014501.

[53] 2012 Nb-Bi2Te3-Nb Veldhorst, M., Snelder, M., Hoek, M., Gang, T., Guduru, V.K., Wang, X.L., Zeitler, U., van der Wiel, W.G., Golubov, A.A., Hilgenkamp, H. and Brinkman, A., 2012. Josephson supercurrent through a topological insulator surface state. *Nature materials*, *11*(5), pp.417-421.

[54] 2012 Pb-Bi2Te3-Pb Qu, F., Yang, F., Shen, J., Ding, Y., Chen, J., Ji, Z., Liu, G., Fan, J., Jing, X., Yang, C. and Lu, L., 2012. Strong superconducting proximity effect in Pb-Bi 2 Te 3 hybrid structures. *Scientific reports*, *2*, p.339.

[55] J. P. Xu, M. X. Wang, Z. L. Liu, J. F. Ge, X. Yang, C. Liu, et al., "Experimental detection of a Majorana mode in the core of a magnetic vortex inside a topological insulator-superconductor Bi2Te3/NbSe2 heterostructure," Phys Rev Lett, vol. 114, p. 017001, Jan 9 2015.

[56] Sun, H.H., Zhang, K.W., Hu, L.H., Li, C., Wang, G.Y., Ma, H.Y., Xu, Z.A., Gao, C.L., Guan, D.D., Li, Y.Y. and Liu, C., 2016. Majorana zero mode detected with spin selective Andreev reflection in the vortex of a topological superconductor. *Physical review letters*, *116*(25), p.257003.

[57] Hor, Y.S., Williams, A.J., Checkelsky, J.G., Roushan, P., Seo, J., Xu, Q., Zandbergen, H.W., Yazdani, A., Ong, N.P. and Cava, R.J., 2010. Superconductivity in Cu x Bi 2 Se 3 and its implications for pairing in the undoped topological insulator. *Physical review letters*, *104*(5), p.057001.

[58] Liu, Z., Yao, X., Shao, J., Zuo, M., Pi, L., Tan, S., Zhang, C. and Zhang, Y., 2015. Superconductivity with topological surface state in Sr x Bi2Se3. *Journal of the American Chemical Society*, *137*(33), pp.10512-10515.

[59] Zhang, P., Yaji, K., Hashimoto, T., Ota, Y., Kondo, T., Okazaki, K., Wang, Z., Wen, J., Gu, G.D., Ding, H. and Shin, S., 2018. Observation of topological superconductivity on the surface of an iron-based superconductor. *Science*, *360*(6385), pp.182-186.

[60] Clark, T. D., and D. R. Tilley. "Resistive transition tailing in an array of Josephson junctions." *Physics Letters A* 28.1 (1968): 62-63.

[61] A. Rimberg. Dissipation-driven superconductor-insulator transition in a two-dimensional Josephsonjunction array. Phys. Rev. Lett., 48(13):3316–2635, March 1997.

[62] Abraham, David W., et al. "Resistive transition in two-dimensional arrays of superconducting weak links." *Physical Review B* 26.9 (1982): 5268..

[63] J.M. Kosterlitz and D.J. Thouless. Ordering, metastability and phase transitions in two-dimensional systems. J. Phys. C. Solid State, 1181(6):1181 – 1203, 1973.

[64] H.S.J. Van der Zant and H.A. Rijken. Phase transition of frustrated two-dimensional Josephson junction arrays. J. Low Temp. Phys., 82, 1991.

[65] M.P.A. Fisher. Quantum phase transitions in disordered two-dimensional superconductors. Phys. Rev. Lett., 65(7):923–927, August 1990.

[66] C. Ebner and D. Stroud. Diamagnetic susceptibility of superconducting clusters: Spin-glass behavior. Phys. Rev. B, 31(1):165, January 1985.

[67] C. Chen, P. Delsing, D. Haviland, Y. Harada, and T. Claeson. Flux flow and vortex tunneling in two-dimensional arrays of small Josephson junctions. Phys. Rev. B, 54(13):9449–9457, October 1996.

[68] I.-C. Baek, Y.-J. Yun, and M.-Y. Choi. Vortex state of a 2D Josephson junction array at irrational frustration. Physica C, 388-389:785–786, May 2003.

[69] H.S.J. Van der Zant, F.C. Fritschy, T.P. Orlando, and J.E. Mooij. Vortex dynamics in two-dimensional underdamped, classical Josephson-junction arrays. Phys. Rev. B, 47(1):295–304, January 1993.

[70] Kawaguchi, Takaaki. "Depinning mechanism and driven dynamics of vortices in disordered Josephson junction arrays." *Physica C: Superconductivity* 392 (2003): 364-368.

[71] D. Kimhi and F. Leyvraz. Resistive transition in two-dimensional arrays of proximity Josephson junctions: Magnetic field dependence. Phys. Rev. B, 1984.

[72] B.J. Wees, H.S.J. Van der Zant, and J.E. Mooij. Phase transitions of Josephson-tunnel-junction arrays at zero and full frustration. Phys. Rev. B, 35(13):7291–7295, May 1987

[73] W.Y. Shih and D. Stroud. Two-dimensional superconducting arrays in a magnetic field: Effects of lattice structures. Phys. Rev. B, 32(1):158 – 165, July 1985.

[74] Koren, Gad. "Proximity effects at the interface of a superconductor and a topological insulator in NbN-Bi2Se3 thin film bilayers." *Superconductor Science and Technology* 28.2 (2014): 025003.

[75] Bae, Seokjin, et al. "Microwave Meissner screening properties of proximity-coupled topological-insulator/superconductor bilayers." *Physical Review Materials* 3.12 (2019): 124803.

[76] Hu, Lun-Hui, Chao-Xing Liu, and Fu-Chun Zhang. "Topological Larkin-Ovchinnikov phase and Majorana zero mode chain in bilayer superconducting topological insulator films." *Communications Physics* 2.1 (2019): 1-7.

[77] Kayyalha, Morteza, et al. "Highly skewed current–phase relation in superconductor–topological insulator–superconductor Josephson junctions." *npj Quantum Materials* 5.1 (2020): 1-7.

[78] Kurter, Cihan, et al. "Evidence for an anomalous current–phase relation in topological insulator Josephson junctions." *Nature communications* 6.1 (2015): 1-6.

[79] Martinoli, Piero, and Chris Leemann. "Two dimensional Josephson junction arrays." *Journal of Low Temperature Physics* 118.5-6 (2000): 699-731.

[80] Kosterlitz, John Michael, and David James Thouless. *Journal of Physics C: Solid State Physics* 6.7 (1973): 1181.

[81] Kosterlitz, J. M. *Journal of Physics C: Solid State Physics* 7.6 (1974): 1046.

[82] D.J. Resnick and J.C. Garland. Kosterlitz-Thouless transition in proximity-coupled superconducting arrays. Phys. Rev. Lett., 47(21), November 1981.

[83] Lobb, C. J., David W. Abraham, and M. Tinkham. "Theoretical interpretation of resistive transition data from arrays of superconducting weak links." *Physical Review B* 27.1 (1983): 150.

[84] Henini, Mohamed, ed. *Molecular beam epitaxy: from research to mass production*. Newnes, 2012.

[85] Eley, Serena, et al. "Approaching zero-temperature metallic states in mesoscopic superconductor–normal–superconductor arrays." *Nature Physics* 8.1 (2012): 59-62.

[86] Flötotto, David, et al. "Superconducting pairing of topological surface states in bismuth selenide films on niobium." *Science advances* 4.4 (2018): eaar7214.

[87] Haviland, David B., Karin Andersson, and Peter Ågren. "Superconducting and insulating behavior in one-dimensional Josephson junction arrays." *Journal of Low Temperature Physics* 118.5-6 (2000): 733-749.

[88] Williams, J. R., A. J. Bestwick, P. Gallagher, Seung Sae Hong, Y. Cui, Andrew S. Bleich, J. G. Analytis, I. R. Fisher, and D. Goldhaber-Gordon. "Unconventional Josephson effect in hybrid superconductor-topological insulator devices." *Physical review letters* 109, no. 5 (2012): 056803.

[89] Charpentier, Sophie, Luca Galletti, Gunta Kunakova, Riccardo Arpaia, Yuxin Song, Reza Baghdadi, Shu Min Wang et al. "Induced unconventional superconductivity on the surface states of Bi 2 Te 3 topological insulator." *Nature communications* 8, no. 1 (2017): 1-8.

[90] Ambegaokar, Vinay, and B. I. Halperin. "Voltage due to thermal noise in the dc Josephson effect." *Physical Review Letters* 22, no. 25 (1969): 1364.

[91]Herbert, S. T., Y. Jun, R. S. Newrock, C. J. Lobb, K. Ravindran, H-K. Shin, D. B. Mast, and S. Elhamri. "Effect of finite size on the Kosterlitz-Thouless transition in two-dimensional arrays of proximity-coupled junctions." *Physical Review B* 57, no. 2 (1998): 1154.

[92] Rzchowski, M.S., Benz, S.P., Tinkham, M. and Lobb, C.J., 1990. Vortex pinning in Josephson-junction arrays. *Physical Review B*, *42*(4), p.2041.

[93] Van der Zant, H.S.J., Rijken, H.A. and Mooij, J.E., 1991. Phase transition of frustrated two-dimensional Josephson junction arrays. *Journal of low temperature physics*, *82*(1-2), pp.67-92.

[94] Rzchowski, M.S., Benz, S.P., Tinkham, M. and Lobb, C.J., 1990. Vortex pinning in Josephson-junction arrays. *Physical Review B*, *42*(4), p.2041.

[95]Sarma, S.D., Freedman, M. and Nayak, C., 2015. Majorana zero modes and topological quantum computation. *npj Quantum Information*, *1*(1), pp.1-13.

[96] Hlevyack, J.A., Najafzadeh, S., Lin, M.K., Hashimoto, T., Nagashima, T., Tsuzuki, A., Fukushima, A., Bareille, C., Bai, Y., Chen, P. and Liu, R.Y., 2020. Massive Suppression of Proximity Pairing in Topological (Bi 1− x Sb x) 2 Te 3 Films on Niobium. *Physical Review Letters*, *124*(23), p.236402.

[97] Bose, S.A.N.G.I.T.A., 2007. *Size effects in nanostructured superconductors* (Doctoral dissertation, Thesis).

[98] Courtois, H., Gandit, P., Mailly, D. and Pannetier, B., 1996. Long-range coherence in a mesoscopic metal near a superconducting interface. *Physical review letters*, *76*(1), p.130.

[99] Katz, A.S., Woods, S.I. and Dynes, R.C., 2000. Transport properties of high-T c planar Josephson junctions fabricated by nanolithography and ion implantation. *Journal of Applied Physics*, *87*(6), pp.2978-2983.

[100] Courtois, H., Gandit, P. and Pannetier, B., 1995. Proximity-induced superconductivity in a narrow metallic wire. *Physical Review B*, *52*(2), p.1162.

[101] Hlevyack, J.A., Najafzadeh, S., Lin, M.K., Hashimoto, T., Nagashima, T., Tsuzuki, A., Fukushima, A., Bareille, C., Bai, Y., Chen, P. and Liu, R.Y., 2020. Massive suppression of proximity pairing in topological $(Bi_{1-x}Sb_x)_2Te_3$ films on niobium. *arXiv preprint arXiv:2006.01716*.

[102] Cha, M.C., Fisher, M.P., Girvin, S.M., Wallin, M. and Young, A.P., 1991. Universal conductivity of two-dimensional films at the superconductor-insulator transition. *Physical Review B*, *44*(13), p.6883.

[103] Geerligs, L.J., Peters, M., De Groot, L.E.M., Verbruggen, A. and Mooij, J.E., 1989. Charging effects and quantum coherence in regular Josephson junction arrays. *Physical review letters*, *63*(3), p.326.

[104] Granato, E. and Kosterlitz, J.M., 1990. Superconductor-insulator transition and universal resistance in Josephson-junction arrays in a magnetic field. *Physical review letters*, *65*(10), p.1267.

[105] Van Otterlo, A., Wagenblast, K.H., Fazio, R. and Schön, G., 1993. Response of Josephson-junction arrays near the quantum phase transition. *Physical Review B*, *48*(5), p.3316.

[106] Van der Zant, H.S.J., Elion, W.J., Geerligs, L.J. and Mooij, J.E., 1996. Quantum phase transitions in two dimensions: Experiments in Josephson-junction arrays. *Physical Review B*, *54*(14), p.10081.

[107] Takahide, Y., Yagi, R., Kanda, A., Ootuka, Y. and Kobayashi, S.I., 2000. Superconductor-insulator transition in a two-dimensional array of resistively shunted small Josephson junctions. *Physical Review Letters*, *85*(9), p.1974.

[108] Van der Zant, H.S.J., Elion, W.J., Geerligs, L.J. and Mooij, J.E., 1996. Quantum phase transitions in two dimensions: Experiments in Josephson-junction arrays. *Physical Review B*, *54*(14), p.10081.

[109] Fisher, M.P., 1987. Dissipation and quantum fluctuations in granular superconductivity. *Physical Review B*, *36*(4), p.1917.

[110] Abeles, B., 1977. Effect of charging energy on superconductivity in granular metal films. *Physical Review B*, *15*(5), p.2828.

[111] Fazio, R. and Schön, G., 1991. Charge and vortex dynamics in arrays of tunnel junctions. *Physical Review B*, *43*(7), p.5307.

[112] Mooij, J.E., Van Wees, B.J., Geerligs, L.J., Peters, M., Fazio, R. and Schön, G., 1990. Unbinding of charge-anticharge pairs in two-dimensional arrays of small tunnel junctions. *Physical review letters*, *65*(5), p.645.

[113] Sugahara, M., 1985. Superconductive granular thin film and phase quantum tunnel device. *Japanese journal of applied physics*, *24*(6R), p.674.

[114] Fang, M., Wang, Z., Gu, H., Tong, M., Song, B., Xie, X., Zhou, T., Chen, X., Jiang, H., Jiang, T. and Liu, S., 2020. Layer-dependent dielectric permittivity of topological insulator Bi2Se3 thin films. *Applied Surface Science*, *509*, p.144822.

[115] Falco, C.M., Parker, W.H., Trullinger, S.E. and Hansma, P.K., 1974. Effect of thermal noise on current-voltage characteristics of Josephson junctions. *Physical Review B*, *10*(5), p.1865.

[116] Ambegaokar, V. and Baratoff, A., 1963. Tunneling between superconductors. *Physical Review Letters*, *10*(11), p.486. and errata 11(2), p.104